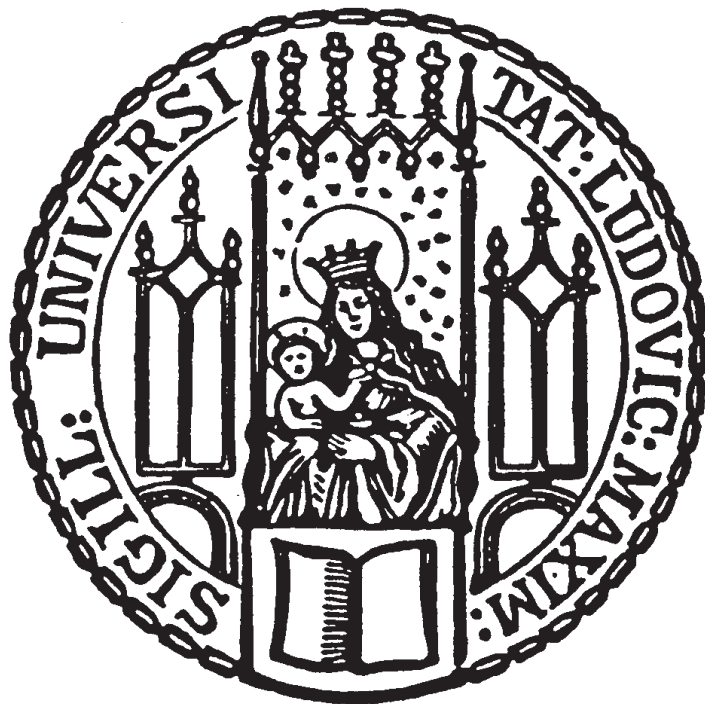


---

**Optimization of a scintillation detector with wave  
length shifting fiber and SiPM readout**

---

**Optimierung eines Szintillationsdetektors mit  
wellenlängenschiebender Faser und SiPM-Auslese**



**Masterarbeit der Fakultät für Physik  
der  
Ludwig-Maximilians-Universität München**

vorgelegt von

**Johannes Großmann**

geboren in Lichtenfels

**München, den 30.10.2014**

---

Gutachter: Prof. Dr. Otmar Biebel



---

## Abstract

---

The Cosmic Ray Facility (CRF) in Garching detects cosmic muons with a precision of  $50\ \mu\text{m}$ . It will be used for commissioning and calibration of micromegas detectors, which will be part of the ATLAS new small wheel upgrade. The current energy selector consists of an iron absorber, a trigger hodoskope and streamer tubes. The streamer tubes will be replaced by a newly developed scintillating detector. The goal of this work was the optimization of a scintillating detector with wavelength shifting fiber (WLSF) and Silicon Photomultiplier (SiPM) readout, which will be used as energy selector in the CRF. The current single detector prototype module consists of two trapezoidal, optically insulated BC-400 scintillator rods and covers  $9\ \text{cm} \times 60\ \text{cm}$  with a height of 4 cm. Each half has a minimum of two BCF-92 WLSF glued to grooves along the long side of the rod. Position sensitivity along the long side, the x-axis direction, is obtained via the time of flight information of the photons generated by the muons. Along the 9 cm side, the y-axis, the difference in the light output of the two halves is position sensitive due to the trapezoidal shape. The amount of light produced is proportional to the pathlength of the muon inside the rods and depends on the y-axis position, where the muon enters and exits the rods.

In this thesis an automatic SiPM characterization with a temperature controlled test setup has been developed. The electronic parameters of different SiPM types were deduced from U-I measurements and from charge spectra of illuminated SiPMs. The individual breakdown voltages 30 SiPM were deduced and from temperature studies the temperature coefficient for the bias voltage was determined. A multichannel gain stabilization system is presented, which reduces the gain variation of a SiPM due to temperature changes to 0.93%. The system is based on a digitally controlled voltage divider and monitors the temperature of each SiPM.

---

A Monte Carlo model for the SiPM detector response function is presented. The model shows, that the determination of the mean photon number using the number of nonsense-photon events is problematic and that the nonlinear response is mainly dominated by crosstalk effects.

The timing performance of the current readout system and the SiPM was studied with a detector prototype with a 20 MeV proton beam. It turns out, that the limiting factor for the position sensitivity of the time of flight information is the light trapping by the WLSF. Light emitted from points near the fiber generates narrow time spectra and a minimum spatial resolution along the x-axis of 10 cm is achieved. The spatial resolution degrades rapidly with the distance of the light source from the fiber. To obtain a better spatial resolution, the time information may be combined with pulse height information, but other concepts of determining the position along the x-axis should be considered in order to achieve a better position sensitivity.

---

## Kurzzusammenfassung

---

Das Ziel dieser Arbeit war die Optimierung eines szintillierenden Detektors mit wellenlängenschiebender Faser (WLSF) und SiPM Auslese, der als Energieselektor in der Cosmic Ray Facility (CRF) in Garching eingesetzt werden könnte. Die Cosmic Ray Facility detektiert Myonen mit einer Genauigkeit von  $50\ \mu\text{m}$  und nach Energieselektion benutzt man geradlinige Spuren für die Kalibration von Micromegas Detektoren, die Teil des ATLAS New Small Wheel Upgrades werden. Der Energieselektor besteht aus einem Eisenabsorber, einem Triggerhodoskop und Streamer Tubes. Die Streamer Tubes werden möglicherweise durch einen neu entwickelten szintillierenden Detektor ersetzt. Aktuell besteht ein einzelner Detektormodulprototyp aus zwei trapezoidalen, optisch isolierten BC-400 Szintillatorblöcken und deckt eine Fläche von  $9\ \text{cm} \times 60\ \text{cm}$  mit einer Höhe von  $4\ \text{cm}$  ab. Jede Hälfte hat mindestens zwei BCF-92 WLSF, die in eine Nut entlang der langen Seite der Blöcke geklebt sind. Positionsauflösung wird entlang der langen Seite des Szintillators, der x-Achse, durch die Flugzeitinformation der Photonen erreicht, die durch Myonen im Szintillator generiert werden. Die Sensitivität entlang der y-Achse beruht auf der Differenz der Lichtmenge in den Szintillatorhälften auf Grund der trapezoidalen Form. Die Lichtmenge ist proportional zur Weglänge der Myonen in den Blöcken und hängt von der y-Position ab, wo das Myon in die Blöcke eintritt und diese verlässt.

In dieser Arbeit wurde ein temperierter Teststand für die automatisierte Charakterisierung von SiPM entwickelt. Die elektrischen Parameter von verschiedenen SiPM Typen wurden aus U-I Messungen und aus Ladungsspektren von beleuchteten SiPMs hergeleitet. Der optimale Betriebspunkt wurde dadurch definiert. Aus Temperaturstudien wurde der Temperaturkoeffizient für die Betriebsspannung bestimmt. Ein Vielkanalsystem zur Stabilisierung der Verstärkung

---

wurde entwickelt, welches die Variation der Verstärkung durch Temperaturänderungen auf 0.93 % reduziert. Das System basiert auf einem programmierbaren Spannungsteiler und überwacht die Temperaturen jedes SiPMs. Ein Monte Carlo Modell für die SiPM Response-Funktion wurde entwickelt. Das Modell zeigt, dass die Bestimmung der mittleren Photonenzahl über die Anzahl an No-Photonen Ereignissen problematisch ist und dass die Nichtlinearität hauptsächlich durch Crosstalk Effekte dominiert wird. Die Zeitauflösung des aktuellen Auslesesystems und des SiPMs wurde mit einem Detektorprototypen mittels eines 5 mm breiten, 20 MeV Protonenstrahls getestet. Es stellt sich heraus, dass der limitierende Faktor für die Positionsensitivität über die Flugzeitinformaton das Lichtsammeln durch die WLSF ist. Photonen aus Quellen nahe bei der Faser haben schmale Zeitspektren und eine minimale Ortsauflösung von 10 cm entlang der x-Achse wird erreicht. Die Ortsauflösung wird mit steigendem Abstand der Lichtquelle zur Faser schnell kleiner. Um eine bessere Ortsauflösung zu erreichen, könnte man die Zeitinformaton mit Pulshöheninformaton kombinieren oder andere Konzepte für die Bestimmung der Position entlang der x-Achse sollten in Erwägung gezogen werden.

---

## Preface

---

*Democritus - Fragment 11:*

*"There are two ways of knowledge, one genuine, one imperfect. To the latter belong all the following: sight, hearing, smell, taste, touch. The real is separated from this. When the imperfect can do no more—neither see more minutely, nor hear, nor smell, nor taste, nor perceive by touch with greater clarity — and a finer investigation is needed, then the genuine way of knowledge comes in as having a tool for distinguishing more finely." [Diels and Kranz, 1922, p.60]*



---

## Vorwort

---

*Demokrit Fragment 11:*

*"Es gibt zwei Formen der Erkenntnis, die echte und die unechte. Zur unechten gehören folgende allesamt: Gesicht, Gehör, Geruch, Geschmack, Gefühl. Die andere Form aber ist die echte, die von jener jedoch völlig geschieden ist. [...] Wenn die unechte nicht mehr ins Kleinere sehen oder hören oder riechen kann, sondern die Untersuchung ins Feinere geführt werden muss, dann tritt an ihre Stelle die echte, die ein feineres Denkkorgan besitzt." [Diels and Kranz, 1922, p.60]*



---

# Contents

---

1	Introduction	1
2	The interaction of charged heavy particles with matter	3
3	Basics on SiPM	5
3.1	Silicon . . . . .	5
3.2	Doped silicon . . . . .	9
3.3	The p-n junction . . . . .	10
3.4	The Silicon Photomultiplier . . . . .	13
3.4.1	Working principle . . . . .	13
3.4.2	SiPM properties . . . . .	15
3.4.3	SiPM noise characteristics . . . . .	19
4	Scintillation process and plastic scintillators	21
5	Wave length shifter and light collection	23
6	The idea of the POSSUMUS-detector	25
7	SiPM characterization	27
7.1	Temperature control . . . . .	28
7.1.1	Prototype A . . . . .	28
7.1.2	Prototype B . . . . .	29
7.2	Static characteristic . . . . .	30
7.2.1	Forward scan . . . . .	30
7.2.2	Reverse scan . . . . .	31
7.3	Dynamic characteristics . . . . .	35

Contents

---

8	SiPM gain stabilization	43
9	Model for the SiPM response	47
10	Tests on the time resolution and readout system	53
10.1	Photomultiplier-Fiber prototype . . . . .	54
10.2	SiPM-Fiber prototype . . . . .	57
10.3	SiPM scintillator block prototype . . . . .	61
10.3.1	Readout of WLSF with SiPM <sub>0/1</sub> . . . . .	62
10.3.2	Direct readout of scintillator SiPM <sub>2/4</sub> . . . . .	65
11	Conclusion and outlook	69
A	Appendix	73
A.1	The Chi-Square Test for comparison of experimental and simulated data . . . . .	73
A.1.1	Unweighted histograms . . . . .	74
A.1.2	Weighted histograms . . . . .	74
A.1.3	Histograms with normalized weights . . . . .	76
A.2	The constant fraction triggering technique . . . . .	76
A.3	Uniformity of channels for the voltage divider . . . . .	77
	Bibliography	83
	Acronyms	91
	Symbols	93
	Glossary	95
	List of Figures	99
	List of Tables	103

# CHAPTER 1

---

## Introduction

---

Large area micromegas detectors for the new small wheel upgrade 2018 of the ATLAS experiment will be built by the ATLAS collaboration. The LMU Munich participates in the construction of micromegas detectors, which will be tested and calibrated in the CRF (see Biebel et al. [2003]), figure 1.1, in Garching. The CRF tracks high energetic muons with two reference drift chambers with accuracy of  $50\ \mu\text{m}$ . A veto on the low energetic muons is generated by the streamer tubes, which are used to measure the multiple scattering angle of the muons after passing a 34 cm thick iron absorber. In this way a threshold on the minimum energy of the muons of 600 MeV can be set [Biebel et al., 2003]. The streamer tubes have some disadvantages and it is planned to replace them by a scintillating detector with SiPM readout (POSSUMUS project, see [Ruschke, 2014]), which will be position sensitive in two directions. The goal is to achieve a position resolution of 5 mm in y-direction and of 5 cm in the x-direction. The POSSUMUS detector is a prototype detector, newly developed at the LMU Munich. The idea of the detector is, to combine two optically insulated trapezoidal scintillator rods. The light produced by the incoming particles is collected by scintillating fibers and guided to the double sided SiPM readout. The position resolution along the y-axis is achieved using the difference in the light output of the two scintillator rods, which is due to the trapezoidal shape. The position sensitivity along the x-axis is obtained using the time of flight information of the signal.

Several prototypes had been built and beamtimes at CERN had shown, that the resolution along the x-axis is in minimum 15 cm and along the y-axis 5 mm (see Ruschke [2014]).

One goal of this thesis, was to improve the SiPM characterization capabilities, which is important for the adequately biasing the detector at a good operating point and to understand the detector response. Furthermore the position sensitivity along the x-axis should be increased and the important effects, which dominate the position resolution along the x-axis, were studied.

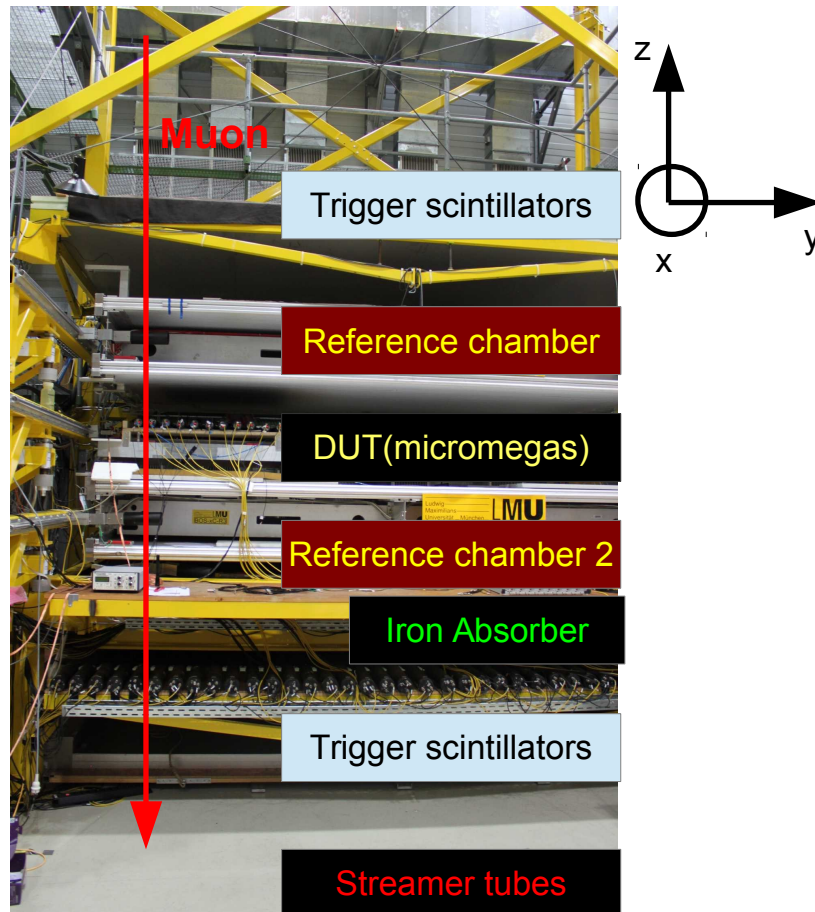


**Figure 1.1:** The CRF consists of two scintillator trigger hodoskopes, two reference chambers, the iron absorber and the streamer tubes.

## CHAPTER 2

---

### The interaction of charged heavy particles with matter

---

Heavy charged particles mainly interact with matter in two ways. They may be deflected by inelastic collisions with atomic electrons of a material or by elastic scattering from nuclei. Bremsstrahlung, nuclear reactions and the emission of Cherenkov radiation are less important and rare in comparison to the latter. The average energy loss per unit path length is called stopping power and is described by the Bethe-Bloch formula with shell correction  $\frac{C}{Z}$  and density correction  $\delta$

$$-\frac{dE}{dx} = 2\pi N_a r_e^2 m_e c^2 \rho \frac{Z}{A} \frac{z^2}{\beta^2} \left[ \ln \left( \frac{2m_e \gamma^2 v^2 W_{max}}{I^2} \right) - 2\beta^2 - \delta - 2\frac{C}{Z} \right], \quad (2.1)$$

where  $2\pi N_a r_e^2 m_e c^2 = 0.1535 \text{ MeV cm}^2 \text{ g}^{-1}$ .

The Bethe-Bloch formula has a minimum at  $\beta\gamma = 4$  and those particles are called minimum ionizing. The range of particles is obtained by integration of the Bethe-Bloch formula up to a minimum energy.

Symbol	Meaning
$r_e$	classical electron radius
$m_e$	electron mass
$N_a$	Avogadro number
$I$	mean excitation potential
$Z$	atomic number of absorbing material
$A$	atomic weight of absorbing material
$\rho$	density of absorbing material
$z$	charge of incident particle in units of $e$
$\beta$	$v/c$ of the incident particle
$\gamma$	$1/\sqrt{1-\beta^2}$
$\delta$	density correction
$C$	shell correction
$W_{max}$	maximum energy transfer in a single collision

**Table 2.1:** Symbols for the advanced Bethe-Bloch formula (2.1).

# CHAPTER 3

---

## Basics on SiPM

---

### 3.1 Silicon

The material silicon today is one of the most important materials when building modern electronics and one can use it to detect ionizing particles at high precision as well as for photon-counting at single-photon level.

Material	Silicon (Si)
Lattice	fcc-cubic
Density	$2.329 \text{ g cm}^{-3}$
Refractive index	3.42
Breakdown field	$\approx 3 \times 10^5 \text{ V cm}^{-1}$
Band gap	1.12 eV
Intrinsic carrier density	$9.65 \times 10^9 \text{ cm}^{-3}$ [Altermatt et al., 2003]
Mean energy for e-h-pair creation	3.63 eV
Absorption coefficient $\alpha$ (see fig. 3.2)	$1 \times 10^7 \text{ m}^{-1}$ to $1 \times 10^5 \text{ m}^{-1}$

**Table 3.1:** Properties of silicon at 300 K

Silicon is an indirect semiconductor and the electrical properties are related to its energy band structure. There are three different principal energy band structures for metals, insulators and semiconductors as one can see in figure 3.1. At absolute zero temperature the valence band is completely occupied and the maximum energy of the highest occupied state is called  $E_v$ . Electrons in the valence band are bound and cannot move through the crystal. In analogy there is the conduction band, which is completely empty at zero temperature. The energy of the lowest

unoccupied state is called  $E_c$ . Electrons can move inside the conduction band and build up an electrical current. The bandgap is the forbidden area in between. There are no allowed energy states available and the width of the bandgap is  $E_g = E_c - E_v$ . The difference in electronic behaviour of a material is mainly given by the bandgap energy  $E_g$ . For metals it is  $E_g < 0$ , for semiconductors  $E_g > 0$  and for insulators  $E_g \gg 0$ . For silicon, a semiconductor, the valence band is filled and the conduction band is only partly filled, depending on the ambient temperature.

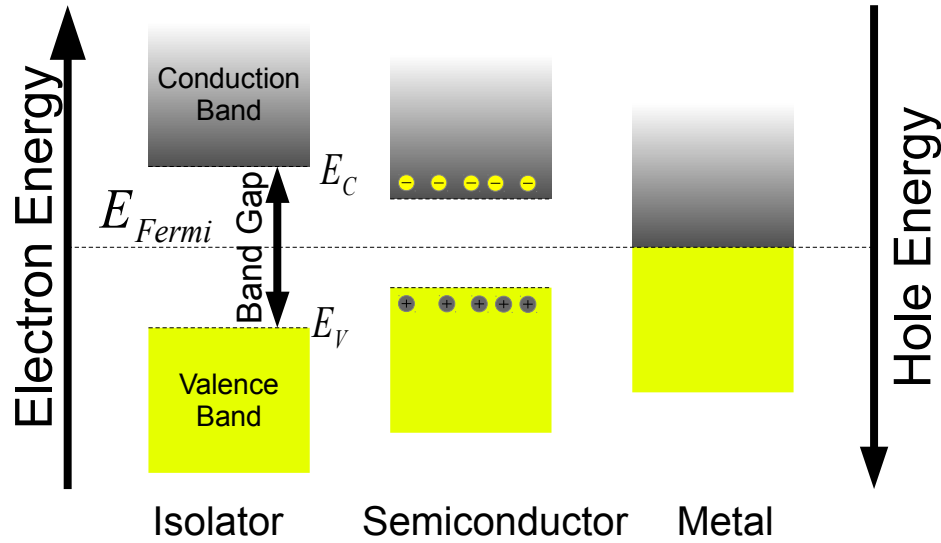


**Figure 3.1:** Three principal types of band structures - metal, semiconductor and insulator. One finds the Fermi energy  $E_{Fermi}$ , Bandgap energy  $E_g = E_c - E_v$ , where  $E_c$  is the conduction band edge energy and  $E_v$  is the valence band edge energy

The probability that an orbital at energy  $E$  will be occupied in thermal equilibrium is given by the Fermi-Dirac Probability Density Function (PDF) [Kittel and McEuen, 1976, p. 136]

$$f(E) = \frac{1}{\exp[(E - \mu)/k_B T] + 1} \quad (3.1)$$

with the chemical potential  $\mu$ , which equals  $E_F$  (see 3.1) for small temperatures, and the Boltzmann constant  $k_B = 8.617 \times 10^{-5} \text{ eV K}^{-1}$ . The equation (3.1) for electron energies far greater than the Fermi energy reduces to the Maxwell Boltzmann distribution:

$$f_e(E) \approx \exp\left(-\frac{E - \mu}{k_B T}\right), \quad \text{if } E - \mu \gg k_B T \quad (3.2)$$

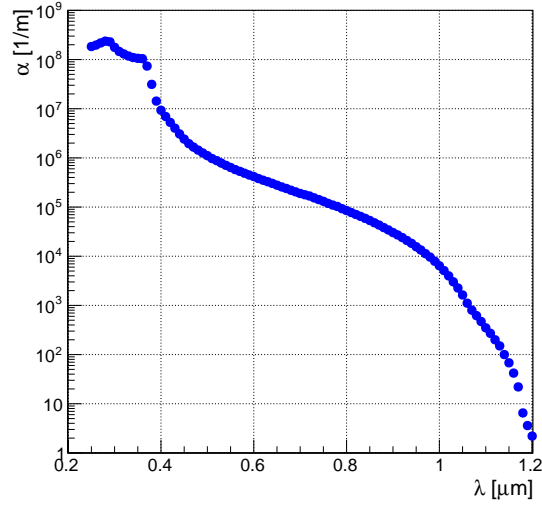


**Figure 3.2:** Absorption coefficient of silicon at 300 K taken from Green [2008]. The range of visible light in silicon is in the order of a few 0.1  $\mu\text{m}$  for blue light and 10  $\mu\text{m}$  for red light.

For non occupied states in the valence band (holes) the density of states one obtains in a similar approximation with  $f_e + f_h = 1$ :

$$f_h = 1 - f_e \approx \exp\left(-\frac{\mu - E}{k_B T}\right) \quad (3.3)$$

The use of  $E_F$  similar to the chemical potential  $\mu$  is convention in semiconductor physics. In the conduction band [Kittel and McEuen, 1976, see p. 205]

$$E_k = E_c + \hbar^2 k^2 / 2m_e \quad (3.4)$$

holds for the electron energy, with  $E_c$  the lowest energy inside the conduction band. The density of states in the conduction band for electrons is the number of orbitals per unit energy range and is given by [Kittel and McEuen, 1976, see p. 205]

$$D_e(E) = \frac{dN}{dE} = \frac{1}{2\pi^2} \cdot \left(\frac{2m_e}{\hbar^2}\right)^{3/2} \cdot (E - E_c)^{1/2} \quad (3.5)$$

where  $m_e$  is the effective electron mass. By convolution of  $D_e(E)$  and  $f_e(E)$  from (3.2) we obtain the concentration of electrons in the conduction band:

$$n = \int_{E_c}^{\infty} D_e(E) f_e(E) dE \quad (3.6)$$

This integral yields [Kittel and McEuen, 1976, see p. 206]:

$$n = 2 \left( \frac{m_e k_B T}{2\pi\hbar^2} \right)^{3/2} \exp[(\mu - E_c)/k_B T] = n_c \exp[(\mu - E_c)/k_B T] \quad (3.7)$$

In a similar manner one obtains a formula for the concentration of holes in the valence band [Kittel and McEuen, 1976, see p. 206]:

$$p = 2 \left( \frac{m_h k_B T}{2\pi\hbar^2} \right)^{3/2} \exp[(E_v - \mu)/k_B T] = n_v \exp[(E_v - \mu)/k_B T] \quad (3.8)$$

Multiplication of (3.7) and (3.8) yields

$$np = 4 \left( \frac{k_B T}{2\pi\hbar^2} \right)^3 (m_e m_h)^{3/2} \exp(-E_g/k_B T), \quad (3.9)$$

where  $\mu$  gets eliminated and the difference  $E_c - E_v = E_g$  is equal to the bandgap. The number of electrons equals the number of holes for an intrinsic semiconductor so that one obtains from equation (3.9) [Kittel and McEuen, 1976, see p. 207]

$$n_i = p_i = 2 \left( \frac{k_B T}{2\pi\hbar^2} \right)^{3/2} (m_e m_h)^{3/4} \exp(-E_g/2k_B T) \quad (3.10)$$

as intrinsic density of charge carriers in thermal equilibrium, where the electron-hole pair creation rate equals the recombination rate. For equal effective masses of electrons and holes  $m_h = m_e$  in the intrinsic case the Fermi level is in the middle of the bandgap [Kittel and McEuen, 1976, see p. 207].

$$\mu = \frac{1}{2} E_g + \frac{3}{4} k_B T \ln(m_h/m_e) \quad (3.11)$$

## 3.2 Doped silicon

If one deliberately adds impurities to a semiconductor (doping) the material characteristics change and the semiconductor shows extrinsic behaviour. In the following we consider the case for silicon, which forms four covalent bonds. There are two ways of doping. One adds

- donors, atoms of valence five like P or As, which leave free excess electrons in the conduction band.
- acceptors, of valence three, like B or Al, which leave positive holes in the valence band.

Donors (n-type silicon) and acceptors (p-type silicon) introduce states in the forbidden region (bandgap) and an increase in doping concentration affords an increase in conductivity (see figure 3.3). The Fermi level shifts towards the conduction band for n-type silicon and towards the valence band for p-type silicon. The extra electrons for n-type material reside in a discrete energy level inside the gap and can be excited into the conduction band. For p-type material the extra states are created in the forbidden region near the valence band, which means, that electrons from the valence band are excited to this extra level. In this case an electron-hole pair is created and the holes become majority charge carriers for this kind of material. In order to calculate the fermi level, assume that in n-type silicon the electron density is given mainly by the donor density  $N_{donor}$  and, that for p-type material  $p \approx N_{acceptor}$ . Using equation (3.7) and (3.8) the shifted Fermi level ( $E_{Fermi} = \mu$ ) reads:

$$E_{Fermi,n} = E_c - k_B T \ln(N_C / N_{donor}) \quad (3.12)$$

$$E_{Fermi,p} = E_v + k_B T \ln(N_C / N_{acceptor}) \quad (3.13)$$

In the same manner for the charge carrier concentration one obtains:

$$n_n = n_i \exp\left(\frac{E_{Fermi,n} - E_{Fermi,i}}{k_B T}\right) \quad (3.14)$$

$$n_p = n_i \exp\left(\frac{E_{Fermi,p} - E_{Fermi,i}}{k_B T}\right) \quad (3.15)$$

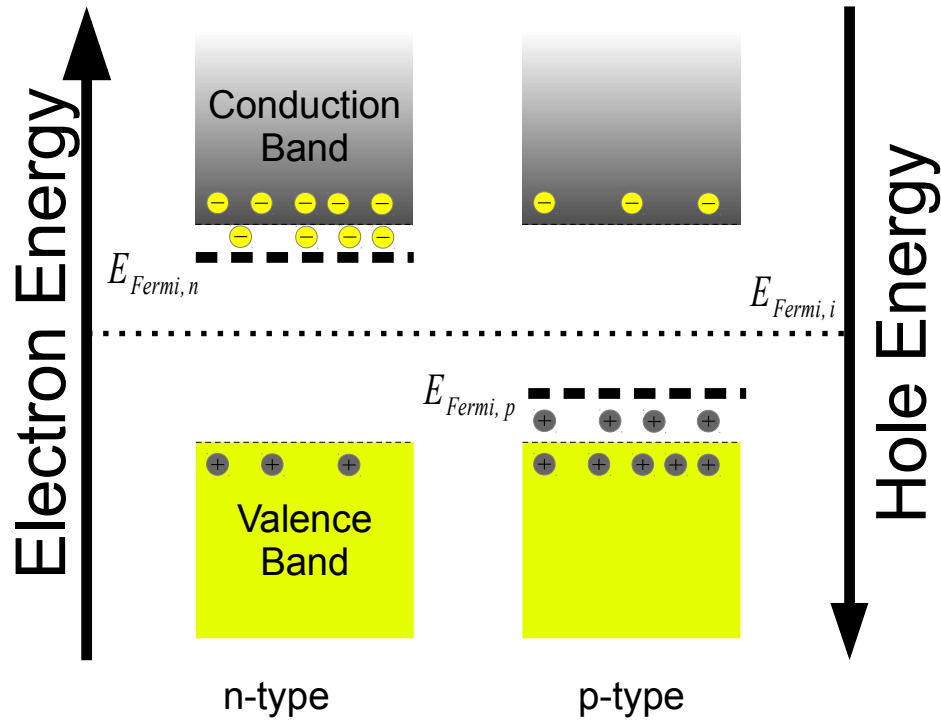


**Figure 3.3:** The band structure of p and n-type silicon. In n-type silicon electrons form the majority charge carrier while holes are minority charge carriers, whilst in p-type material this is vice versa.

### 3.3 The p-n junction

If one joins p-type material and n-type material, the Fermi levels equalize and the energy bands bend. The boundary of the two regions is called p-n junction (see fig.3.4). The extra electrons from the n-type region drift towards the p-region and fill the holes, while the diffusion is vice-versa for the p-region holes. A net charge builds up on either side of the junction and an electric field gradient is created. The net charge is positive for the n-region, negative for the p-region. The field gradient leads to a contact potential  $V_0$  [Leo, 1994, see pp. 223]. The region near the boundary is called depletion zone, which is free of mobile charge carriers.

One can calculate the width of such a depletion zone using the Poisson equation in one dimension,

$$\frac{d^2V}{dx^2} = -\frac{\rho(x)}{\epsilon}, \quad (3.16)$$

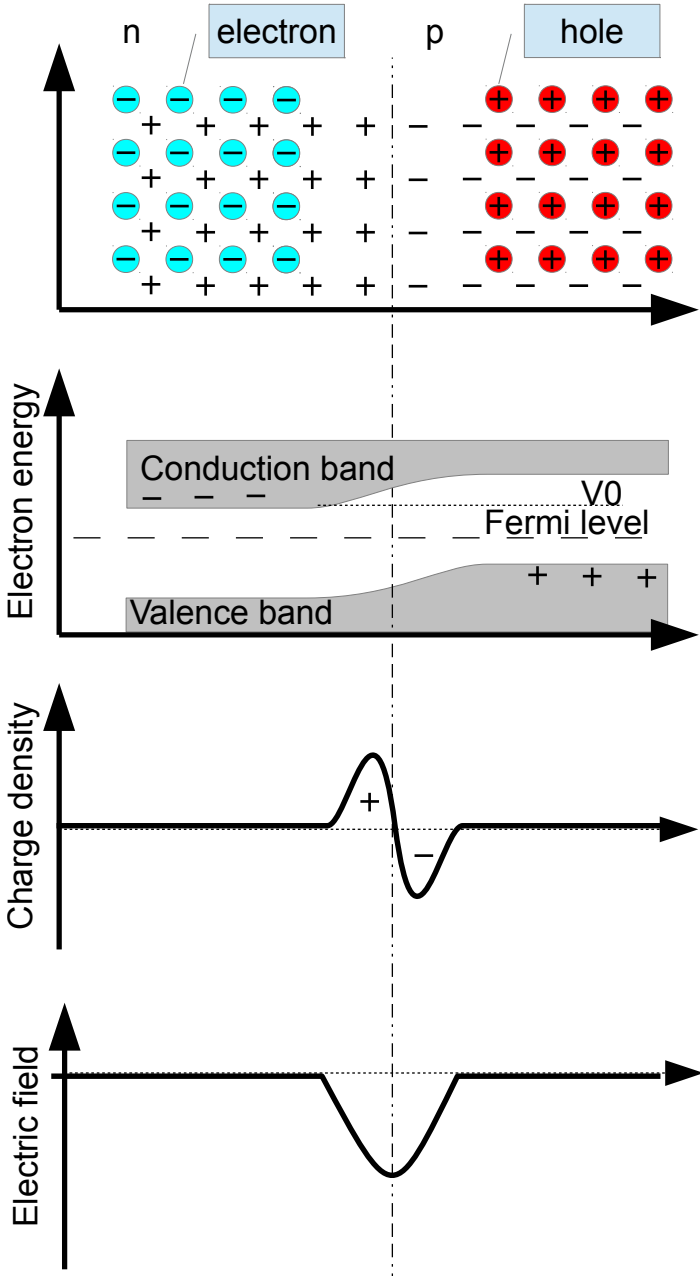


Figure 3.4: The p-n junction in a doped semiconductor

where  $\varepsilon = \varepsilon_0 \times \varepsilon_{silicon}$ .

In the following the author sticks to the derivation of the formulae in Leo [1994, see pp. 224-225]. For simplicity assume a uniform charge distribution along the x-axis for each side,

$$\rho(x) = \begin{cases} eN_D & 0 < x < x_n \\ -eN_A & -x_p < x < 0, \end{cases} \quad (3.17)$$

where  $e$  is the elementary charge and  $N_D$  and  $N_A$  are the donor and acceptor concentrations. For reasons of charge conservation it holds

$$N_A x_p = N_D x_n. \quad (3.18)$$

By integration of (3.16) and using  $dV/dx = 0$  at  $x = x_n, x = x_p$  one finds

$$\frac{dV}{dx} = E(x) = \begin{cases} -eN_D x + C_n & 0 < x < x_n \\ eN_A x + C_p & -x_p < x < 0. \end{cases} \quad (3.19)$$

Solving Poisson's equation piecewise with the correct boundary conditions one obtains

$$V_0 = \frac{e}{2\varepsilon} (N_D x_n^2 + N_A x_p^2) \quad (3.20)$$

for the contact potential and for the width of the depletion zone [Leo, 1994, see pp. 225]

$$d = x_n + x_p = \left( \frac{2\varepsilon V_0 (N_A + N_D)}{e N_A N_D} \right)^{1/2}, \quad (3.21)$$

where  $N_a, N_d$  is the acceptor and donor concentration,  $\varepsilon$  is the vacuum permittivity and  $V_0$  the contact potential. For the case that  $N_A/N_D \gg 1$  one can further simplify equation (3.21) to

$$d \approx \left( \frac{2\varepsilon V_0}{e N_D} \right)^{1/2}. \quad (3.22)$$

This holds also, if an external (reverse) voltage is applied, which enlarges the depletion zone, by replacing  $V_0$  with  $V = V_0 + V_{ext}$ . From (3.22) one obtains

$$E(x=0) = \sqrt{\frac{e N_D V}{\varepsilon}} = \frac{2V}{d}. \quad (3.23)$$

## 3.4 The Silicon Photomultiplier

The first developments for light detection at low intensities with semiconductors were done by McIntyre [1961] and Haitz [1964], who were studying the effects of avalanche breakdown and microplasma effects in reverse biased silicon diodes. This research led to the development of the Avalanche Photo Diode (APD), which consists of a reverse biased p-n junction. Incoming particles or photons create electron-hole pairs, which create further electron-hole pairs and this leads to avalanche generation. The APD has an internal gain in the order of 50 to 500. For these devices cooling is mandatory in order to get acceptable signal-to-noise-ratio (SNR) and single photon counting is not possible. The next step was the SiPM (see figure 3.5,3.6), which is a matrix of APDs biased slightly above  $V_{bd}$ , the breakdown voltage, in so called Geiger mode and connected in parallel realized first by Golovin and Saveliev [2004] and Buzhan et al. [2003]. A sketch for the charge concentration of a single microcell can be found in figure 3.7.

### 3.4.1 Working principle

The initial process for the detection of a photon is the creation of an e-h-pair in the avalanche or drift region of the Geiger mode APD (GM-APD), due to absorption of a photon. The absorption coefficient of silicon determines the depth of interaction (see figure 3.2). When a single GM-APD is biased slightly above  $V_{bd}$  then the energy, that the charge carrier gains through the high electric field between two subsequent collisions, is high enough to generate further electron hole pairs via impact ionization (see figure 3.10). Note that the electron component dominates and ionization by holes is negligible. The microcell APD breaks down discharging the accumulated charge completely (see figures 3.8,3.9). The discharge is quenched by a voltage drop across a quenching resistor  $R_{quench}$  in series with the GM-APD. The equivalent circuit of a cell is given by a capacitance  $C_{cell}$  and a switch in parallel and a quenching resistance  $R_{quench}$  in series. The recharge time constant is  $\tau = R_{quench} \times C_{Cell}$ .

The gain ranges from  $1 \times 10^5$  to  $1 \times 10^6$  and depends on the charge stored on  $C_{Cell}$ . An estimation for the field strength in the avalanche region can be obtained

using equation (3.23), which yields  $10^5 \text{ V cm}^{-1}$  for typical width of the depletion zone of  $1 \mu\text{m}$  and bias voltage in the order of  $10^2 \text{ V}$ .

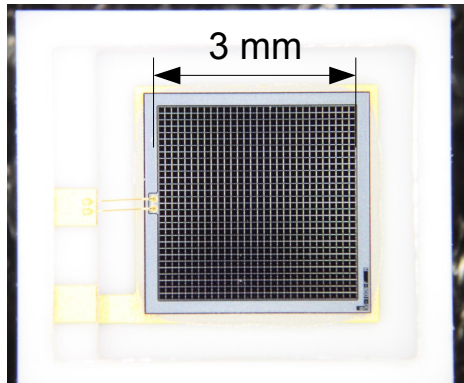


**Figure 3.5:** A Hamamatsu S10362-33-100C SiPM of size  $3 \text{ mm} \times 3 \text{ mm}$  with  $100 \mu\text{m}$  pixel pitch

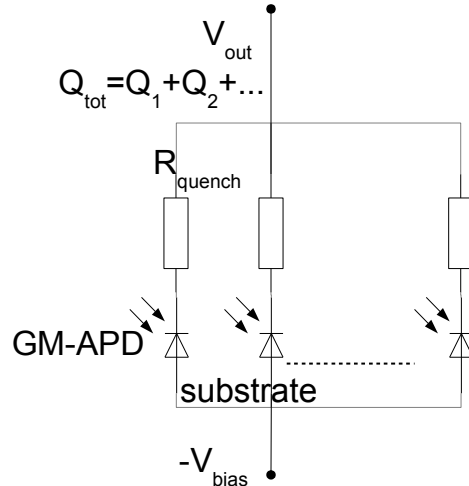


**Figure 3.6:** The equivalent circuit diagram of a SiPM. A microcell is represented by GM-APD with a capacitance  $C_{cell}$  and a resistance  $R_{quench}$

The advantages of silicon photomultipliers are the high internal gain, small volume, the use of standard silicon technology for production, the insensitivity to magnetic fields, good timing properties down to  $123 \text{ ps}$  [Buzhan et al., 2003, p. 51], photon detection efficiency of about  $30\%$  and SiPM tolerate accidental illumination. The major drawbacks today are the high dark count rate at single photon level, temperature dependence of signal form and gain, complex noise phenomena like optical crosstalk and afterpulses. One chooses the peak sensitivity wavelength of a SiPM by charge concentration profile. For high sensitivity for blue light, one p-silicon on n-substrate is necessary, for high sensitivity for green light the n-silicon on p-substrate configuration is preferred. Doping adjusts the position of the avalanche region and the position of the drift region of lower electric field, according to the absorption length of the material (see figure 3.2).

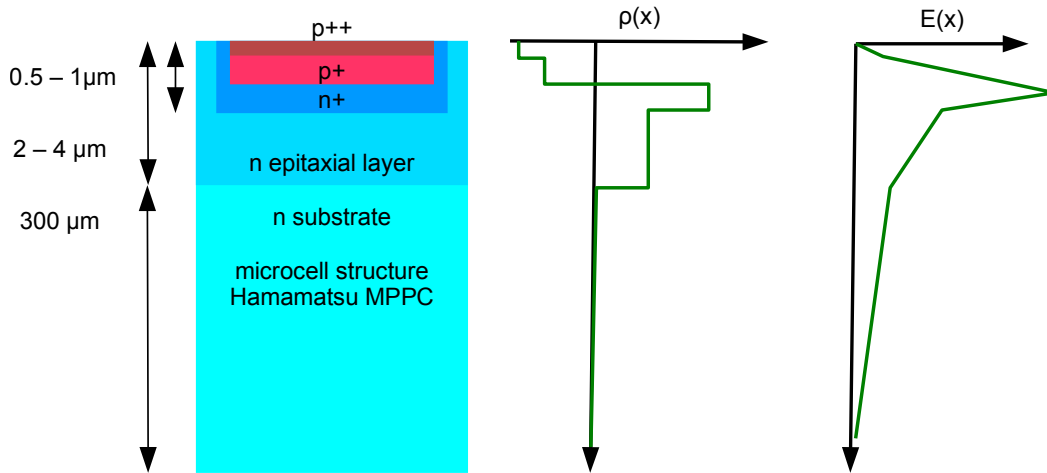


**Figure 3.7:** SiPM charge concentrations and field configuration of a single microcell (GM-APD) for a Hamamatsu SiPM. p+ and p++ refer to heavy and extreme heavy doping with more than 1 foreign atom per 1000 silicon atoms. [Renker and Lorenz, 2009, see p. 29]

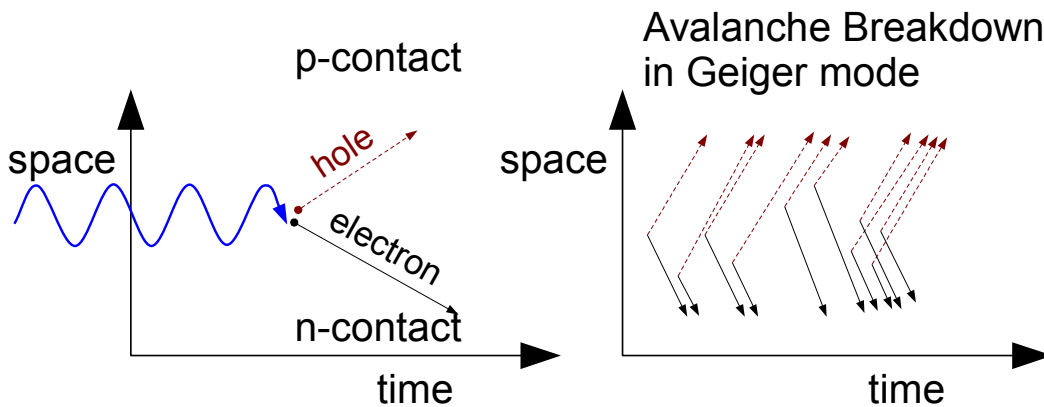


**Figure 3.8:** When biased above  $V_{bd}$  electron-hole pairs will trigger an avalanche due to impact ionization in the high field region of the GM-APD.

### 3.4.2 SiPM properties

The SiPM is biased above breakdown voltage. The difference  $V_{bias} - V_{bd} = V_{over}$  is called overvoltage ( $V_{over}$ ). A single microcell represents a capacitor (see figure 3.11) and the stored charge divided by  $e$  is the single pixel gain

$$G = Q/e = \frac{(V_{bias} - V_{bd})C_{Cell}}{e} . \tag{3.24}$$

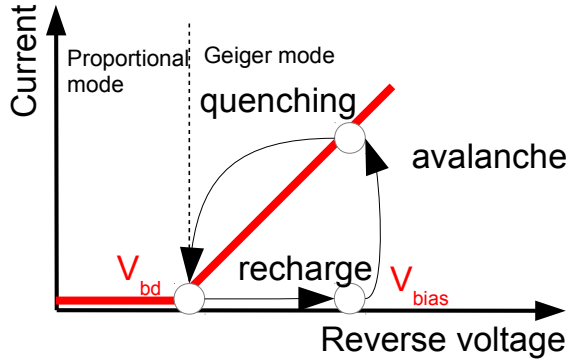


**Figure 3.9:** Operating mode of a GM-APD according to [Dinu, 2013]. Absorption leads to avalanche discharge, which is quenched by the voltage drop across  $R_{quench}$ . Then the cell is recharged and can be triggered again. The read line represents the linear dependence of the signal height on the overvoltage.

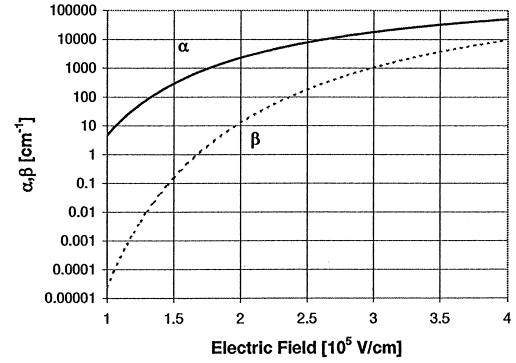


**Figure 3.10:** The impact ionization coefficients  $\alpha$  for electrons and  $\beta$  for holes from Musienko et al. [2000]. Avalanche breakdown is dominated by the electron component.

$G$  is a function of  $V_{over}$  and the temperature. For the differential it holds

$$dG = \frac{\partial G}{\partial T} dT + \frac{\partial G}{\partial V_{over}} dV_{over} \quad (3.25)$$

and for  $dG = 0$  one obtains

$$\frac{dV_{over}}{dT} = -\frac{\partial G}{\partial T} \left( \frac{\partial G}{\partial V_{over}} \right)^{-1}, \quad (3.26)$$

which means, that by correct adjustment of  $V_{bias}$  one can compensate temperature effects on  $G$ .

One refers to a 1 photo electron (PE) signal for a single cell, which is ideally uniform. All cells are connected in parallel (see figure 3.6) and in this way the readout signal is the sum signal

$$S = \sum_{i=1}^{n_c} S_i, \quad (3.27)$$

where  $n_c$  is the number of microcells on the SiPM.

The Photon Detection Efficiency (PDE) is the probability than an incoming photon with certain wavelength is detected. This number was measured to be about 35 % in maximum [Dinu et al., 2009, see p. 424] for the SiPM types used.  $PDE$  is the product of the ratio of active surface to total detector area, which is the geometrical efficiency  $\varepsilon_{geom}$ , the trigger efficiency to trigger a microcell  $\varepsilon_{trigger}$ , when an electron hole pair has been created, and the quantum efficiency  $QE$  to create a primary electron hole pair.

$$PDE = QE(\lambda) \times \varepsilon_{geom} \times \varepsilon_{trigger}(\lambda, V_{bias}, T) \quad (3.28)$$

Gain and PDE are related because  $\varepsilon_{trigger}$  is voltage dependent, which puts a lower limit on the feasible  $V_{over}$ . Furthermore the probability for optical crosstalk between microcells rises for higher  $V_{over}$ . This fakes larger signals and puts an upper limit to  $V_{over}$ .  $\varepsilon_{trigger}$  is a function of the impact ionization constants for electrons and holes (see figure 3.10). Note that the electron component is dominant, because of the lower effective electron mass, which results in greater electron mobility and therefore electrons gain more energy between subsequent collisions, so that it is more likely for them to have the required energy for creation of further electron-hole pairs and not to loose energy in other collision processes.

The time dependent electric signal of a SiPM consists of a fast and a slow component. The fast component is dominated by the avalanche discharge, while cell recovery is responsible for the slow one. The cell recovery time  $\tau_r$  is determined by the quenching resistance  $R_{quench}$  and the cell capacitance  $C_{Cell}$ :

$$\tau_r \approx R_{quench} C_{cell} \quad (3.29)$$

The sum signal (3.27) has to be corrected for saturation effects. A common correction for the number of triggers  $n_{trigger}$  ignoring the finite recovery time of a microcell [Pulko, 2012, see p. 12] , as well as crosstalk and afterpulsing, is given by

$$n_{trigger} = n_c \left[ 1 - \exp \left( - \frac{PDE \times n_{ph}}{n_c} \right) \right], \quad (3.30)$$

where  $n_{ph}$  is the number of incident photons.

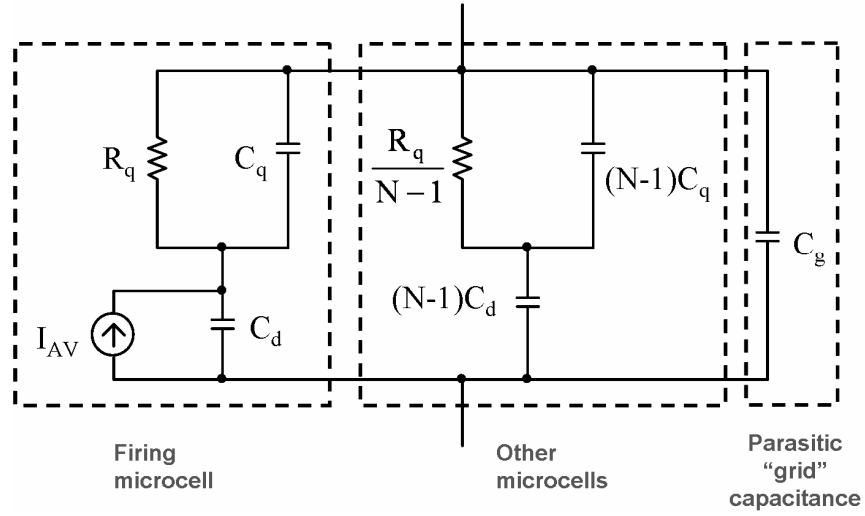


**Figure 3.11:** The equivalent circuit for a SiPM at low photon flux taken from Corsi et al. [2006, pg. 1277].  $C_d$  refers to  $C_{Cell}$  and  $R_q$  to  $R_{quench}$ .

Assuming a Gaussian distribution of the microcell capacities one obtains a general expression of the charge distribution of short light pulses [Finocchiaro et al., 2009, see p. 5]

$$f(x) = A \times \sum_{i=0}^{\infty} g(i) \frac{1}{\sqrt{2\pi}\sigma_{tot}(i)} \exp \left[ -\frac{(x - c(i))^2}{2\sigma_{tot}^2(i)} \right], \quad (3.31)$$

where

$$\sigma_{tot}^2 = \sigma_e^2 + i\sigma_1^2 \quad (3.32)$$

$$c(i) = c_0 + ic_1, \quad (3.33)$$

$A$  is an amplitude,  $g(i)$  is the distribution of the number of firing microcells, which is multiplied by a Gaussian distribution for  $i$ -firing cells.  $\sigma_{tot}(i)$  accounts for the broadening of the peaks and  $c(i)$  includes the uniform distance of the Gaussian peaks, which is due to equal charge released by the microcell (see (3.27)).  $\sigma_e$  is the electronic noise and  $\sigma_1$  is given by the Excess Noise Factor for a microcell breakdown, which is a quantity for pixel-to-pixel gain variation. Finocchiaro et al. [2009] propose a Poisson distribution for  $g(i)$ , in case the SiPM is triggered by

short light pulses. An elaborate model for  $g(x)$  has been developed by Ramilli et al. [2010].

### 3.4.3 SiPM noise characteristics

The principal issue of understanding the SiPM is to interpret correctly the complex noise phenomena.

#### 3.4.3.1 Dark counts

A microcell breakdown can be triggered by any process that generates an e-h pair in the sensitive region of a SiPM. Either it is an incoming photon, thermally or field-assisted generated e-h pairs [Renker and Lorenz, 2009, see p. 31]. The rate of thermally generated charge carriers is temperature dependent and is in the order of  $0.1 \text{ MHz mm}^{-2}$  to  $1 \text{ MHz mm}^{-2}$ . The dark count rate falls by order of magnitude, when increasing the threshold of the readout electronics. The so called staircase function (see figure 3.12) shows the Dark Count Rate (DCR) versus the discriminator threshold. Each step in the staircase corresponds to a certain number of simultaneously firing pixels. The amplitude of a single pixel signal is called 1 PE level. Recent investigations by Zappa et al. [see 2007, pg. 106] show, that the field assisted generation of dark counts via the Poole-Frenkel effect or trap-assisted tunneling are negligible, because the electric field stays below the critical limit.

In general the temperature dependence of DCR is given by the net charge carrier generation rate  $U = -n_i/\tau_e$ , where  $\tau_e$  is the lifetime of an e-h-pair. One finds that  $1/\tau_e$  is temperature independent near its maximum value, while for  $n_i$  equation (3.10) holds and one obtains

$$DCR = \frac{U \times F \times d}{\tau_e} \propto T^{3/2} \times \exp\left(\frac{-E_g}{2k_B T}\right), \quad (3.34)$$

where  $F$  is the area of the p-n junction and  $d$  the width of the depletion zone.

#### 3.4.3.2 Optical crosstalk

When a avalanche is triggered, on average 3 photons per  $1 \times 10^5$  carriers are generated [Lacaita et al., 1993]. The emitted photons have energies greater than

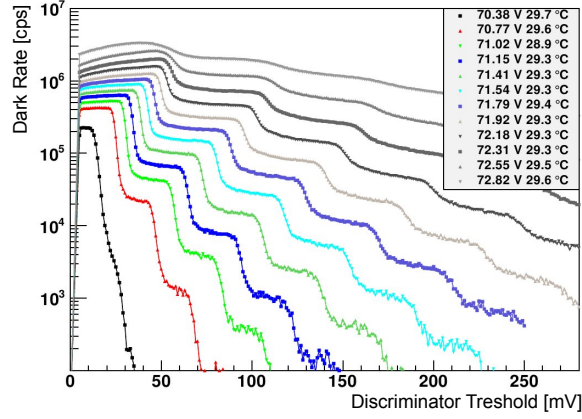


**Figure 3.12:** The dark count rate as a function of the discriminator threshold for a Hamamatsu S10362-11-050C (Ham. 1x1 050C) at different bias voltages from Grossmann [2012]. Each step represents a number of simultaneous firing pixels.

the bandgap of silicon and can therefore trigger other cells, which is called Optical Crosstalk (OC). This process corresponds to the shower fluctuation of an APD [Renker and Lorenz, 2009, see p. 32] and gives a corresponding Excess Noise Factor (ENF) for SiPM. The crosstalk probability is defined as

$$p_{cross} = \frac{DCR_{1.5pe}}{DCR_{0.5pe}}, \quad (3.35)$$

where  $DCR_{0.5pe}$  is the DCR at 0.5 PE level and  $DCR_{1.5pe}$  at 1.5 PE level. Modern devices use optical trenching to suppress OC. A compromise between acceptable level of OC and gain defines the feasible bias voltage.

#### 3.4.3.3 Afterpulsing

When charge carriers are trapped in crystal impurities during an avalanche, once released they can trigger a subsequent avalanche in the microcell up to 100 ns later. In this case an afterpulse (AP) is generated. The lifetime of charge carriers in deep-lying traps is parameterized by two time constants, a short one in the order of 50 ns and a long one in the order of 150 ns.

## CHAPTER 4

---

### Scintillation process and plastic scintillators

---

The plastic scintillator BC-400 used for POSSUMUS prototypes is a transparent material. The working principle for the scintillation process is as follows. Incoming particles produce a certain amount of photons, which is a function of the energy deposited in the scintillator. For this modern scintillator a nearly linear dependence of the light output on the energy deposited is found, if quenching effects for heavy particles do not play a role. The amount of light is detected typically by a conventional Photomultiplier or a SiPM, which produces in first order an electrical signal proportional to the number of impinging photons. The advantages of plastic scintillators are the possibility to obtain almost any desired form, the fast time response and low dead times in the order of a few ns, due to fast recovery times. This is why they are especially suited for triggering purposes.

In general the phenomenon for a material to produce light is called luminescence, which means, that the material absorbs and reemits energy in form of visible light. If the time scale of the reemission is less than  $1 \times 10^{-8}$  s, this is called fluorescence, which is exploited for scintillators [Leo, 1994, p. 158].

Luminescence for organic scintillators is usually based on  $\pi$ -molecular orbitals in benzene ring structures. The process may start with the absorption of a photon and subsequent excitation of an electron in the  $S_3$  singlet state. Non-radiative internal degradation leaves the electron in the  $S_1$  state, from where the electron has a high probability of radiative decay to excited vibrational states of  $S_0$ , which is called fluorescence (see figure 4.1). These emitted photons cannot be reabsorbed and this is why the scintillator is transparent to its own radiation (see [Leo, 1994, pp. 159-162]). For the triplet states  $T$  multipole selection rules forbid the transition to

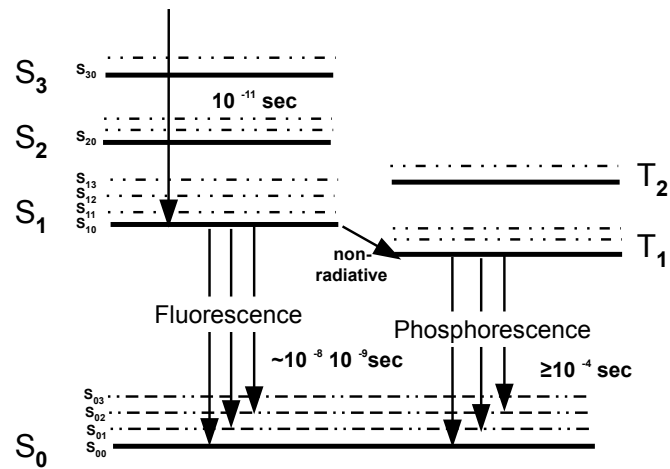
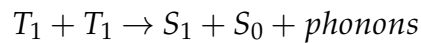


**Figure 4.1:** The scintillation principle with singlet and triplet states taken from White [1988].

the  $S_0$  state and the decay is realized by interaction with another excited molecule (see White [1988], Leo [1994, pg. 162]).



In this process one of the molecule ends in the  $S_0$  state and the decay is as mentioned before, which results in the delayed component of scintillation light.

# CHAPTER 5

---

## Wave length shifter and light collection

---

The produced light in the scintillator may be collected by a wave length shifting fiber. The WLSF consists of scintillator material, which is enriched with wavelength shifting components with the principal purpose of trapping the light inside the thin fiber, which is then guided by total reflection along the fiber. The second purpose is to match the wavelength of the emitted light to the wavelength of maximum sensitivity of the photon counter.

The underlying principle of wave length shifting is the Franck-Condon effect, which means, that the atoms in excited state are spatially shifted, such, that the de-excitation with the same energy is forbidden, because there is no wave-function overlap between excited state and ground state. Typically a fluor atom is excited to a vibrational mode of a higher electron level. Via internal degradation the vibrational mode decays to its ground state of the excited electron level. Due to the spatial displacement of the excited atom the probability for the transition to a vibrational mode of the electronic ground state is highest. This transition results in a photon with reduced energy.

Often two or more wave length shifting components are added to a scintillator. A sketch for such a de-excitation process one finds in figure 5.1.

The fiber typically consists of a core material and a cladding material. The refractive index of the cladding is lower than that of the core. The wave length shifted photons are emitted isotropic in all directions. Those emitted with angles lower than the angle for total reflection will exit the fiber at the ends, while the others are lost. The used WLSF (BCF-92) have a refractive index of  $n_{cladding} = 1.49$

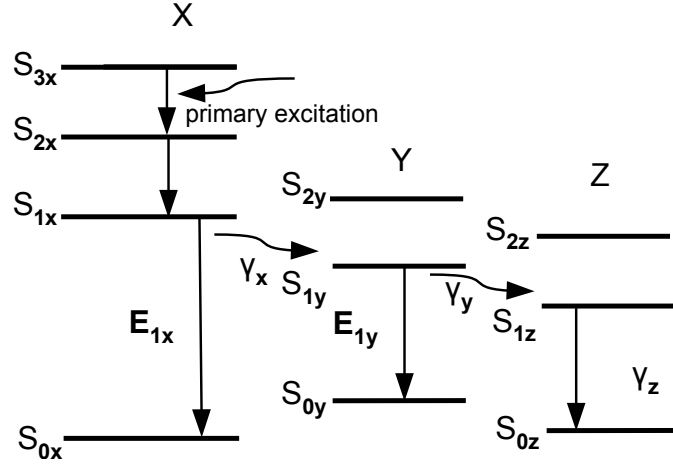


**Figure 5.1:** The de-excitation based on the Franck-Condon principle with two wavelength shifters involved from White [1988, pg. 821].

and  $n_{core} = 1.60$ , from which one calculates the angle of total reflection  $\theta_c$  via Snell's law:

$$\theta_c = \arcsin\left(\frac{n_{cladding}}{n_{core}}\right) = 68.63^\circ \quad (5.1)$$

The trapping efficiency one calculates from the probability of a photon to be emitted in the solid angle, where total reflection occurs.

$$P_{trap} = \frac{1}{4\pi} \left( 2 \int_0^{2\pi} d\phi \int_0^{\frac{\pi}{2} - \theta_c} d\theta \sin\theta \right) = 0.068 \quad (5.2)$$

The factor 2 accounts for the two possible directions, where the photon is emitted. Note that the absorption and subsequent emission process is essential for trapping photons in the fiber. Incoming photons leave the fiber, if no absorption takes place, because they never fulfill the conditions for total reflection.

## CHAPTER 6

---

### The idea of the POSSUMUS-detector

---

POSSUMUS means POsition Sensitive Scintillating MUon SiPM detector. The basic principle of one detector module is to combine two trapezoidal, long scintillators (see 6.1, thesis Ruschke [2014]). Consider a muon hits the detector from above and the amount of light produced is nearly proportional to the path length in the scintillator. Then the photon flux through the end of the fibers is proportional to the path length.

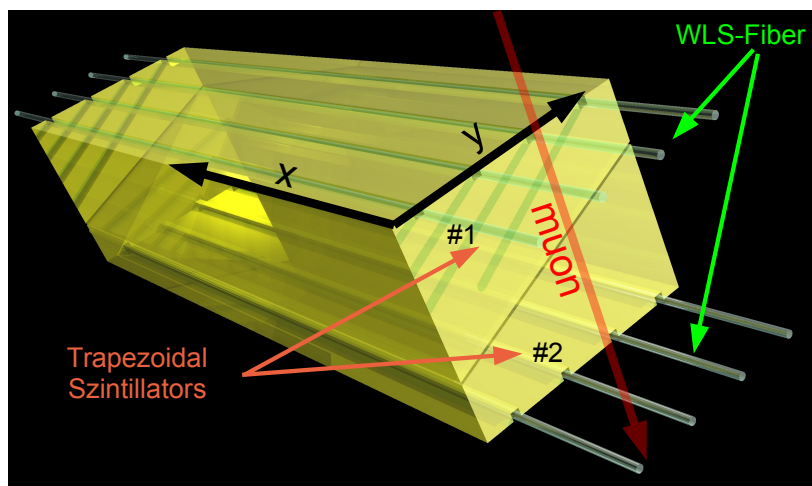


**Figure 6.1:** A sketch of a POSSUMUS detector module with four WLSF. The x-direction is defined along the long side of the scintillators.

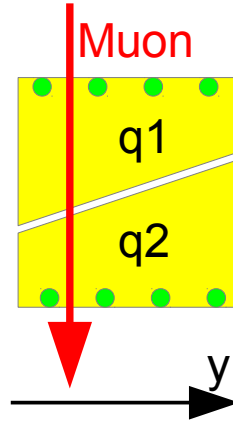


**Figure 6.2:** The basic principle to obtain a position sensitivity along the y-axis. The amount of light  $q1$  in the upper trapezoid is greater than  $q2$  in the lower trapezoid.

The position  $y$  can be expressed as a function of the amount of light produced in scintillator 1 and 2,  $q1$  and  $q2$ . Consider  $Z_{total}$  the total amount of light produced in both halves, then it holds  $Z_{total} = q1 + q2$  and

$$y \propto f\left(\frac{q1}{q1 + q2}\right) \approx \frac{q1}{q1 + q2} + C,$$

where  $C$  is an arbitrary constant. Note, that this formula is a rough approximation only, which ignores the Landau like energy loss of the muons. A more detailed calculation which includes the complete detector geometry one finds in Müller [2013] and Ruschke [2014].

The time of flight photons need until they exit the WLSF can be used to obtain the  $x$ -position of the incoming particle. Consider  $t_l$  and  $t_r$  the arrival time of the photons at the end of the fiber. The time difference is position sensitive and it holds,

$$x \propto c_{eff}(t_l - t_r),$$

where  $c_{eff}$  is an effective velocity of light yet including reflections by the scintillator walls and by the fiber cladding. The upper limit for  $c_{eff}$  is  $c_0/n_{scintillator}$ .

# CHAPTER 7

## SiPM characterization

In the first part of this work, methods for the characterization of SiPMs will be presented. For this purpose a temperature controlled electrically and optically insulated test setup was developed. Temperature controlling is needed, because the SiPM quantities like Gain  $G$ , quenching resistance  $R_{quench}$  and dark count rate DCR are temperature dependent. Furthermore the vendor of the devices gives recommendation on  $V_{bias}$ , but there is no information on the breakdownvoltage  $V_{bd}$ , which is essential in order to bias the SiPM at constant moderate  $V_{over}$  to reach a constant  $G$ . The device types in tables 7.1 and 7.2 have been tested.

Type (Parameters at 25 °C)	S10362-11-			Unit
Subtype	025C	050C	100C	
Area	1	1	1	mm <sup>2</sup>
$n_c$	1600	400	100	
Pixel size	25x25	50x50	100x100	μm <sup>2</sup>
Peak-PDE wavelength	440	440	440	nm
$\epsilon_{geom}$	30.8	61.5	78.5	%
Typical DCR	100	150	200	kHz
$dV_{bd}/dT$	56	56	56	mV °C <sup>-1</sup>
$G$	$2.75 \times 10^5$	$7.50 \times 10^5$	$2.40 \times 10^6$	

**Table 7.1:** Properties of different tested 1 mm × 1 mm SiPM types from Hamamatsu datasheet. In the following the author refers to Hamamatsu S10362-11-025C (Ham. 1x1 025C), Ham. 1x1 050C and Hamamatsu S10362-11-100C (Ham. 1x1 100C)

Type (Parameters at 25 °C)	S10362-33-		Unit
Subtype	050C	100C	
Area	9	9	mm <sup>2</sup>
$n_c$	3600	900	
Pixel size	50x50	100x100	μm <sup>2</sup>
Peak-PDE wavelength	440	440	nm
$\epsilon_{geom}$	61.5	78.5	%
Typical DCR	6	8	MHz
$dV_{bd}/dT$	56	56	mV °C <sup>-1</sup>
$G$	$7.50 \times 10^5$	$2.40 \times 10^6$	

**Table 7.2:** Properties of different tested 3 mm × 3 mm SiPM types from Hamamatsu datasheet. In the following the author refers to Hamamatsu S10362-3x3-025C (Ham. 3x3 025C), Hamamatsu S10362-3x3-050C (Ham. 3x3 050C) and Hamamatsu S10362-3x3-100C (Ham. 3x3 100C)

## 7.1 Temperature control

### 7.1.1 Prototype A

A first prototype of the temperature control system used a commercially available Peltier controller (Quick Ohm QC-PC-Co1C). The set temperature was adjusted using a digitally controlled 10 kΩ 8bit potentiometer. The system uses Pulse-width modulation (PWM) to control the power of a Peltier element. The input sensor of the system is a thermistor. For monitoring purpose the temperature values are recorded by two DS18B20 temperature sensor (DS18B20) every 30 s. The monitor system assures, that a set temperature was reached at the beginning of a measurement and that the temperature was kept constant within 0.1 K inside the box. A PSP1210 Voltcraft programmable power supply (psp1210) [Voltcraft, 2008] was used as voltage source for the Peltier element. Via the I<sup>2</sup>C Bus and an Arduino UNO microcontroller one could set the digital potentiometer. One problem of this setup was, that PWM is a source of noise for the measurement. This was the reason to build a second prototype B, using a software PID controller (see glossary PID controller).

## 7.1.2 Prototype B

The second prototype of the test setup was constructed by carefully insulating the Peltier element against the housing. The programmable PSP12010 was used as current source and the controlling parameters for the software PID controller could be adjusted manually. The temperature was constant within 0.1 K. An open source PID controller code was adapted. The achieved temperature range is from 5 °C to 60 °C. For reasons of stability and simplicity the controller was realized as PI-controller. The controller output was the set current for the Peltier element. The controller gain was set to  $K_P = 6 \text{ A K}^{-1}$  and with  $T_i = 62.8 \text{ s}$ . The direction of the current through the Peltier element is controlled via H Bridge (see figure A.8 for the wiring diagram) directly in software, so that the system can be used for cooling and heating. A characterization measurement (see figure 7.1) was done and a temperature difference of 26 K with respect to the room temperature of 28 °C was achieved at a current of 10 A. Figure 7.2 shows the temperature curves for different controller setpoints. It takes about 200 s until the temperature has settled.

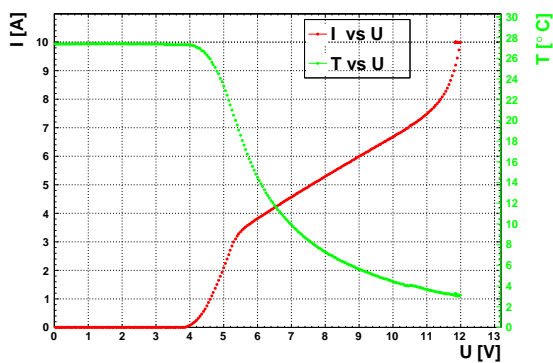


**Figure 7.1:** Current voltage characteristic for the 50 mm × 50 mm Peltier element H bridge combination. The recorded temperatures are measured inside the box in thermal equilibrium. As long as the nonlinearities of the U-I line are small PI-controlling is possible.

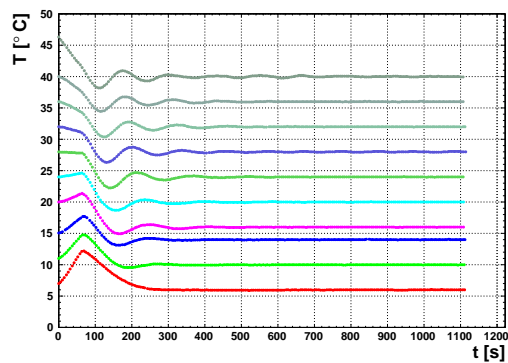


**Figure 7.2:** T [°C] vs time [s] for different controller setpoints. The temperature is kept constant with 0.1 °C accuracy. The curves refer to the setpoints 6, 10, 14, 16, 20, 24, 28, 32, 36 and 40 °C. Controlling starts at 75 s

## 7.2 Static characteristic

Via static behaviour of a SiPM one can access  $R_{quench}$  and  $V_{bd}$ . For obtaining  $R_{quench}$  one does a forward U-I scan of the device, for  $V_{bd}$  a backward scan is done.

### 7.2.1 Forward scan

The forward scan has been done using a Keithley 2400 (see datasheet Keithley [2002]) with a SiPM in series. The forward characteristic is governed by the typical diode equivalent resistance for voltages below ca. 0.7 V, the built in potential of a silicon diode. At higher voltages  $R_{quench}$  is the dominant resistance and the current behaves linear. The measurements were done at stable temperature of 20 °C under dark conditions and a current limit was set.  $R_{quench}$  can be obtained by fitting a straight line to the measured points in an adequate range and multiplying the SiPM resistance with  $n_c$ , the number of cells. In general the focus for the measurements was on Ham. 1x1 100C and on Ham. 3x3 100C type, due to its greater sensitive surface and higher fill factor  $\varepsilon_{geom}$ , because the limiting factor for position resolution of the POSSUMUS detector prototypes was the low light yield and therefore the most sensitive SiPM types were chosen. In this way the dynamic range of the devices used is smaller than for the other tested SiPMs, but this compromise is acceptable, because the mean number of photons was well below a level, where saturation effects occur. The results for the quenching resistance of the microcell from figure 7.4 can be found in table 7.3.

Type	$R_{SiPM}$ [ $\Omega$ ]	$R_{quench}$ [ $k\Omega$ ]
Ham. 1x1 025C	$168 \pm 1$	$270 \pm 2$
Ham. 1x1 050C	$303 \pm 2$	$121 \pm 1$
Ham. 1x1 100C	$1220 \pm 8$	$122 \pm 1$
Ham. 3x3 050C	$34.9 \pm 0.4$	$126 \pm 1$
Ham. 3x3 100C	$153 \pm 1$	$138 \pm 1$

**Table 7.3:** Quenching resistance and sum resistance of different SiPM types obtained by a linear fit to the forward voltage characteristic.

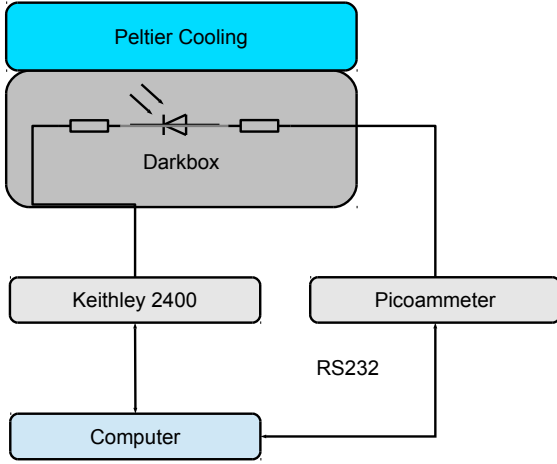


**Figure 7.3:** The setup for the measurement of the reverse U-I characteristic of a not illuminated SiPM. The voltage source is a Keithley 2400 and the current is measured by a Keithley 6515 Piccoammeter.

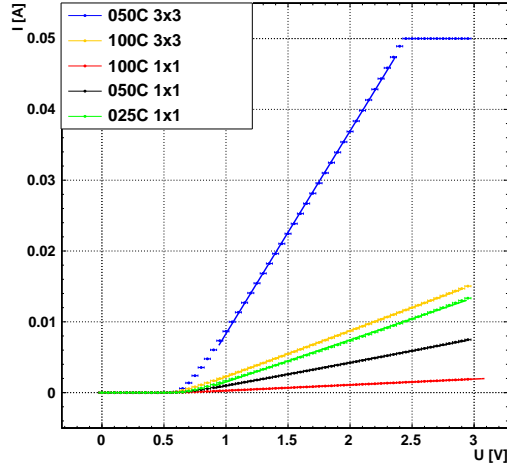


**Figure 7.4:** Current voltage forward characteristic measured for a bare SiPM with a Keithley 2400 voltage source at 20 °C

### 7.2.2 Reverse scan

$V_{bd}$  is accessible via the reverse current characteristic. For this the SiPM was connected to a test board with two 5 k $\Omega$  resistors in series (see figure 7.3). The voltage source was a Keithley 2400 and the current was measured using a Keithley 6514 electrometer (see datasheet Keithley [2003]). An automatic measurement system was developed increasing the sourced voltage until a current of 2  $\mu$ A was reached.

The current is given by the sum of the single APD signal, which can be described in a first approximation by the Shockley equation [see Dinu, 2013, pg. 12, 20, 172],

$$I = I_s (e^{V_{bias}e/(nk_B T)} - 1) \quad (7.1)$$

where  $I_s$  is the reverse bias saturation current,  $n$  is the ideality factor between 1 to 2. This equation ignores surface effects, carrier generation by thermal excitation inside the depletion zone and for high electric fields the tunneling of charges, as well as avalanche multiplication process above breakdown [see Dinu, 2013].

The current near the breakdown region has two components (see eq. (7.2)) - surface current and bulk current. For surface effects one has to consider, that the maximum electric field region is near the surface of the junction, which is contaminated with ion impurities during the fabrication process. These impurities may establish a conduction channel over the surface, when ions move in the latter due to high electric field effects. The bulk current is given by the thermally generated e-h pairs. Thermal generation takes place, when crystal impurities act as generation/recombination centers for e-h pairs via indirect transitions in the forbidden bandgap region. For a reverse biased depletion region it holds that the net charge generation rate  $U$  is given by  $U = \frac{n_i}{\tau_0}$ , where  $\tau_0$  is the effective lifetime of e-h pairs in the depletion region. Both variables depend on temperature and so  $U$  is a function of  $T$ . The approximately linear growth of pre-breakdown current is due to the growth of the depletion width, which results in greater volume where charge carriers are generated in the bulk and contributes linear to  $I_{bulk}$ .

For APD one has to consider a multiplication factor for the amount of charge, that flows through the avalanche region,

$$I_{pn} = I_{surface} + I_{bulk} \times M(V_{bias}) , \quad (7.2)$$

where  $M$  is the multiplication factor, which is related to  $G$  for a GM-APD. So for voltages below  $V_{bd}$  the current is dominated by the surface leakage component, whereas above breakdown the current is dominated by the bulk component. An approximation for the current above  $V_{bd}$  is

$$I_{V>V_{bd}} \approx e \times G \times DCR \propto e \times V_{over} \times V_{over} , \quad (7.3)$$

because the DCR rises approximately linearly with  $V_{over}$ . To extract a value for  $V_{bd}$  from the U-I characteristic the following fit function was used:

$$I(V_{bias}) = p[1] + p[2] \times V_{bias} + p[3] \times \theta(V_{bias} - V_{bd}) \times (V_{bias} - V_{bd})^2 \quad (7.4)$$

This holds for  $V_{bias}$  as long as the avalanche quenching time is much smaller than the recharging time constant  $R_{quench} \times C_{Cell}$ . For higher negative bias voltages the current through the junction approaches the asymptotic value  $I = V_{over}(R_{quench} + R_D) \approx V_{over}R_{quench}$ , where  $R_D$  is the variable diode cell resistance, and the amount

of charge contained in a single pulse increases more than linearly, because the avalanche quenching time increases with  $V_{over}$  [Dinu, 2013, p. 31]. This nonlinear behaviour is also amplified by the increase of afterpulsing processes with higher  $V_{over}$ .

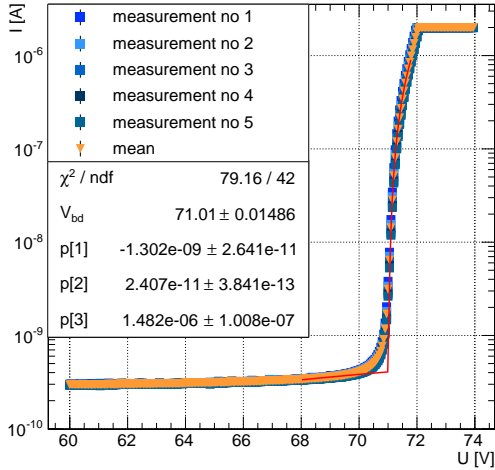


**Figure 7.5:** Current voltage reverse characteristic for a Ham. 3x3 050C in series with two 5 kΩ resistors at 20 °C. The measurement was repeated 5 times for reasons of reproducibility and combined. From the fit one obtains  $V_{bd} = (71.0 \pm 0.2)$  V.

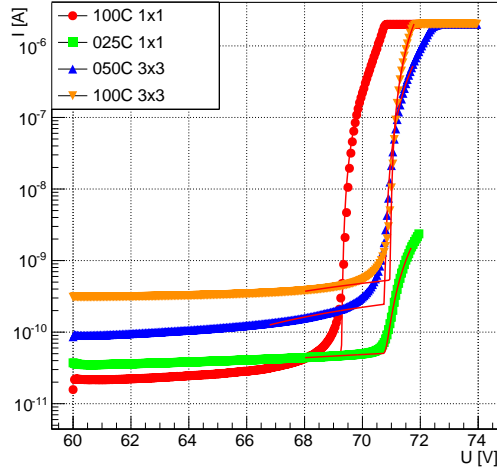


**Figure 7.6:** The U-I reverse characteristic for the tested SiPM types. The 3 mm × 3 mm models have greater leakage currents, because of the difference in area. The Ham. 3x3 100C type shows the steepest increase of current above  $V_{bd}$ .

Each U-I measurement is the combination of 5 repetitions (see figure 7.5). Figure 7.6 shows U-I characteristics for different SiPM types - green for Ham. 1x1 025C, red for Ham. 1x1 100C, blue for Ham. 3x3 050C, orange for Ham. 3x3 100C. Greater pixel size lead to steeper increase in current, because the single cell avalanche contains more charge and the DCR per area is greater for greater pixel sizes. If one assumes that  $U$  and the doping profile is similar for the different types, then the rate of charge carriers produced per area is the same and this leads to a greater current for higher pixel sizes. From the fitted function (7.4) one obtains  $V_{bd}$ . The problem of this fit, is, that the parameters must be preset carefully to obtain good fit results and that the range of the fit region is not clearly defined. In this case a range of up to 1 V above a estimated breakdown point and 2 V below this point

was used. A general expression for the nonlinear behaviour above  $V_{bd}$  was not found in the literature, . The two resistors in series have only small influence on the measured values, but they prevent accidental overbias. The fit parameter error for  $V_{bd}$  underestimates the error. The accuracy for  $V_{bd}$  is about 0.2 V and far greater than the errors from the fit, because the fit is sensitive to changes in the preset  $V_{bd}$  values.

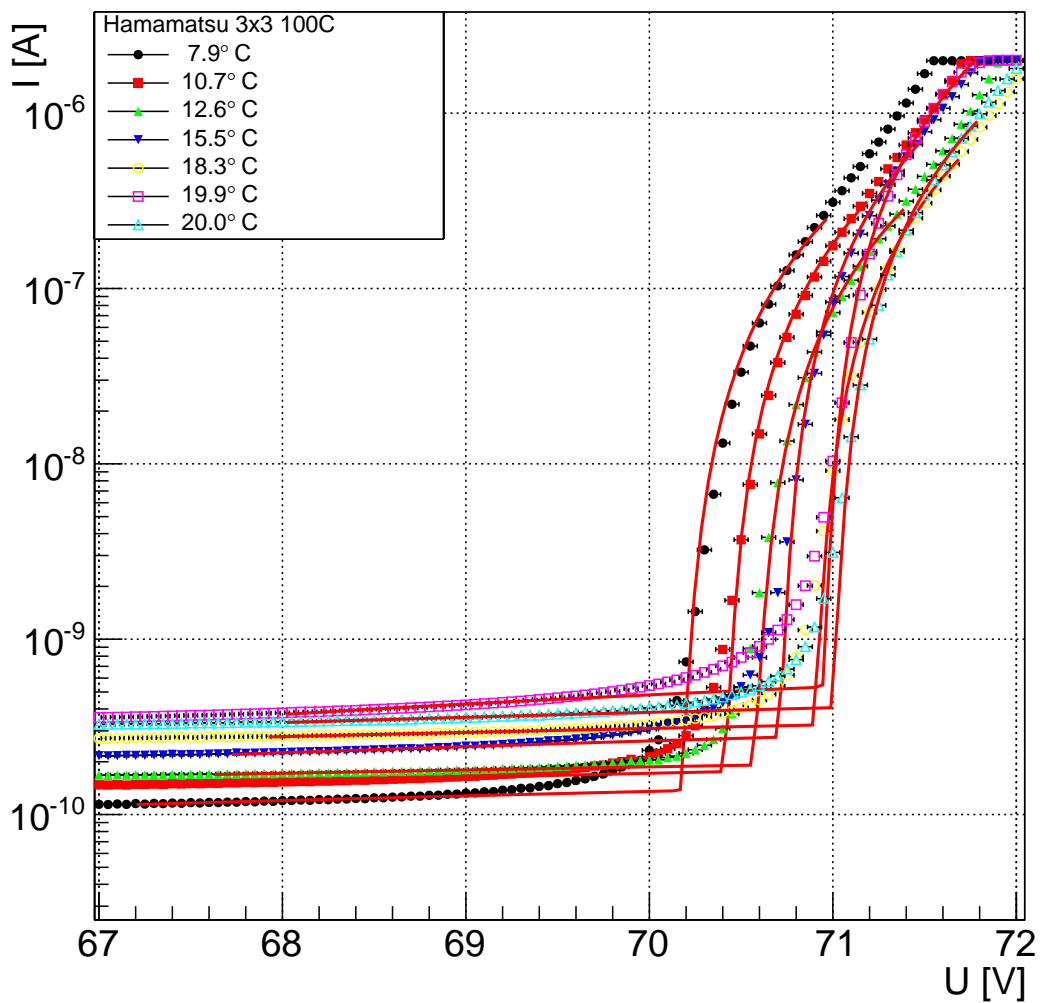


**Figure 7.7:** Current voltage reverse characteristic for a Ham. 3x3 100C SiPM in series with two 5 k $\Omega$  resistors at different temperatures. The temperature dependence of the leakage current and of  $V_{bd}$  is clearly visible.

Temperature studies for the Ham. 3x3 100C type have been done in order to investigate  $V_{bd}(T)$  and one can recognize the influence of temperature changes in the U-I characteristic (see fig. 7.7). From this measurement a temperature coefficient  $dV_{bd}/dT$  of  $(66 \pm 1) \text{ mV K}^{-1}$  was obtained (see figure 7.8). An alternative way of measuring  $dV_{bd}/dT$  and the interpretation of the results is presented in chapter 7.3.

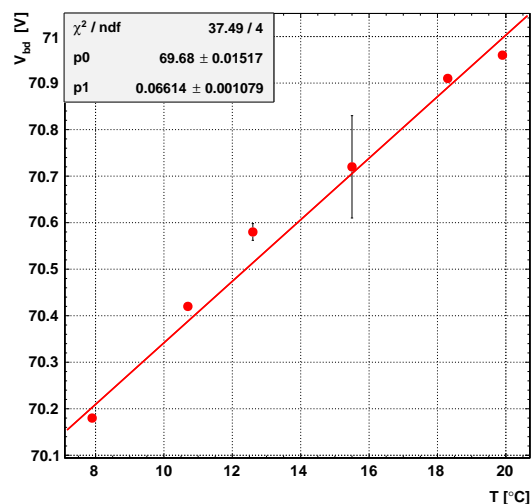


**Figure 7.8:** The temperature coefficient of a Ham. 3x3 100C via U-I characteristic, assuming a linear behaviour.

## 7.3 Dynamic characteristics

For the dynamic characteristics various SiPM were illuminated with short 8 ns LED light pulses [Caen, 2011a], such that the amount of triggered microcells was small (1 to 10 PE). The SiPM was mounted to a preamplifier board designed by Prothmann [2008, see pg. 22]. The amount of charge generated by a light pulse was recorded via a CAEN V792 12 bit QDC [Caen, 2010] within a 45 ns integration

gate. Considering the preamplifier Gain of 19.0 dB (amplitude ratio 8.91), the QDC conversion factor for the SiPM charge is:

$$Q[\text{C}](\text{QDC} - \text{chan}) = \frac{400}{4096} \times \frac{1}{8.91} \times \frac{1 \text{ pC}}{\text{QDC} - \text{chan}} \quad (7.5)$$

$$= 11.0 \times 10^{-3} \frac{\text{pC}}{\text{QDC} - \text{chan}} \quad (7.6)$$

The LED-driver triggers the QDC-readout (see fig. 7.10). Using this method, charge spectra have been recorded at different  $V_{over}$  and temperatures for different SiPM types. A picture of the setup in figure 7.9.

The obtained charge spectrum (see 7.11) is described by equation (3.31). In the so called finger spectrum one can clearly differentiate the number of microcells firing during a light pulse. Each peak represents a certain number of simultaneously triggered microcells. The left peak is called pedestal, when no cells have been triggered. For this analysis 11 peaks are fitted with a multigaussian fitfunction plus a gaussian background (7.7) and from the fit a probability distribution for the number of firing microcells was obtained, which is used in chapter 9. The gaussian background accounts for surface currents and dark counts, which smear out the gaussian peaks.

$$f(x) = A_{bg} \times \mathcal{N}(\mu_{bg}, \sigma_{bg}^2) + \sum_{i=1}^{n_{peaksfound}} A_i \times \mathcal{N}(\mu_i, \sigma_i^2) \quad (7.7)$$

$\mathcal{N}$  is a standard normal distribution. The spectra series contain information on  $G$ ,  $dG/dV$ ,  $dG/dT$ , the crosstalk probability  $p_{cross}$ , and via the distribution of the number of firing microcells one obtains the distribution for the mean number of impinging photons (see pg. 15).

Figure 7.12 shows the peak positions at different  $V_{over}$  relative to the pedestal peak. The fitted linear functions intersect at the breakdown point. The slope of the linear function of peak number 1 is proportional to  $dG/dV$ . In this work the breakdown voltage is calculated as the mean of the intersections of the lines from 1 to 3 PE. The reason why not more lines were used, is the fact, that the peak positions for higher order peaks do not depend linear on  $V_{over}$ , because the integration time is too short. But significantly longer integration times are not feasible, because dark

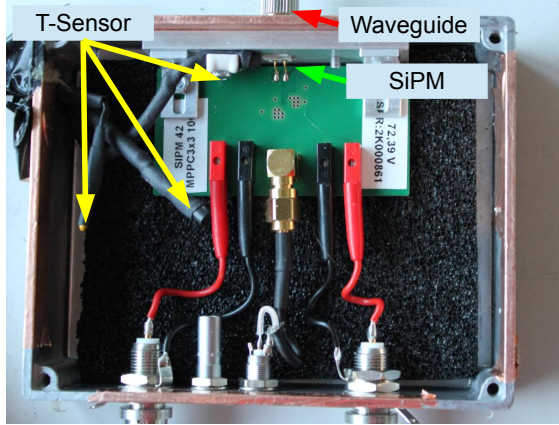


**Figure 7.9:** The setup for the SiPM characterization at low photon flux. The Clear Wave Guide (CWG) guides the light pulses with peak intensity at 400 nm. Two DS18B20 sensors were used to monitor the temperature inside the box.

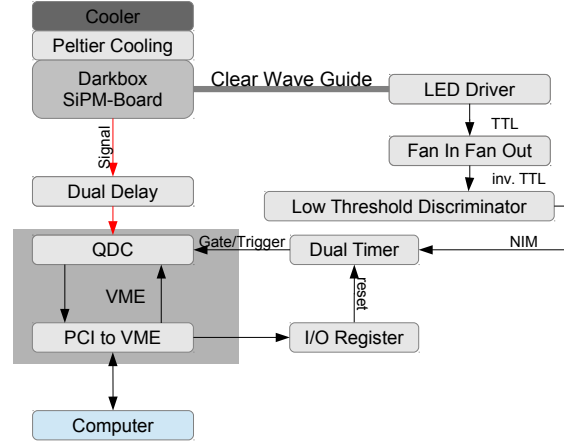


**Figure 7.10:** The readout scheme for the QDC-spectra.

counts prevent resolving the peaks and a spurious background builds up in the charge spectrum (see 7.11). The values for the tested SiPMs can be found in table A.1. The statistical error for the determined breakdown voltage is as follows,

$$(\Delta V_{bd})^2 = \frac{1}{9} \sum_{i=1}^3 \left[ \left( \frac{\Delta b_i}{a_i} \right)^2 + \left( \frac{b_i \Delta a_i}{a_i^2} \right)^2 \right] \quad (7.8)$$

where  $a_i$  and  $b_i$  correspond to slope and intercept of the  $i$ th line. Combining this with the systematic error of the voltage source (see Keithley [2002]) one obtains:

$$V_{bd} = (69.439 \pm 0.025(\text{stat}) \pm 0.039(\text{sys})) \text{ V} \quad (7.9)$$

For the Ham.  $3 \times 3$  100C  $dG/dV(T = 20\text{K}) \approx 8 \times 10^5 \text{ V}^{-1}$ . Consider a typical  $V_{over} = 1.5\text{V}$ , a compromise between PDE and crosstalk then it holds in the linear approximation:

$$\frac{dG/dV}{G} = 1/V_{over} \approx 0.067\% \text{ mV}^{-1}$$

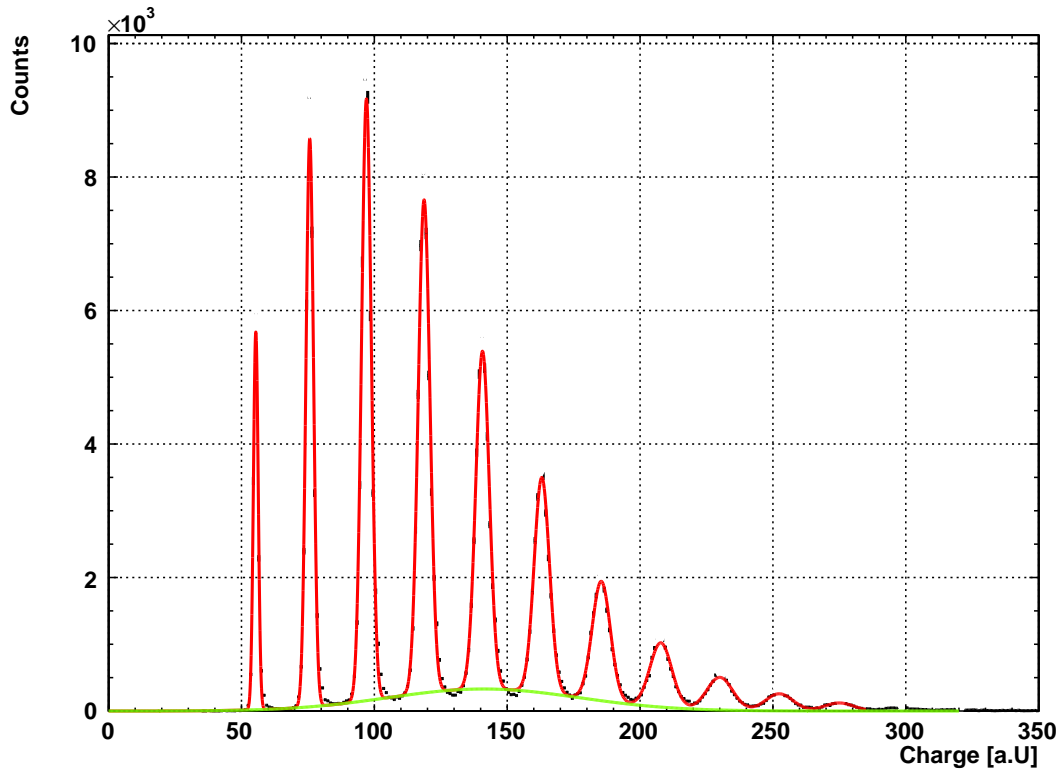


**Figure 7.11:** QDC spectrum (black) of a Ham. 1x1 100C at  $V_{over} = 0.6$  V with the multigaussian fitfunction (red) with gaussian background (green). The conversion factor for charge is 400/4096 pC per bin with preamplifier gain of 8.91.

This implies that the voltage source should be stable at the level off ca. 10 mV, that effects due to gain variations stay low. Higher  $V_{over}$  lead to significant increase in crosstalk and DCR and a compromise must be made.

Temperature studies show a temperature coefficient for the Ham. 1x1 100C of  $(60.8 \pm 0.6) \text{ mV K}^{-1}$  (see figure 7.13), which is in good accordance to the value measured with via the U-I method (see section 7.2.2). Deviations are probably due to the problematic fit procedure used for the U-I-characteristic. The signal height variation due to the temperature dependence of the BGA614 Darlington preamplifier gain is negligible. The bias resistance used for the amplifier was  $68 \Omega$  at  $V_{cc} = 5$  V [see Prothmann, 2008]. The temperature testing range was from approximately  $0^\circ\text{C}$  to  $30^\circ\text{C}$ , which implies a variation in device current of about

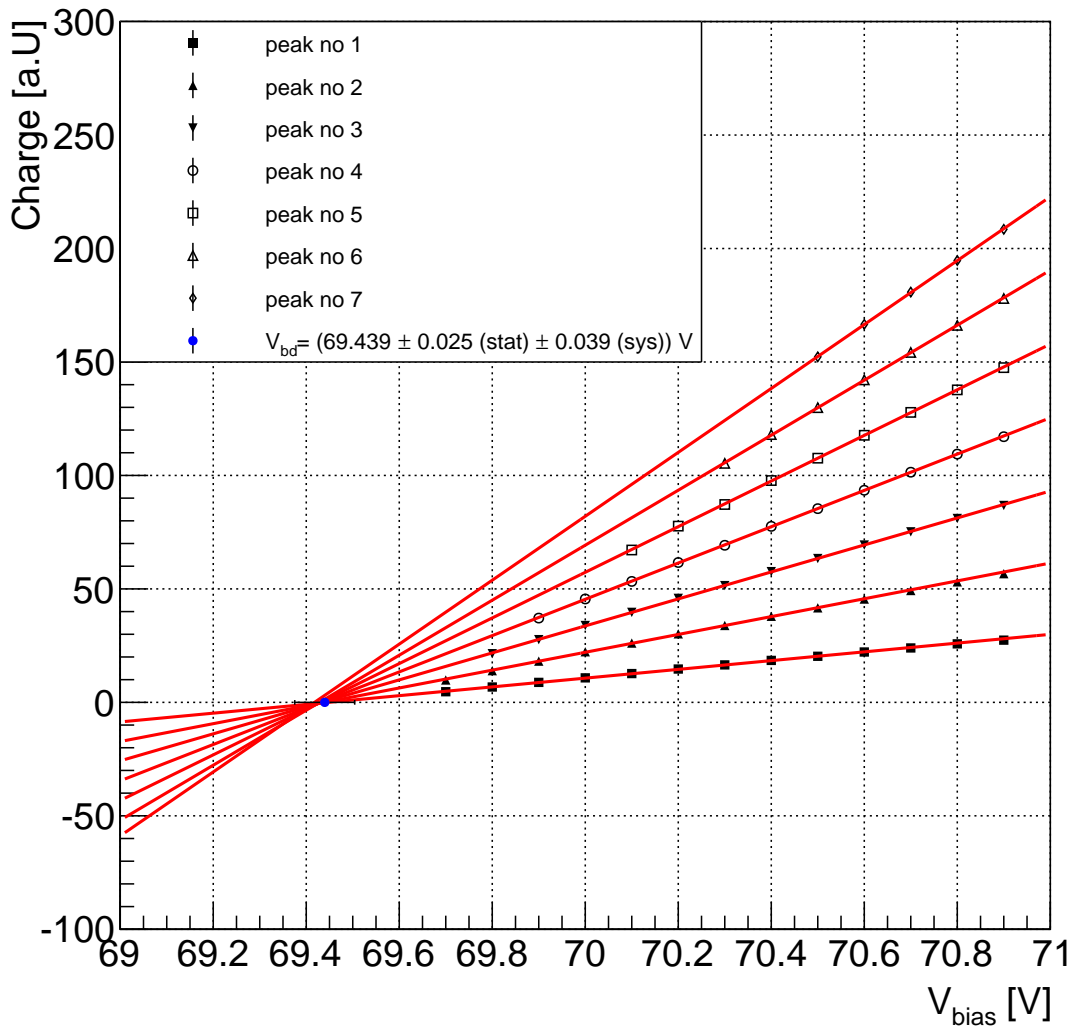


**Figure 7.12:** The peaks positions for various charge spectra of a Ham. 1x1 100C vs  $V_{bias}$ . The position of a peak depends linear on  $V_{over}$ . For higher order peaks this is not true, because the 45 ns signal integration time is too short for the signal. For this reason only the first 3 peaks were used for calculation of  $V_{bd}$

1 mA. The resulting variation in power gain is less than 0.1 dB at 19 dB [see Prothmann, 2008, pg. 35], which results in a temperature coefficient for the power gain variation in the order of  $0.1\% \text{ K}^{-1}$ . One concludes that the dominant factor for variations in the SiPM signal is the SiPM temperature coefficient.

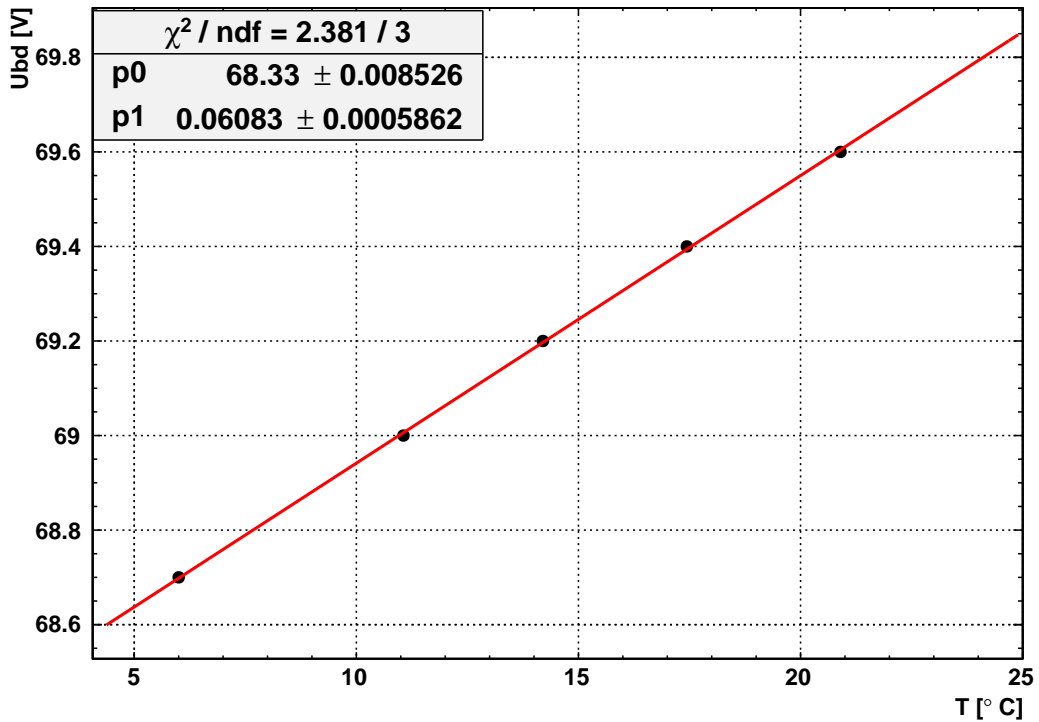


**Figure 7.13:** The temperature coefficient  $dV_{bd}/dT$  determined via charge spectra series at 5 different temperatures.

The reason why this temperature coefficient is positive, is the temperature dependence of ionization probability per unit distance travelled  $\alpha$  (impact ionization coefficient), which is a function of  $\epsilon_r$ , the optical phonon energy,  $\epsilon_i$ , the ionization energy, and  $\lambda$  the mean free path for generation of optical phonons. Using Barraffs theory Crowell [1966] showed, that in the high field region the temperature dependence of the ionization rate is dominated by a variation in  $\lambda$ , while the energy lost per unit path is nearly independent of the temperature. For higher temperatures the mean free path is smaller, which means, that a smaller fraction of the carriers

reach the energy necessary to generate further ionization, which results in a positive temperature coefficient for  $V_{bd}$ .



## CHAPTER 8

---

### SiPM gain stabilization

---

For SiPM it is essential to monitor and control  $V_{over}$ , because  $G$  and PDE depend on this parameter unlike for photomultipliers, where gain and quantum efficiency can be adjusted separately. The temperature dependence of  $G$  was investigated in chapter 7. The results show the greatest values for  $dG/dV$  for the 100  $\mu\text{m}$  Pixel size type. For the POSSUMUS detector, no active temperature control of the setup was applied and in this way a controlling mechanism for  $V_{bias}$  was required. Test measurements with the setup and readout from figures 7.9,7.10 were done, in order to check the performance of linear gain stabilization (see figures 8.2,8.2) and showed that the temperature dependence was reduced. Then a multichannel gain stabilization system was built, using 8 bit 20 k $\Omega$  RDAC as voltage divider for 5 V. The input of the temperature sensor, which is mounted on the metal beam next to the SiPM, is used with the temperature coefficient  $dV_{bd}/dT = 60\text{mV K}^{-1}$  to adjust  $V_{bias}$ . A sketch of the multichannel gain stabilization system can be found in figure 8.1. The system measures and records the temperature for each SiPM and the controlling threshold is a minimum temperature change of 0.3 K, limited by the resolution of the RDAC. Calibration measurements have been performed with the programmable voltage divider to check the uniformity of channels (see A.3). A long term measurement of 7 days was done to test the performance of the multichannel gain stabilization system.  $G$  is stabilized at best within  $\sigma$  at 0.92 % of the set  $G$  value (see table 8.1).

The design value of 20 k $\Omega$  for the maximum was chosen such, that under a load similar to a Ham. 3x3 100C the output voltage shows linear behaviour. The minimum load resistance is in the order of  $R_{load} \approx 70\text{V}/100\mu\text{A} = 700\text{k}\Omega$ , when the

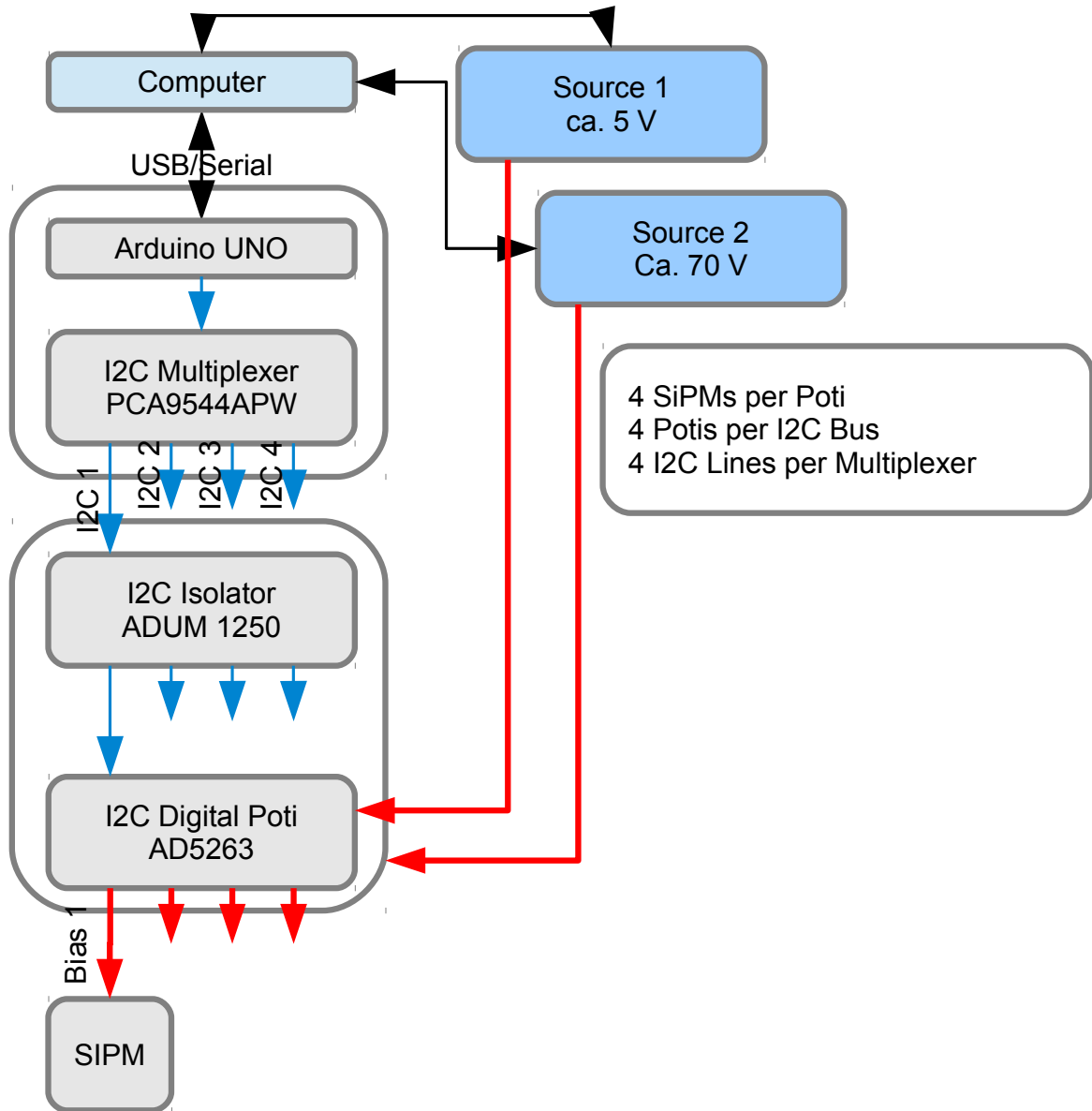


**Figure 8.1:** The multichannel gain stabilization system uses the I<sup>2</sup>C Bus to steer the voltage divider. The voltage divider uses a 5 V floating voltage source.

SiPM is saturated. The output voltage of the voltage divider with resistance  $R_1$ ,  $R_2$  without load is given by  $V_t = \frac{R_2}{R_1+R_2}V$ . If one includes the load resistance it reads

$$V_t = \frac{R_P}{R_1 + R_P}V, \quad (8.1)$$

where  $R_P = (R_{load}R_2)/(R_{load} + R_2)$ . The deviation of set voltage value from the real voltage is 25 mV at maximum (see figure A.4) and negligible, for SiPM at low photon flux.

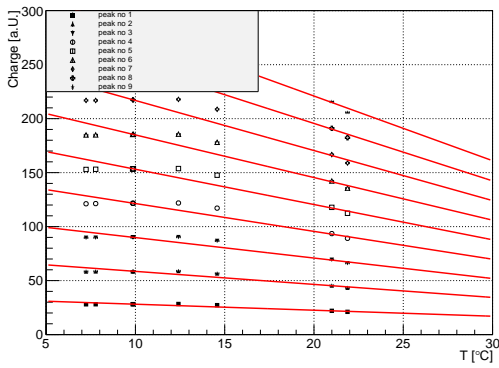


**Figure 8.2:** The peaks of the charge distribution spectra at different temperatures and constant  $V_{bias}$

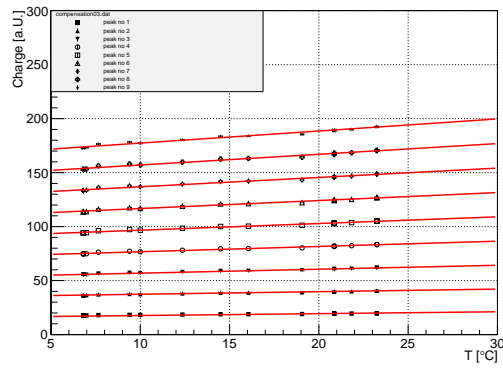


**Figure 8.3:** The peaks of the charge distribution spectra with temperature compensation via adjustment of  $V_{bias}$  using  $60 \text{ mV K}^{-1}$ . For this measurement the setup from chapter 7.3 was used.

Channel no.	RMS/Mean		Unit
	Uncompensated	Compensated	
0	4.5	0.92	%
1	4.7	1.3	%
2	5.7	0.97	%
3	6.3	1.3	%

**Table 8.1:** The goodness of G controlling algorithm. The values calculated with the measurement from figures A.6, A.7

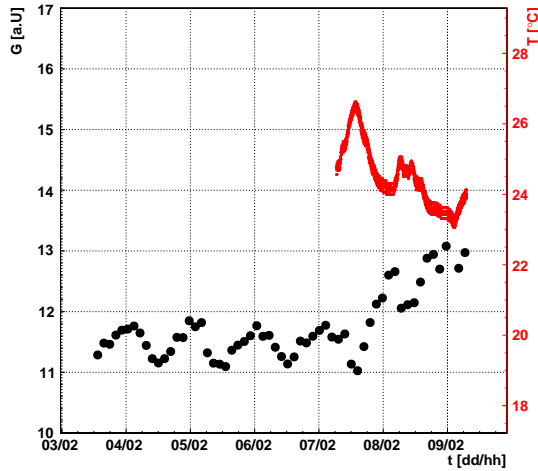


**Figure 8.4:** Gain monitoring without  $V_{bias}$  correction. The measurements were performed using a programmable LTD, switching between low threshold for Gain determination and the threshold for cosmic rays. For details see thesis Ruschke [2014]. Temperature recording started only later in the measurement.

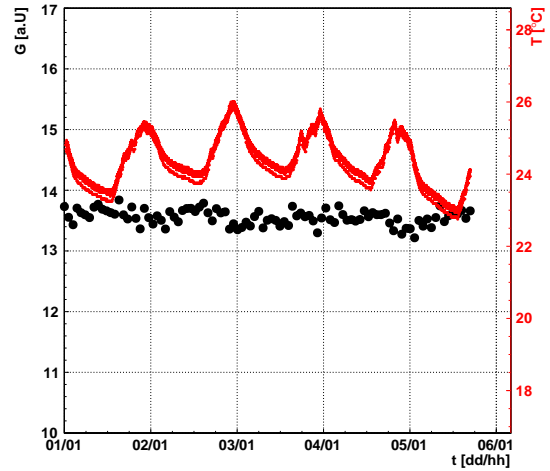


**Figure 8.5:** The peaks of the charge distribution spectra, when compensating temperature changes via adjustment of  $V_{bias}$  using  $60 \text{ mV K}^{-1}$ . The multichannel gain stabilization system uses the I<sup>2</sup>C Bus steer the 5 V floating voltage divider.

In figure 8.4 one can clearly recognize the day-night temperature variations in the lab. When the temperatures drop,  $G$  increases, whereas in figure 8.5 there is no long term trend visible and  $G$  fluctuates around a constant value.

## CHAPTER 9

---

### Model for the SiPM response

---

For the SiPM detector response function one has to consider, the distribution of the number of incoming photons, dark count rate (DCR), optical crosstalk (OC), photon detection efficiency (PDE). According to Ramilli et al. [2010] a simple model assumes a Bernoullian detection process, with the parameter PDE for a single photon to trigger an avalanche during the integration time. In this case the probability distribution of triggered microcells is given by a sum over the product of the distribution of impinging photons with a Binomial distribution. OC can be described as cascade phenomenon by a constant probability at a certain  $V_{over}$  for one cell to trigger another one, independent of the number of previously triggered cells and geometry effects. The time dependence of this process is also completely omitted, which is a good assumption, as long as the signal integration time is long in comparison to the time scale of OC. Several authors [Eckert et al., 2010, Finocchiaro et al., 2009, Ramilli, 2008] propose Poissonian statistics for the photon number distribution of a pulsed LED at low light intensities, which is directly connected to the initial distribution for the number of firing cells via PDE. This hypothesis is based on the assumption that the registration of photons is statistically independent during the counting interval [see Teich and Saleh, 1991, pg. 403,404]. Deviations from this behaviour originate in correlated events. These three parameters -  $\lambda_{Poisson}, PDE, p_{cross}$  - were used to generate a Monte-Carlo sample according to figure 9.1 in order to test the Poissonian hypothesis. Minimizing chisquare (see chapter A.1) the best fit-distribution was found, extracting the normalized probability distribution of equation (7.7) for the number of firing microcells from the finger spectrum in figure 7.11. Dark counts during the counting

interval of 45 ns are unlikely to happen at DCR in the order of 1 MHz and contribute about a few % to the mean value of the distribution of firing cells. For the spectrum of this SiPM data were available also on the value for  $p_{cross}(V_{over} = 1.1 \text{ V}) = 0.3$ , taken from Bollu [2014, see pg. 29,30], which was used to fix  $p_{cross}$ , for the minimization procedure. This was necessary, because a the global minimum for chisquare does not show sensible results for the model parameters.

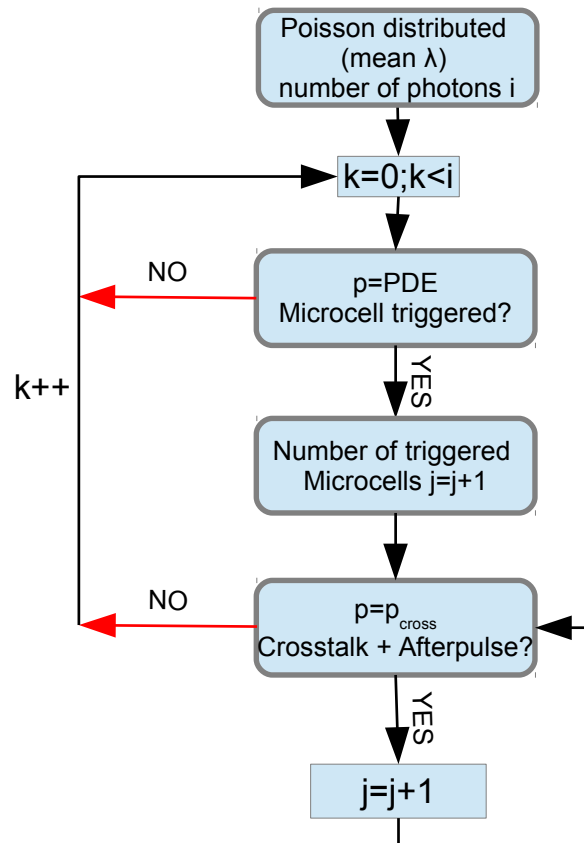


**Figure 9.1:** A simple model for the detector response using the Poisson hypothesis for low light intensities from pulsed LEDs.

The comparison of data and Monte-Carlo sample (see figure 9.2,9.3) reveals, that there is a good agreement for a higher number of firing cells, while especially at 0 to 3 firing cells, the agreement is not perfect. This may be an effect of omitting the spurious dark counts, which are indistinguishable from real hits. Dark counts result in a smaller probability for 0 firing cells and in greater probabilities for 1 and more firing cells. The fundamental difference to OC is, that for OC the 0 bin is not

---

affected, but true photon hits and OC events are shifted to higher bin numbers. For OC no upper limit of the maximum triggered cells was used, because the number of triggered cells is small compared to the total number of cells and even for higher order OC the density of triggered cells around the initially triggered cell stays small [see Otte, 2007, pg. 158]. More elaborated models for OC have been developed by Otte [2007], but these require a detailed knowledge about the doping concentrations in the cell structure, which is not provided by the vendor, as well as knowledge on the emission process of photons produced in the avalanche discharge. The latter includes the energy spectrum and the intensity of the emitted photons during the avalanche, which are object of actual research. The parameters obtained by the minimization procedure are  $PDE = 0.37$  at  $V_{over} = 0.6V$  and  $\lambda_{Poisson} = 4.2$ . Comparing with the value of  $PDE = 0.42$  measured at  $V_{over} = 1.4V$  by Dinu [see 2013, pg. 65], the minimization leads to sensible values. In this way an alternative method was found to obtain  $\lambda_{Poisson}$ , which is quite commonly determined using the information in the 0 bin with the total number of entries only and determining the number of incoming photons as  $\lambda_{Poisson} = -\ln \frac{N_{ped}}{N_{tot}}$ , where  $N_{ped}$  corresponds to the number of entries in bin 0 and  $N_{tot}$  represents the total number of entries in the histogram [Enzweiler, 2013, Glauß, 2012].

The chisquare plots (figure 9.4,9.5,9.6, note the logarithmic color axis.) with one parameter fixed show, that  $\lambda_{Poisson}$  and  $p_{cross}$  are anti-correlated, which is the expected behaviour, because crosstalk fakes photon signals and this leads to an overestimation of  $\lambda_{Poisson}$  (see figure 9.4). From figure 9.5 one concludes, the higher the mean of the incoming photons is reconstructed the less  $PDE$  is assumed. This result is at first sight astonishing, but may be connected to the Poisson hypothesis and the shape of the initial photon number distribution. It is probable that dark counts may cause this kind of behaviour, because of effects on the shape of the photon distribution, especially in the first bins. Figure 9.6 indicates that higher  $p_{cross}$  is connected to lower  $PDE$ , because given a higher crosstalk, which triggers additional cells, one may estimate lower values for  $PDE$ .

The Monte Carlo model showed, that it is problematic to determine the mean number of impinging photons with the number of entries in the 0 bin. A possible extension of the model is to use also the data on dark count rate, which may have effects on the discrepancies in the first bins.

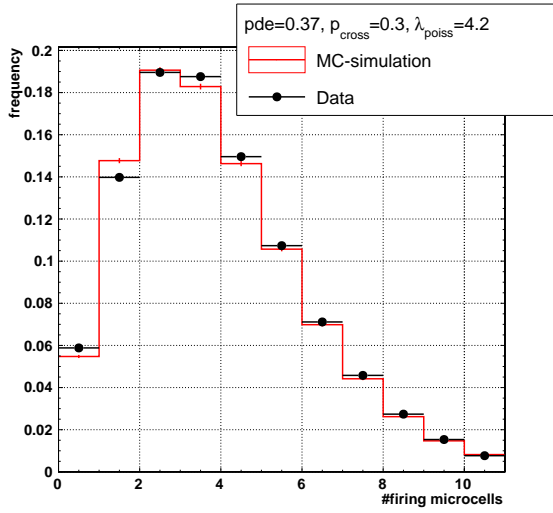


**Figure 9.2:** Data vs MC-simulation for a Poissonian number of photons in the LED-light pulse and the detector response model as in 9.1.

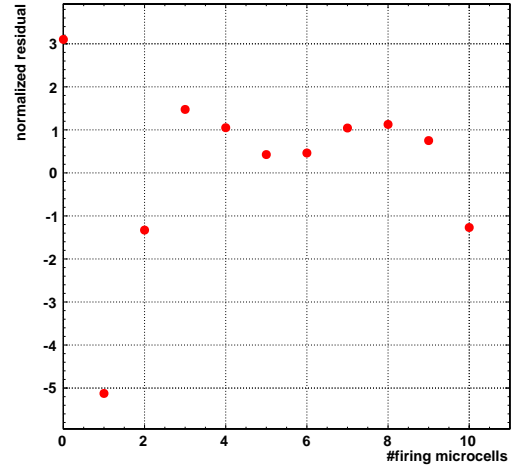


**Figure 9.3:** Normalized residuals

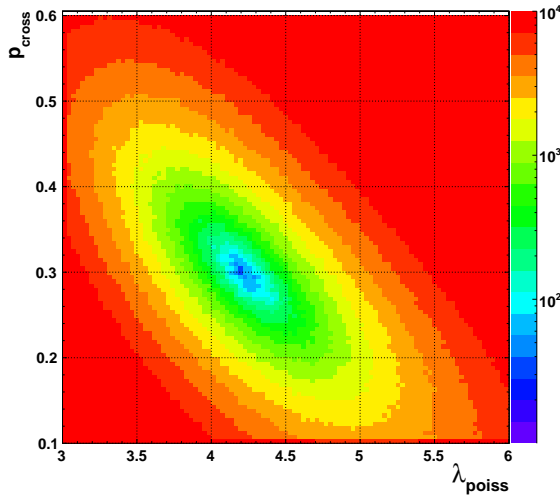


**Figure 9.4:** Chisquare distribution for  $p_{cross}$  vs  $\lambda_{Poisson}$

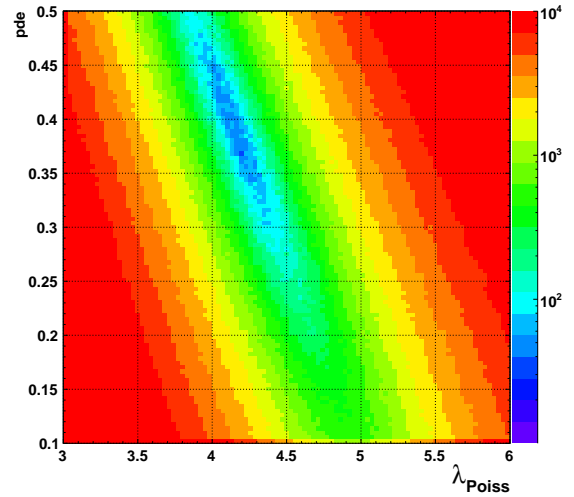


**Figure 9.5:** Chisquare distribution for  $PDE$  vs  $\lambda_{Poisson}$

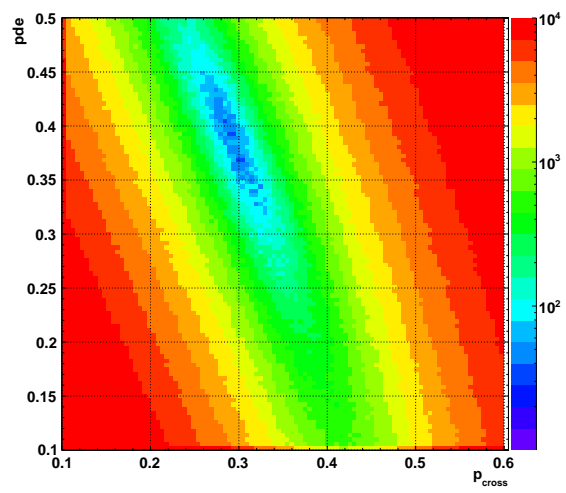


**Figure 9.6:** Chisquare distribution for  $PDE$   
vs  $p_{cross}$



# CHAPTER 10

---

## Tests on the time resolution and readout system

---

One goal for the POSSUMUS detector is a position sensitivity along the long side of the scintillator rods of 5 cm. In order to check the performance of the readout system, the scintillator rods and the SiPM timing, two scintillating fiber prototypes were constructed. For the latter BCF-12 scintillating fiber with 3.2 ns decay time, 435 nm peak emission and absorption length of 2.7 m with 5 mm diameter (see Saint-Gobain\_Crystals [2014a]) was used. The core refractive index is 1.6, while the cladding refractive index is 1.49. This prototypes were tested with a 20 MeV proton beam of 5 mm diameter at MLL-Garching tandem accelerator (see figure 10.1) in March 2014 and August 2014. The projected range of the protons along the beam axis inside a  $1.05 \text{ g cm}^{-3}$  polystyrene target (see BCF-12) as given in the NIST PSTAR ([NIST, 2014]) database is 0.41 cm, which means the protons stop inside the prototype.

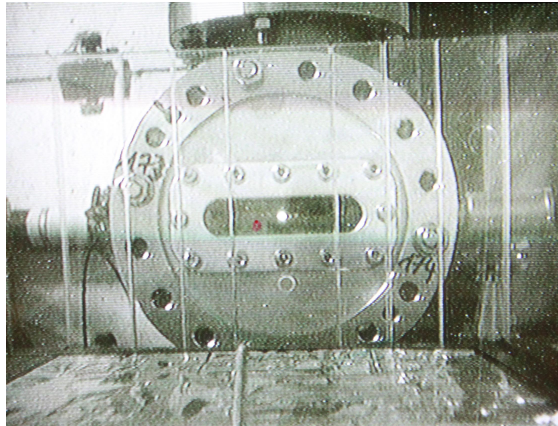


**Figure 10.1:** The 20 MeV proton beam hitting a scintillator tile. The 5 mm beamspot is clearly visible.

## 10.1 Photomultiplier-Fiber prototype

For this prototype a 1 m fiber was used and two Hamamatsu R1665 Photomultipliers were glued to the ends of the optically insulated fiber. The prototype was mounted to a step motor with 5  $\mu\text{m}$  minimum step size. In the experiment 35 cm horizontal movement was covered in 5 cm steps. The height of the prototype was adjusted to the position of maximum trigger rate of 170 Hz. The photomultiplier voltages were set to 800 V and 752 V, such that the pulse heights were equal at the center of the fiber. As voltage source a ISEG SHQ 224M was used (see datasheet ISEG [2014]).

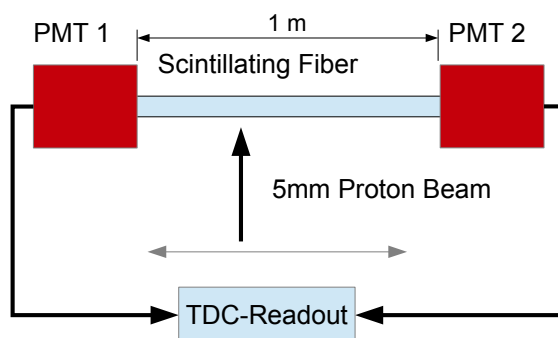


**Figure 10.2:** A sketch of the setup for testing the time-to-digital converter (TDC) readout.

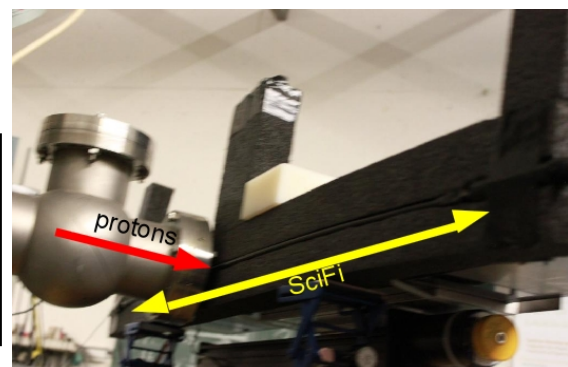


**Figure 10.3:** The scintillating fiber mounted to the stepper motor at the tandem accelerator facility.

A Caen N845 low threshold discriminator in combination with a Caen N455 coincidence logic unit with coincidence time of 40 ns was used to trigger a Caen V775N 12 bit TDC (see datasheets [Caen, 2004, 2011b, 2012]). One finds a sketch of the readout scheme in figure 10.4. The TDC was operated in common stop mode and the full range was set to 143 ns, so that the conversion factor is 34.9 ps per bin. The discriminator threshold was set to 30 mV, well above dark current of the photomultipliers. One finds the obtained TDC spectra for the different positions in figure 10.5. The right peak is the peak of the 32 ns delayed channel with a width of 1 bin standard deviation, which means, that the delay is sufficient and no triggers are generated by the second channel.

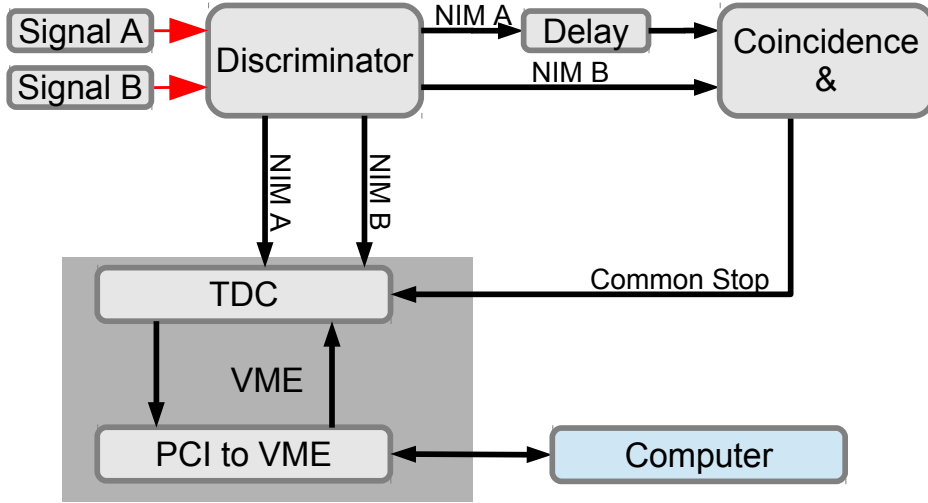


**Figure 10.4:** The TDC readout scheme. For the SiPM experiment a constant fraction discriminator with amplitude and risetime compensation triggering and for classical photomultiplier a low threshold discriminator were used.

The arrival time difference of the signals is given by

$$\Delta t = \frac{n_{core}}{c} \Delta x_{eff}, \quad (10.1)$$

where  $n_{core}$  is the refractive index of the core material,  $c$  the velocity of light,  $x_{eff}$  the effective way of light in the fiber accounting for reflections. A Gaussian function was fit to each of the spectra from fig. 10.5. The skewness of the distributions at the edges of the covered range may be an effect of light attenuation in the fiber and the constant threshold trigger technique. Considering the absorption length

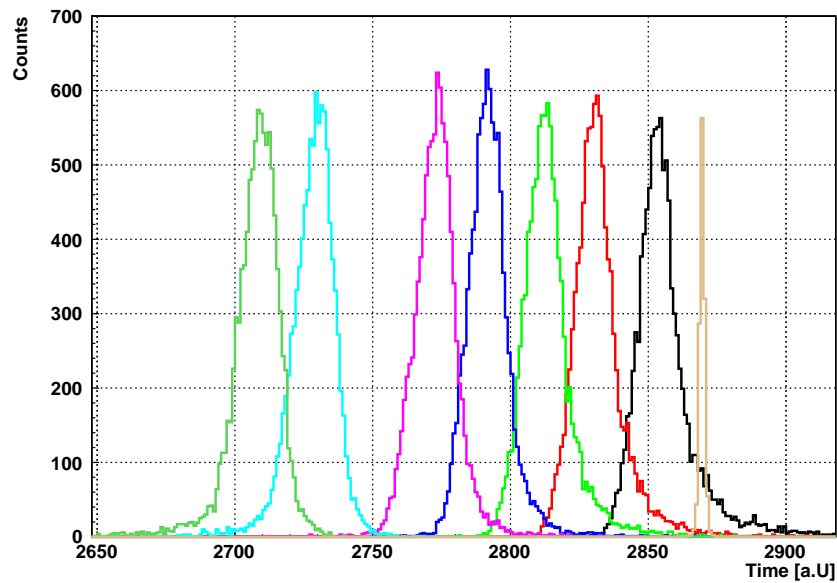


**Figure 10.5:** The time distribution of the photomultiplier signals at different detector positions. The right peak corresponds to the delayed channel. The step size is 5 cm. One position is missing. 10000 events were recorded at each position.

of 2.7 m one finds a difference of 12 % in intensity from edge to edge. From figure 10.6 one obtains  $(7.1 \pm 0.4) \text{ cm ns}^{-1}$  for the effective velocity of light. For this value  $8.5 \text{ cm ns}^{-1}$  has been reported by Chichester et al. [2012] for this material. The difference may be a calibration effect of the TDC or, because Chichester et al. [2012] used a longer piece of fiber. The used TDC was calibrated with a signal and delayed signal from 2 ns to 40 ns.

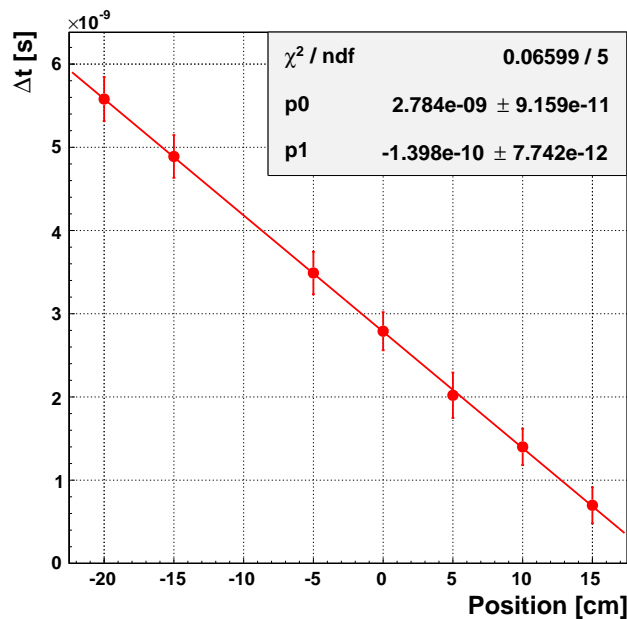


**Figure 10.6:** The time difference of the arrival times obtained by the Gaussian fit versus the detector position for the photomultiplier prototype. The effective velocity of light was  $(7.1 \pm 0.4) \text{ cm ns}^{-1}$ .

## 10.2 SiPM-Fiber prototype

The SiPM-Fiber prototype was built (see figure 10.7) in order to check the SiPM timing performance in comparison to classical photomultipliers. Two Ham.  $3 \times 3$  100C SiPM were glued with instant adhesive to a centering plastic structure at the polished ends of a 35 cm long scintillating fiber. The optically active surface of the SiPM was covered with Roth M500000 silicone fluid (now Wacker, see [Wacker, 2013]) with refractive index of 1.40 in order to improve the coupling to the fiber. As SiPM voltage source two EA PSI 8160-04T (see [Automatik, 2014]) were used. The readout electronics was as in figure 10.4, except that in place of the low threshold discriminator a programmable Caen V812 constant fraction discriminator (CFD) was used. The CFD uses amplitude and risetime compensating triggering technique (see glossary amplitude and risetime compensation triggering) with 4 ns delay time, accounting for the SiPM signal rise time and 150 ns dead time, which suppresses further triggers due to afterpulsing or time walk due to the temperature coefficient

of  $R_{quench}$ , which has effects on the shape of the signal during cell recovery. Apart from that, Constant Fraction Triggering has the advantage that the trigger signal is in theory independent from the signal height and time walk is minimized. A coincidence time of 40 ns was set. Gain compensation with  $60 \text{ mV } ^\circ\text{C}^{-1}$  temperature coefficient was implemented in a program, which takes the input of the DS18B20 temperature sensors and carries out the communication with the voltage source. The reference temperature for the set bias voltage is  $25^\circ\text{C}$ .



**Figure 10.7:** The SiPM-Fiber prototype with 35 cm long fiber and optical shielding. The SiPM was centered and glued to a plastic structure. A silicone fluid connects the active surface of the SiPM and the fiber.

For this prototype in a similar manner TDC spectra were recorded at the MLL tandem accelerator with 20 MeV proton beam as before. The step size was chosen to be 1 cm and the sample contains 50 000 events. One finds the time spectra for 7 different detector positions with 5 cm steps in figure 10.8. The skewness of the spectra is reduced compared to figure 10.5, which may be an effect of amplitude and risetime compensation triggering.  $V_{over}$  was equal for each of the SiPMs, nevertheless the height of the peaks decreases from left to right, which is an effect of the SiPM-fiber coupling. One channel may count fewer photons than the other and for this reason the time distribution broadens. For analysis a double Gaussian fit function for every peak was used, where the ratio of the amplitudes is about 4 : 1 (see figure 10.9). The mean values of the two Gaussians coincide within 1 bin and the ratio of the two sigma values is about 4/10.

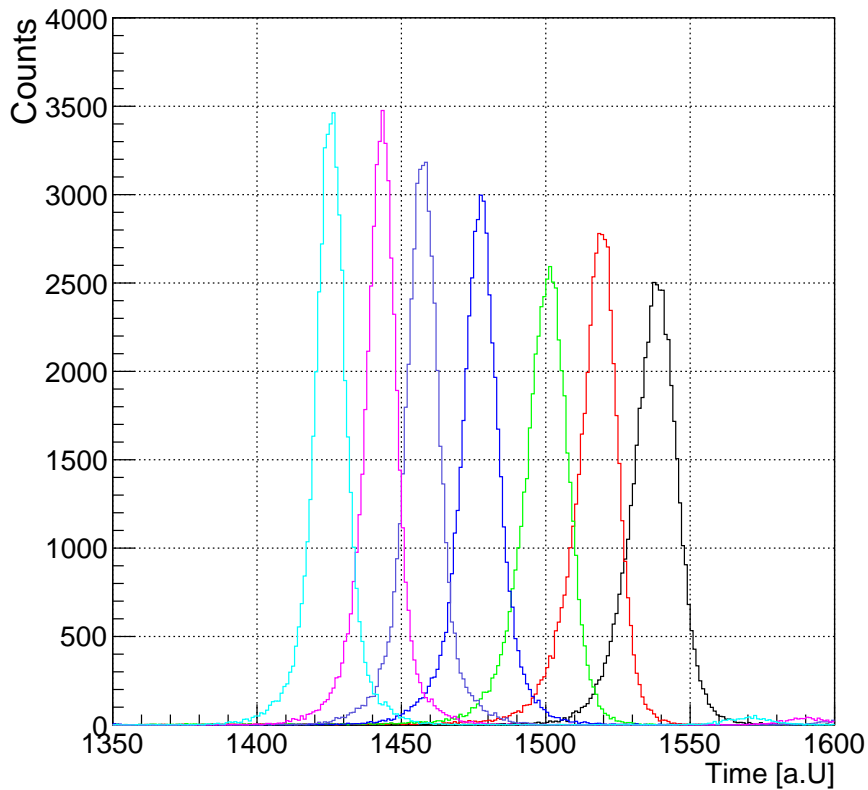


**Figure 10.8:** The time distribution of the SiPM signals at different detector positions. The scan step size was 1 cm, but for reasons of readability the position difference for the spectra is 5 cm. For each position 50 000 events were recorded.

The analysis (see figure 10.10) shows, that the position of the mean values is linearly dependent on the detector position. A slight peak broadening is visible, if the proton beam hits the detector at higher distances to one of the SiPMs. The overvoltage were set to be equal, so this may only be an effect of different SiPM-fiber coupling.

Table 10.2 shows the mean standard deviation of the Gaussian peaks converted to a distance with the conversion factor obtained as a combination of the two fiber measurements of  $7.15 \text{ cm ns}^{-1}$  (see figure 10.10, 10.6). The obtained position resolution as well as the measured effective velocity of light of the fiber detector prototypes are comparable. The effective velocity of light is governed by reflections

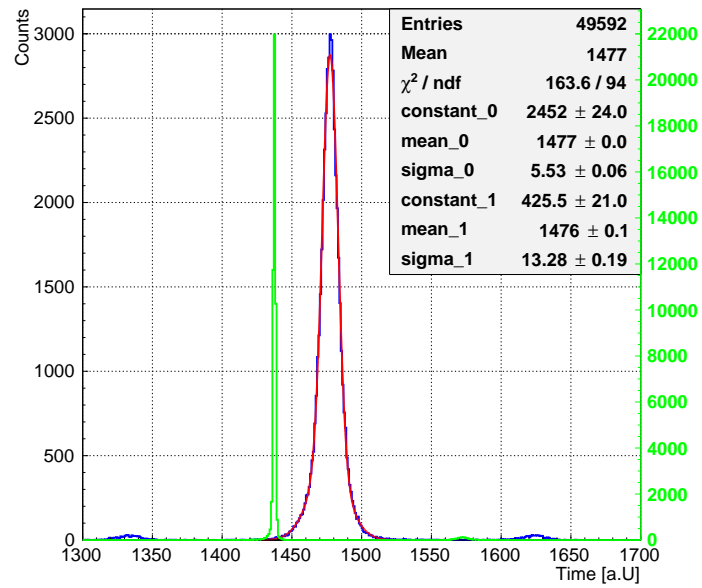


**Figure 10.9:** The time distribution at position 20.4 cm from the left SiPM, which corresponds to the blue peak in figure 10.8. A double Gaussian fitfunction was used. The green spectrum represents pedestal peak.

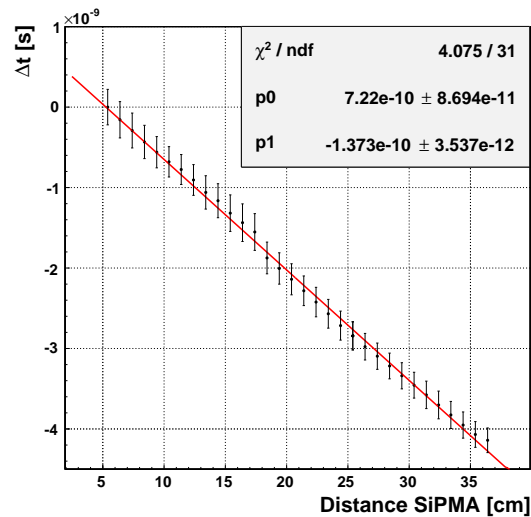


**Figure 10.10:** The position of the mean values of the dominant Gaussians, with sigma errors. The obtained effective velocity of light is  $(7.3 \pm 0.2) \text{ cm ns}^{-1}$ .

at the cladding material, and the broadening of the peaks is dominated by the scattering and reflection processes inside the fiber and the time pick-off method of the amplitude and risetime compensation triggering.

Prototype	$\sigma$ [cm]
Photomultiplier prototype	1.8
SiPM prototype Gaussian1	1.2
SiPM prototype Gaussian2	2.86

**Table 10.1:** Mean position resolution at  $1\sigma$  of the Gaussian fit to the time distribution. Gaussian1 and Gaussian2 refer to the double Gaussian used to fit the SiPM fiber prototype data. The values were calculated using the effective velocity of light obtained from the linear fit.

### 10.3 SiPM scintillator block prototype

Experiments at CERN (see [Ruschke, 2014]) revealed, that the position resolution for POSSUMUS via time difference of the signals was about 15 cm. The goal of this experiment was to decide, whether direct coupling of the SiPMs to a scintillator is better for the position resolution along the x-axis, than the readout via the WLSF. The advantage of direct coupling, is that more direct light hits the SiPM, while for indirect readout, the position, where the photons hit the fiber is uncertain and the absorption and reemission process broadens the time spectrum. In order to test this, a POSSUMUS prototype was built. The prototype is based on a 0.6 m long 40 mm  $\times$  90 mm rectangular BC-400 scintillator rod with a 1 mm diameter BCF-92 WLSF (see datasheet [Saint-Gobain\_Crystals, 2014b]) centered at 4.5 cm. The WLSF was placed in a 1 mm groove and glued to the scintillator rod with optical cement of the same refraction index. As wrapping material aluminum foil was used. At each end of the fiber a Ham. 3x3 100C SiPM (SiPM<sub>0</sub>, SiPM<sub>1</sub> see figure 10.11) was attached. In addition two Ham. 3x3 050C were glued with instant adhesive centered to both ends of the scintillator rods, which will be called SiPM<sub>2</sub> and SiPM<sub>4</sub> in the following. A printed plastic support structure fixes the prototype inside a light tight metal case. The readout used is the same as in section 10.2. The CFD threshold was set well above the dark rate of coincident signals. The proton beam hit the rod orthogonal to the surface with the WLSF. The detector was mounted to the stepper motor and moved in 10 cm steps orthogonal to the beam axis for a

length scan. The height was adjusted manually. The x-axis is defined along the long side of the scintillator, with 0-position at SiPM0 and the y-axis is defined along the 9 cm side, with 0-position at the upper end (see figure 10.11)

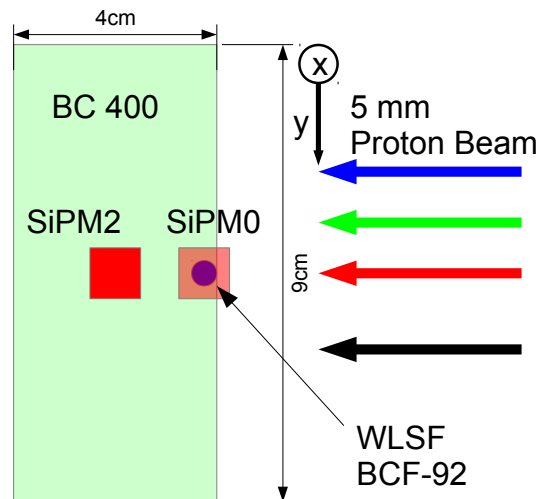


**Figure 10.11:** A POSSUMUS prototype with one centered scintillating fiber readout by SiPM 0 and SiPM1 at both ends. Additionally the scintillator is readout at both ends with a centered, direct coupled SiPM (SiPM2/4). The colors of the arrows represent the beam positions of the height scan.

Three scans have been performed with SiPM0/1:

- Height scan along the y-axis.
- Length scan along the x-axis in 10 cm steps at height 3.5 cm
- Length scan along the x-axis in 10 cm steps at height 2.5 cm

With SiPM2/4 a length scan at height 2.5 cm was performed in 5 cm steps.

### 10.3.1 Readout of WLSF with SiPM0/1

In this section the obtained spectra for the SiPM-fiber couplings shall be discussed.

The height scan in figure 10.12 shows the y-position dependence of the signal timing. Beam positions far from the fiber have a broad time spectrum, which is the expected behaviour.

Light is emitted isotropically mainly from positions near the Bragg peak of the proton beam, which is about 0.5 cm below the surface of the scintillator. Consider

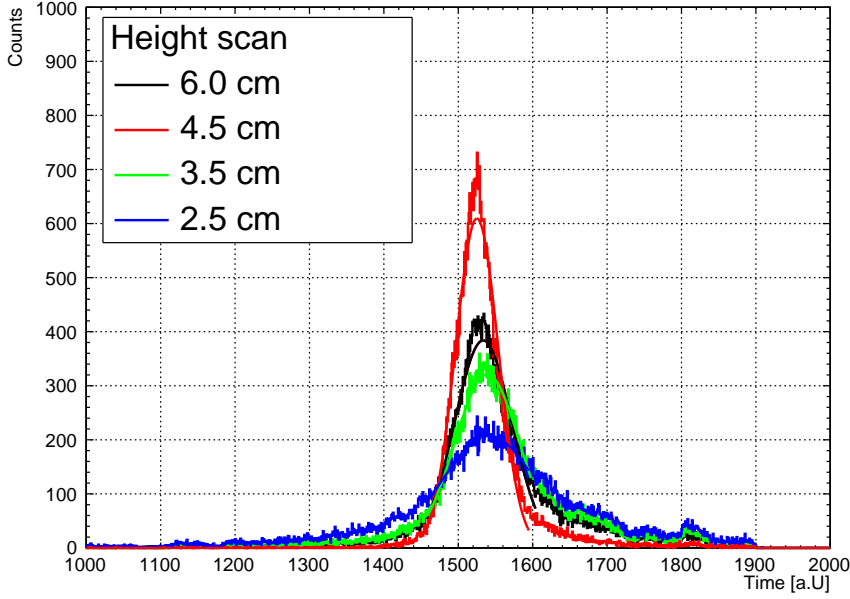


**Figure 10.12:** The height scan reveals a dependence of the time resolution on the distance of the proton beam to the WLSF. Positions far from the fiber at 4.5 cm have broad time spectra, while light generated close to the fiber shows narrow spectra. A Gaussian fit around the maximum of the spectrum was done. The fit parameters can be found in table

Height [cm]	$\sigma$ [ns]
2.5	2.17
3.5	1.52
4.5	1.00
6.0	1.34

**Table 10.2:** Mean standard deviation of the Gaussian fit to the time distribution from figure 10.12.

this a isotropic point light source. Then the photon flux without reflections at a point  $\Delta x$  (see figure 10.13) in the fiber is proportional to the intensity of a isotropic light source in distance  $r$  times the transmittance  $T$ , described by the Beer-Lambert law,

$$I_{pointsource}(1/r^2) \times T(r) = \frac{1}{\Delta x^2 + d^2} \times \exp\left(-\frac{\sqrt{\Delta x^2 + d^2}}{\lambda}\right),$$

where  $\lambda$  is the absorption length of the material,  $d$  the distance of the point source from the fiber,  $\Delta x$  the parallel component of the distance of the light source to a point on the fiber in figure 10.13. For reflected light the source appears to have a greater distance from the fiber and the shape of the distribution does not change. This contribution to the spectrum decreases rapidly with the number of reflections. Also the time for photons to reach the fiber increases with the number of reflections. A trigger is produced if the number of photons hitting both SiPM within the coincidence time is greater than a certain threshold. This indicates that the measured spectrum is a combination of the initial light and the photon absorption and reemission in the fiber and a smaller contribution from reflected light. This may be the reason why broadening occurs rapidly, when  $d$  increases. A slight asymmetry in the spectrum may be caused due to the low light output, which means that for one side less triggers are generated, in case the SiPM-fiber coupling is different.

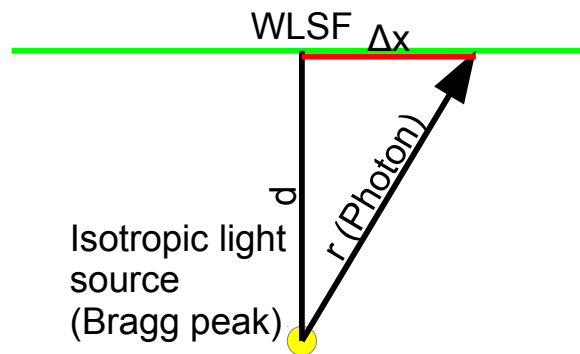


**Figure 10.13:** A sketch for emission of a point source and the photon absorption by a thin fiber.

Figure 10.14 shows the time spectra at different  $x$  positions along the scintillator at height 4.5 cm, figure 10.15 at height 2.5 cm. For analysis a Gaussian fit was done around a region of interest symmetric to the maximum. One finds a plot for  $\Delta t$ , as time difference of the converted Gaussian mean values, versus the positions in figure 10.17. From figure 10.17 via fit of a linear function one obtains an effective velocity of light (see table 10.3), which is comparable to the velocity of light in the BCF-12 fiber, but consists of two components. One is originated in the way of light in the scintillator, while the other component is due to the geometry of the WLSF.

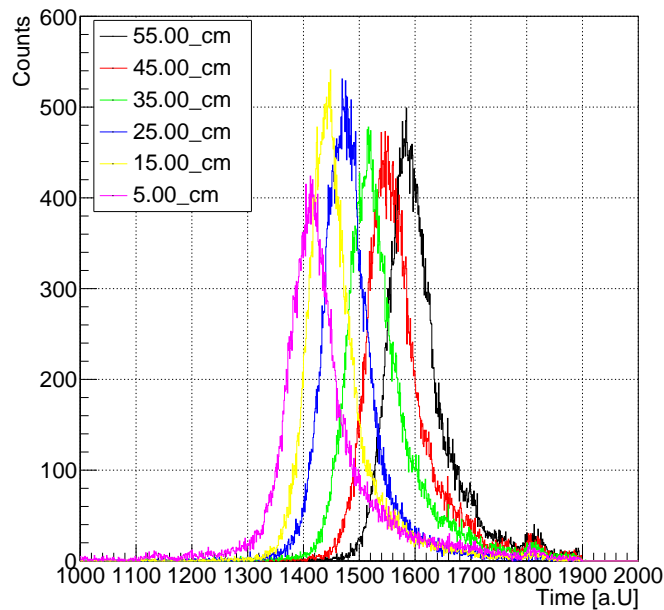


**Figure 10.14:** The time spectra for different x-positions at a height of 4.5 cm near the WLSF. For analysis a Gaussian was fit in a range symmetric to the maximum.

### 10.3.2 Direct readout of scintillator SiPM2/4

One idea to improve the position resolution obtained via the time distribution of the signals is to use two SiPMs coupled directly to the scintillator. The obtained time spectra one finds in figure 10.16. Characteristic for these spectra is that they have a broad background and a small peak, which results from the reflected direct light component. The effective velocity of light (see figure 10.17) is smaller than with the SiPM fiber coupling configuration, which is probably an effect of the high probability that multiply reflected light triggers the SiPM. In figure 10.18 a typical spectrum for the direct coupling can be seen. The problem of this method is, that the peak consists of very few events, which is due to a bad detector efficiency. This rules out the direct coupling option as detector concept.

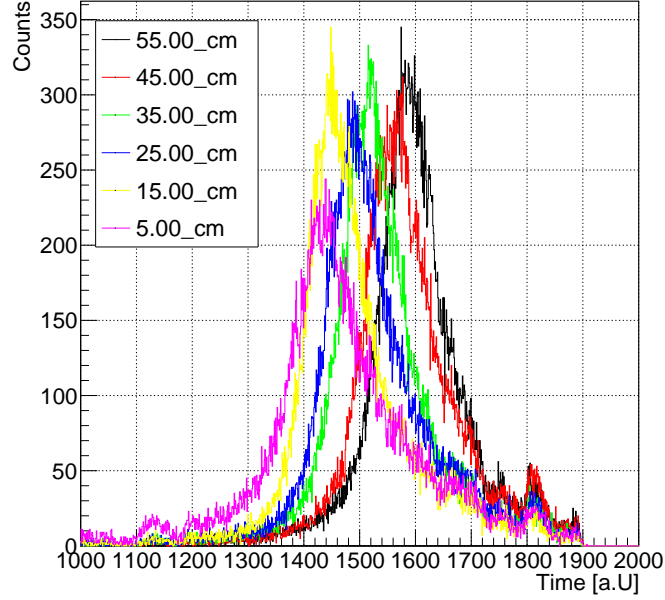


**Figure 10.15:** The time spectra for different x-positions at a height of 2.5 cm, far from the WLSF. The distributions are broader because of geometrical effects.

Sample	$c_{eff}$ [cm ns <sup>-1</sup> ]	Spat. res ( $\sigma$ ) [cm]
Fiber readout $h = 4.5$ cm	$8.01 \pm 0.01$	10
Fiber readout $h = 2.5$ cm	$8.98 \pm 0.03$	16
Direct readout $h = 2.5$ cm	$5.38 \pm 0.02$	10

**Table 10.3:** The obtained effective velocities of light and the mean width of the Gaussian fit function in units of cm. Note that the real error on the  $c_{eff}$  is underestimated.

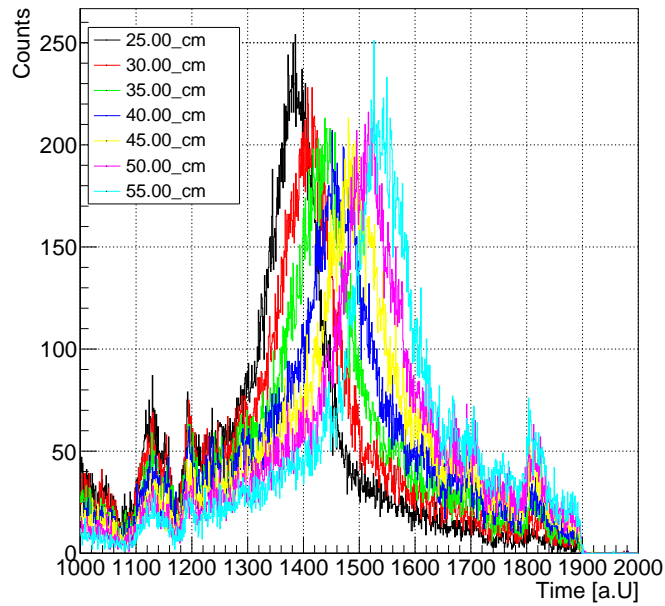


**Figure 10.16:** The time distribution spectra for direct coupling of two Ham. 3x3 050C to the scintillator. A broad background due to the low light output is visible.

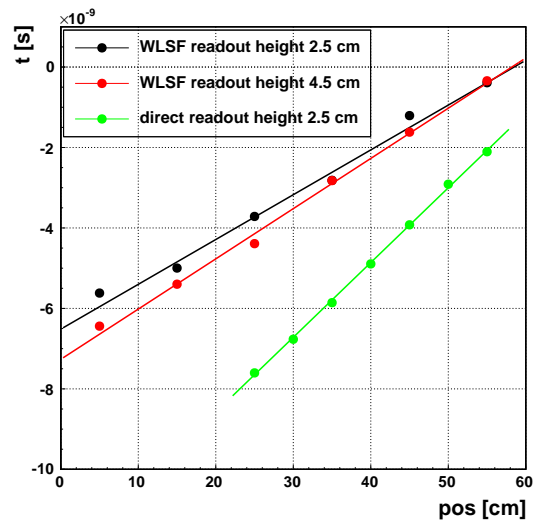


**Figure 10.17:** The position of the mean values obtained by the Gaussian fit to the region of interest symmetric to the maximum value of the time spectrum. The error bars are the fit errors on the mean of the Gaussian, which probably underestimate the true error.

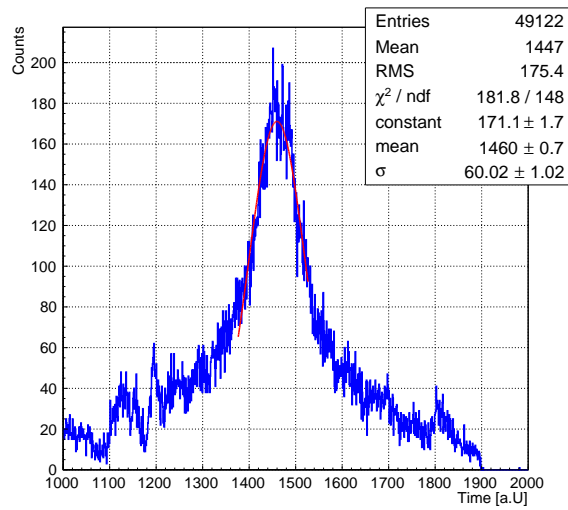


**Figure 10.18:** The time spectrum for direct readout at 40 cm. The number of events inside the fit range is about 40 % of the total events. This means, that the detection efficiency is too low for a good separation of background events from protons.

# CHAPTER 11

---

## Conclusion and outlook

---

The goal of this work was the optimization of a fast scintillation detector for a large areas with SiPM readout and trigger capability. The detector consists of BC-400 scintillator rods, BCF-92 fibers glued to the scintillator. The light emitted at the end of the fiber is collected with SiPMs.

This work consists of two parts. In the first part different SiPM types were characterized. For the latter a temperature controlled (0.1 K) test setup was developed, which was used for automatically determining  $V_{bd}$ ,  $dG/dV$ ,  $dV_{bd}/dT$  and  $R_{quench}$ . Via a the forward U-I scan the microcell resistance  $R_{quench}$  has been measured for 5 different SiPM types. For the reverse U-I scan the breakdown voltage of different SiPM types was reconstructed using a linear-quadratic function. Temperature studies were performed to determine the temperature coefficient via this method. The parameters  $dG/dV$ ,  $dV_{bd}/dT$  and  $V_{bd}$  have been measured automatically, illuminating the SiPM with a pulsed LED. The charge contained in the signal pulse was recorded at different voltages and charge spectra were generated. A multigaussian fit function was used to describe the spectrum and in this way  $V_{bd}$  was measured at high precision with an error of 64 mV. From the position of single pixel peaks at different bias voltages  $dG/dV$  is obtained. These parameters have been determined for about 30 SiPMs of different form factors and microcell sizes.  $dG/dV$  is largest for the SiPMs with 100  $\mu\text{m}$  cell size and smallest for 25  $\mu\text{m}$  cells, which puts an upper limit for the accuracy of the voltage source. The determination of  $V_{bd}$  was necessary, because the vendor only gives a recommended bias voltage, which is greater than  $V_{bd}$ . Measurements with the POSSUMUS prototypes had shown, that the low light output was the main issue in order to improve the position resolution.

The decision was made to use SiPMs with microcell size of  $100\ \mu\text{m} \times 100\ \mu\text{m}$ , because of their greater photon detection efficiency. For this SiPM type a temperature coefficient  $dV_{bd}/dT$  of  $60\ \text{mV K}^{-1}$  was measured, which is in good accordance to the obtained value via the U-I method.

Due to temperature fluctuations in the laboratory it was important to build a system, that reduces the effects of gain variation. For this purpose the automatic multichannel SiPM gain stabilization system has been developed, which minimizes the gain variation due to temperature dependence of  $V_{bd}$ . This system relies on the input of the temperature sensor mounted to the SiPM board and corrects the bias voltage according to the measured temperature coefficient. The circuit is based on a digital controlled voltage divider. The gain could be stabilized within 0.92 % and no long term drifts were visible.

In order to understand the effect of crosstalk on the distribution of the number of firing microcells a simple Monte Carlo detector response model has been developed. The model contains no information on the microcell structure and is therefore applicable to a wide range of SiPM types. Comparison with data shows sensible results, indicating, that the Poisson assumption for the number of incoming photons is good. The model includes crosstalk and afterpulsing effects and the photon detection efficiency. In the range from 0 to 3 firing microcells one finds the largest deviations of the simulated data from the measured spectrum, which may be an effect of dark counts, which have not been included in the model.

In the second part of this work studies on the position sensitivity along the long side of a POSSUMUS prototype were done. For this purpose three detector prototypes were built, which were tested with a 5 mm, 20 MeV proton beam at the MLL-Garching. Two prototypes are based on a 5 mm diameter BCF-12 scintillating fiber and were used to test the timing capabilities of the readout system and the used SiPMs. One of those prototypes was coupled to conventional photomultipliers, the other one to Ham.  $3 \times 3$  100C SiPMs. Time spectra were recorded and from these one obtains a position resolution of 1.8 cm for photomultipliers, 2.86 cm for SiPM readout.

The POSSUMUS prototype consists of a 60 cm long,  $4\ \text{cm} \times 9\ \text{cm}$  rectangular scintillator with a 1 mm BCF-92 fiber glued centered, parallel to the x-axis, which corresponds to the long side of the scintillator. The POSSUMUS prototype was scanned with the proton beam along the y-axis and the time spectra show, that

---

the position resolution via the time information depends on the distance from the proton beam to the fiber. The Gaussian width of the time distribution near the fiber was measured to be 1 ns and decreases rapidly with the distance to the fiber.

From a scan along the 0.6 m long side of the scintillator rod one obtains a mean position resolution of 10 cm near the fiber and 16 cm at a distance of 2 cm parallel to the fiber. For direct readout with two SiPMs centered to the 9 cm  $\times$  4 cm surface of the scintillator, the position resolution is 10 cm but the detection efficiency is too bad to consider this an improvement of the detector. The limiting factor in the time measurement is the transit time jitter of the photons in the scintillator, while electronic effects, scintillation process and electronic noise play a minor role. This indicates, that for obtaining a position resolution of 10 cm along the x-Axis, other methods of analysis e.g. combining pulse height and timing information, must be considered or other scintillator geometries should be tested.

Further improvements of the position sensitivity along the long side of the detector may be achieved by adding more fibers to the detector such, that the spacing between the fibers is about 1 cm or less. Furthermore for better light collection a Winston cone like scintillator may be glued to the ends of the long side or fiber couplers, which join several fibers together, could be used. SiPM readout of each cone will improve the SNR in contrast to direct readout of the flat scintillator surface and may have small effects on time information.

Considering the used SiPM the difficulty was to stabilize gain at high precision, because optical crosstalk puts an upper limit for the feasible  $V_{over}$ . Recent developments of SiPM with reduced optical crosstalk can be biased at higher  $V_{over}$ , which may increase the photon detection efficiency, reduce the requirements for gain stabilization and extend the linearity of the detector response. The gain stabilization system may be improved using a feedback signal, which is computed from the SiPM single pixel signal. A drawback of the current system is, that for gain monitoring purpose the readout of high energetic events must be stopped. The detector is operated by switching the discriminator thresholds between gain monitoring level using the dark rate and the level for signals from incoming particles. For constant gain monitoring a second high gain readout channel for each SiPM is recommended, which uses the full dynamic range of the charge-to-digital converter (QDC).

This work has shown, that SiPMs are suited as a readout for the POSSUMUS detector and that the detector principle has been proven. An automatic test setup was used to characterize the SiPMs used for the detector. The goal of a position resolution of 10 cm could not be achieved with the current detector prototypes, but the limiting effects are well-known and ways to improve the resolution were mentioned.

# APPENDIX A

---

## Appendix

---

### A.1 The Chi-Square Test for comparison of experimental and simulated data

Weighted histograms can be obtained from a Monte Carlo Simulation and experiment. Comparing data and the Monte-Carlo data one possibility to get an estimate of the goodness of the model is the Chi-Square Test, which shall be derived in the next section. The following is a sketch of the Chi-Square method as presented in Gagunashvili [2010]:

The probability for a random event to belong to bin  $i$  of a histogram with  $m$  bins is given by the integral over a region  $S_i$  of the underlying PDF:

$$p_i = \int_{S_i} p(x) dx, \quad i = 1, \dots, m \quad (\text{A.1})$$

A histogram with  $m$  bins states the result of a random experiment with the PDF  $p(x)$ . The homogeneity hypothesis assumes that two histograms have identical underlying probability distributions, which is equivalent to:

1.  $\sum_{i=1}^m p_i = 1$
2.  $p_i$  = probability for a measured value to belong to the  $i$ th bin

### A.1.1 Unweighted histograms

Now define the total number of events in histogram  $j$  belonging to the  $i$ th-bin as  $n_{ji}$  and

$$X_j = \sum_{i=1}^m \frac{(n_{ij} - n_j p_i)^2}{n_j p_i} \quad j = 1, 2 \quad (\text{A.2})$$

a random variable, which has a  $\chi_{m-1}^2$  distribution (see glossary Chisquare Distribution), where the histogram number  $j$  is represented by  $j$ , because the Chisquare Distribution is the distribution of the sum of the squares of a number of independent standard normal random variables. Now for statistically independent histograms:

$$\sum_{j=1}^2 X_j = \sum_{j=1}^2 \sum_{i=1}^m \frac{(n_{ij} - n_j p_i)^2}{n_j p_i} \quad (\text{A.3})$$

is approximately distributed as  $\chi_{2m-2}^2$  and the probabilities  $p_1, \dots, p_m$  are obtained by minimization of equation A.3.

One estimates  $p_i$  by the following expression:

$$\hat{p}_i = \frac{n_{1i} + n_{2i}}{n_1 + n_2} \quad (\text{A.4})$$

Substitute A.4 in A.3 one obtains:

$$\sum_{j=1}^2 \sum_{i=1}^m \frac{(n_{ij} - n_j \hat{p}_i)^2}{n_j \hat{p}_i} = \frac{1}{n_1 n_2} \sum_{i=1}^m \frac{(n_2 n_{1i} - n_1 n_{2i})^2}{n_{1i} + n_{2i}} \quad (\text{A.5})$$

Where the expression in A.5 is  $\chi_{m-1}^2$  distributed with estimation of  $m - 1$  parameters.

### A.1.2 Weighted histograms

In analogy for weighted histograms we define

$$p_i = \int_{S_i} p(x) dx = \int_{S_i} w(x) p(x) dx \quad (\text{A.6})$$

as the integral in a given region of the product of a weight function

$$w(x) = p(x)/g(x) \quad (\text{A.7})$$

and  $p(x)$ , where  $g(x)$  is an arbitrary PDF. Further it holds:

$$\begin{aligned} g(x) > 0 & \quad \forall x \in X = \{\bar{x} : p(\bar{x}) \neq 0\} \\ w(x) = 0 & \quad \forall x \in Y = \{\bar{x} : p(\bar{x}) = 0\} \end{aligned} \quad (\text{A.8})$$

Define normalized weights as  $w(x)$  and in analogy unnormalized weights:

$$\tilde{w}(x) = \text{const} \cdot w(x) \quad (\text{A.9})$$

The sum of weights is given by:

$$W_i = \sum_{k=1}^{n_i} w_i(k) \quad (\text{A.10})$$

$n_i$  number of events in bin  $i$  and  $w_i$  weight of  $k$ th event in the  $i$ th bin. So that the total number of events in the histogram is given by  $n = \sum_{i=1}^m n_i$

To do the test of homogeneity we define the statistics:

$$X_h^2 = \sum_{i=1}^m \frac{(W_{1i} - W_{2i})^2}{d_i^2} \quad (\text{A.11})$$

With  $W_{ij}$  as the sum of weights of the  $i$ th bin of  $j$ th histogram and  $s^2(W_{ij})$  as total sum of squares of the weights in the  $i$ th bin of the  $j$ th histogram.

$$d_i = \begin{cases} W_{2i}[s^2(W_{1i})/W_{1i} + s^2(W_{2i})/W_{2i}] & n_1 \leq n_2 \\ W_{1i}[s^2(W_{1i})/W_{1i} + s^2(W_{2i})/W_{2i}] & n_2 < n_1 \end{cases} \quad (\text{A.12})$$

According to [Gagunashvili, 2010, p.5]  $X_h^2$  has a chi-square distribution.

### A.1.3 Histograms with normalized weights

For two histograms with normalized weights the total sum of weights of events  $W_{ij}$  in the  $i$ th bin of the  $j$ th histogram is given by

$$W_{ij} = \sum_{k=1}^{n_{ij}} w_{ij}(k) \quad (\text{A.13})$$

and  $n_{ij}$ ,  $w_{ij}$  are independent random variables. We introduce a variable

$$r_{ji} = Ew_{ij} / Ew_{ij}^2 \quad (\text{A.14})$$

as the ratio of first to second moment of the distribution of weights in bin  $i$ . The calculation of the test statistic yields [see p. 7 Gagunashvili, 2010]:

$$\hat{X}_k^2 = \sum_{j=1}^2 \frac{1}{n_j} \sum_{i \neq k} \frac{\hat{r}_{ji} W_{ji}^2}{\hat{p}_i} + \sum_{j=1}^2 \frac{1}{n_j} \frac{(n_j - \sum_{i \neq k} \hat{r}_{ji} W_{ji})^2}{1 - \sum_{i \neq k} \hat{r}_{ji} \hat{p}_i} - \sum_{j=1}^2 n_j \quad (\text{A.15})$$

where

$$\hat{r}_{ji} = \sum_{k=1}^{n_{ij}} w_{ij}(k) / \sum_{k=1}^{n_{ij}} w_{ij}^2(k) \quad (\text{A.16})$$

and with

$$\hat{p}_i = \frac{\hat{r}_{1i} W_{1i} + \hat{r}_{2i} W_{2i}}{\hat{r}_{1i} n_1 + \hat{r}_{2i} n_2} \quad (\text{A.17})$$

as initial approximation for  $\hat{p}_i$ . Numerically one minimizes (A.15) and in this way we obtain the estimators for the probabilities  $\hat{p}_i$ .

## A.2 The constant fraction triggering technique

Time measurements of electrical signals at high precision are challenging and it is important to find trigger criteria independent of the pulseheight. For this reason the Constant Fraction Triggering was introduced and up to now this method of triggering is one of the most important and versatile method to measure time.

This method avoids timewalk due to a variance in signalheight, but requires constant rise time for the signal [Leo, 1994, see pp. 327]. A signal is split into two. One part is delayed, whereas the other part is attenuated by a factor  $k$  and inverted.

Now the sum of this signals has a zero-crossing point at a constant fraction  $k$  of the original signal, which can be used for a trigger logic signal.

If the delay time is so short and the undelayed signal does not reach its peak, then only the first component of the signal is taken into account for the calculation of the zero crossing point, the technique is called amplitude and risetime compensation triggering, which is suited for SiPM signal and cancels the effects of afterpulses. Additionally a deadtime in the order of the signal length inhibits further triggers.

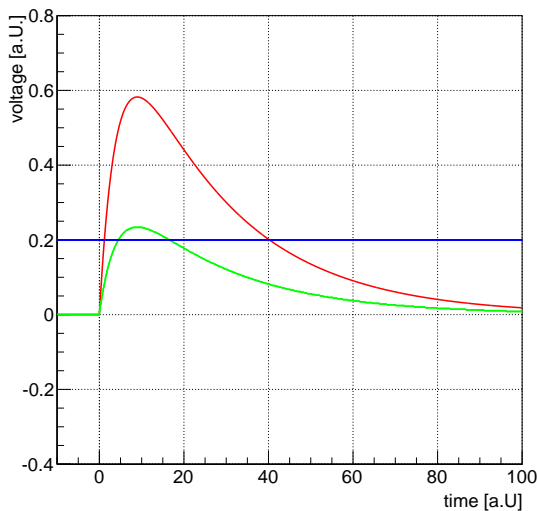


**Figure A.1:** When the signals of different amplitudes exceed a constant threshold a trigger signal is generated. Signal 1 triggers before Signal 2. This time difference is called walk

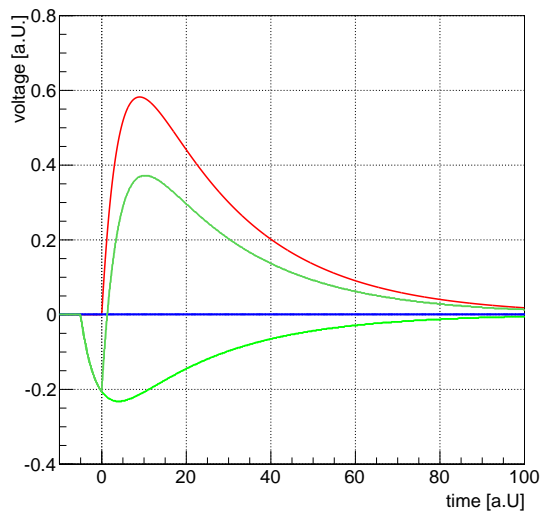


**Figure A.2:** The Constant Fraction Triggering eliminates walk, when the original Signal is delayed and a split Signal is inverted and attenuated by a factor  $k$ . The sum Signal defines the trigger at the zero crossing point.

### A.3 Uniformity of channels for the voltage divider

The calibration measurements for the voltage divider without electrical load as in figure 8.1 were done using a Keithley 6514 Electrometer, to check the uniformity of channels and to get the parameters for a more accurate adjustment of the output voltage. The obtained general values for all channels are 0.01857 V per RDAC value and 0.281 V offset. These are results of fitting a constant (see figure A.5).

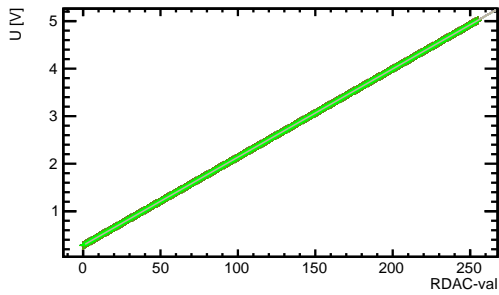


**Figure A.3:** The output voltage vs the set 8 bit RDAC-Value for 24 channels. Via straight line fit one obtains the parameters for offset and slope.

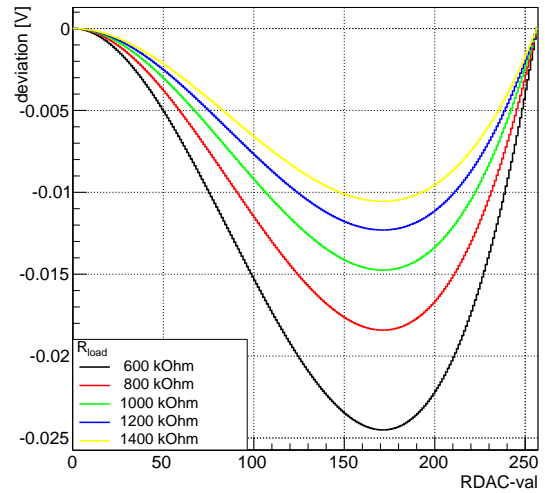


**Figure A.4:** The simulated deviation from the set voltage for the  $20\text{ k}\Omega$  digital voltage divider for  $5\text{ V}$  for different load resistances.

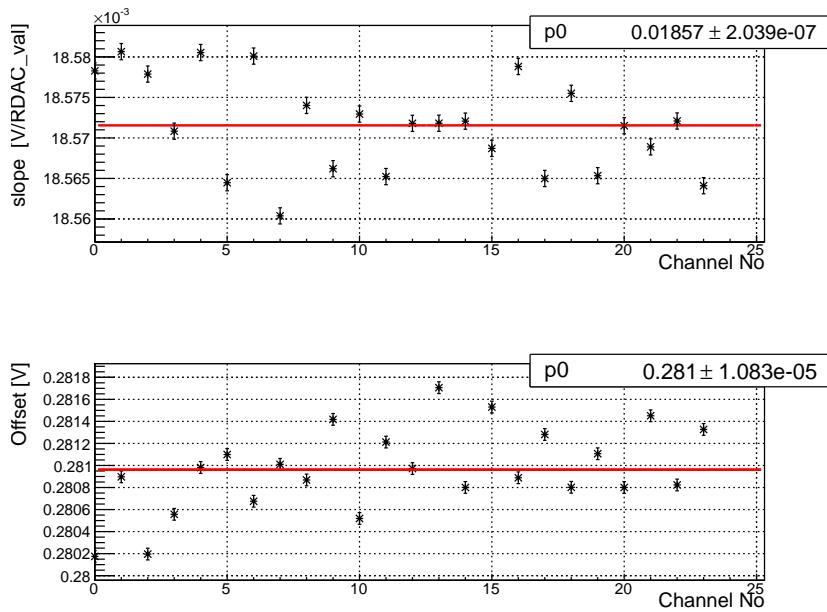


**Figure A.5:** The fit parameters from figure A.3.

SiPM No	Serial	Format	Type	Gate [ns]	$T_{meas}$ [K]	$V_{bd}$	$V_{bd}(T = 25\text{K})$	dG/dV	Error dG/dV
11	1641	1X1	100	45	20	69.28	69.58	$1.15 \times 10^6$	$1.75 \times 10^4$
11	1641	1X1	100	35	20	69.28	69.58	$9.50 \times 10^5$	$3.74 \times 10^4$
40	k000863	3X3	100	45	20	71.01	71.31	$7.56 \times 10^5$	$1.27 \times 10^4$
45	2k00856	3X3	100	45	20	70.92	71.22	$6.66 \times 10^5$	$1.71 \times 10^3$
44	2k000854	3X3	100	45	20	71.02	71.32	$8.02 \times 10^5$	$2.20 \times 10^4$
39	2k000860	3X3	100	45	20	71.08	71.38	$7.81 \times 10^5$	$2.01 \times 10^4$
6	1644	1X1	100	45	20	69.30	69.60	$1.21 \times 10^6$	$5.68 \times 10^4$
11	1641	1X1	100	45	20	69.28	69.58	$1.15 \times 10^6$	$2.24 \times 10^4$
47	1643	1X1	100	45	20	69.31	69.61	$1.21 \times 10^6$	$3.18 \times 10^4$
48	2628	1X1	100	45	20	69.25	69.55	$1.28 \times 10^6$	$3.03 \times 10^4$
49	2630	1X1	100	45	20	69.43	69.73	$1.30 \times 10^6$	$3.48 \times 10^4$
51	2626	1X1	100	45	20	69.21	69.51	$1.28 \times 10^6$	$3.56 \times 10^4$
52	2634	1X1	100	45	20	69.48	69.78	$1.27 \times 10^6$	$3.04 \times 10^4$
54	2635	1X1	100	45	20	69.46	69.76	$1.27 \times 10^6$	$5.65 \times 10^4$
50	2627	1X1	100	45	20	69.24	69.54	$1.23 \times 10^6$	$3.04 \times 10^4$
36	2j006433	3X3	50	45	25.4	72.42	72.40	$1.33 \times 10^6$	$6.44 \times 10^4$
34	2k000851	3X3	100	45	25	71.29	71.29	$8.10 \times 10^5$	$3.70 \times 10^4$
58	2j00064272	3X3	100	45	26.1	70.97	70.90	$7.87 \times 10^5$	$1.57 \times 10^3$
41	2k000859	3X3	100	45	26	71.37	71.31	$8.35 \times 10^5$	$6.04 \times 10^4$
55	2k000845	3X3	100	45	26	71.60	71.54	$7.75 \times 10^5$	$2.74 \times 10^4$
46	2k000855	3X3	100	45	25.8	71.31	71.26	$8.08 \times 10^5$	$2.73 \times 10^4$
57	2j0006432	3X3	50	45	25.8	71.10	71.05	$3.45 \times 10^5$	$9.36 \times 10^3$
53	2633	1X1	100	45	25	69.82	69.82	$1.22 \times 10^6$	$3.46 \times 10^4$
42	2k000861	3X3	100	45	26.2	71.34	71.27	$1.02 \times 10^6$	$3.75 \times 10^4$
32	2k000xxx	3X3	100	45	27.1	71.51	71.38	$1.03 \times 10^6$	$4.23 \times 10^4$
43	2k000802	3X3	100	45	26.8	71.43	71.32	$8.55 \times 10^5$	$3.96 \times 10^4$

Table A.1: The values for  $V_{bd}$  and dG/dV for the SiPMs used in the POSSUMUS prototypes.

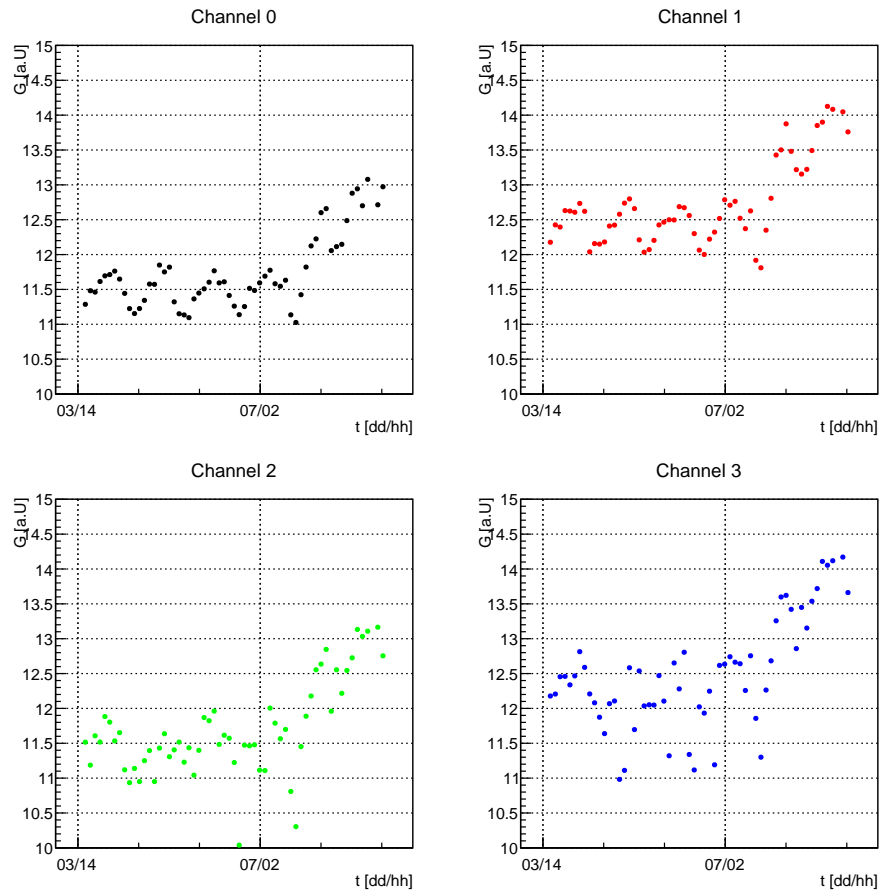


**Figure A.6:** The uncompensated gain values for 4 channels over time. A day night variation is clearly visible.

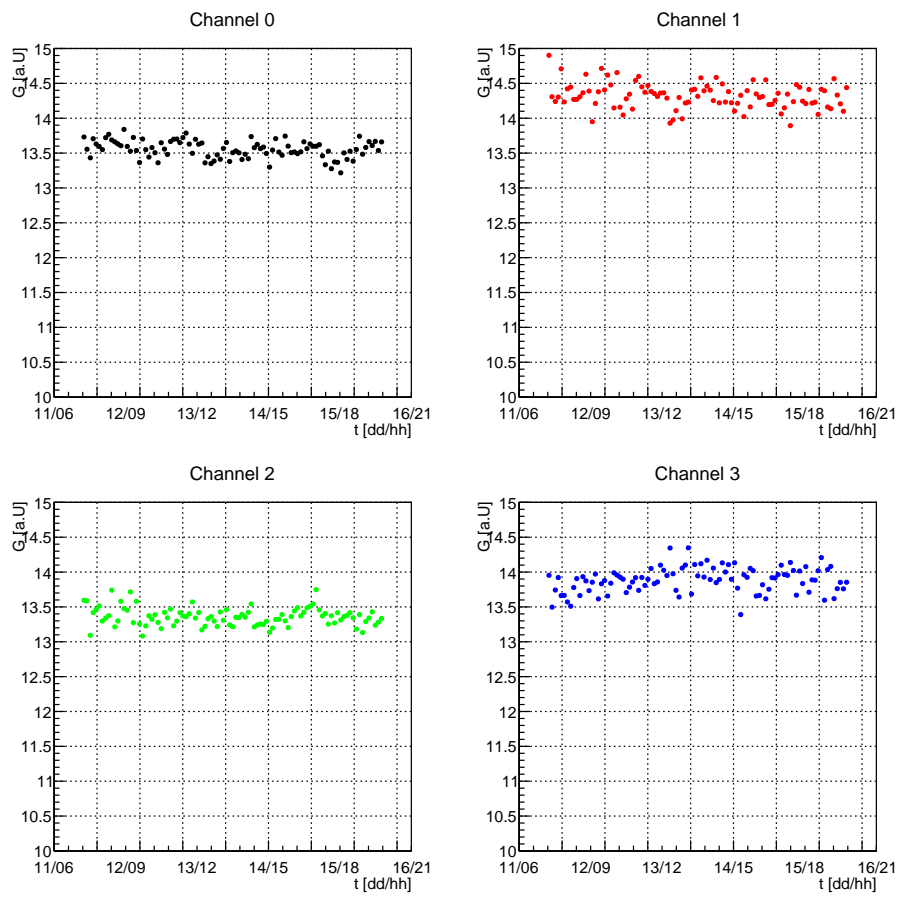
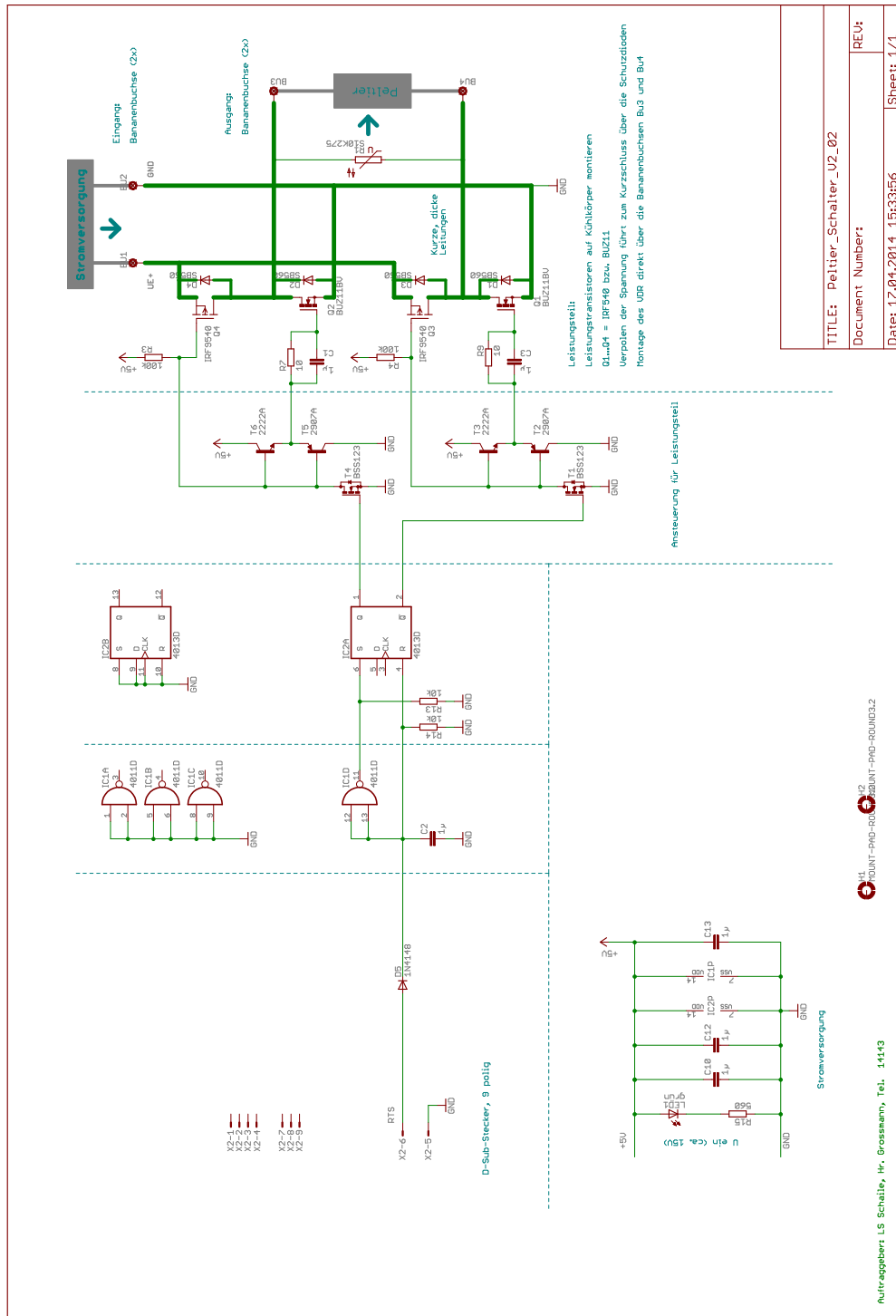


Figure A.7: The compensated gain values for 4 channels.



**Figure A.8:** The wiring diagram for the H bridge used to change the direction of the Peltier element current. The direction of the current can be set via the RTS-line of a RS232 interface.

---

## Bibliography

---

- Pietro P Altermatt, Andreas Schenk, Frank Geelhaar, and Gernot Heiser. Reassessment of the intrinsic carrier density in crystalline silicon in view of band-gap narrowing. *Journal of Applied Physics*, 93(3):1598–1604, 2003. (Cited on page 5)
- Elektronik Automatik. Datasheet EA-PSI 8160-04 t, 2014. URL <http://www.elektroautomatik.de/>. (Cited on page 57)
- O Biebel, M Binder, M Boutemour, A Brandt, J Dubbert, G Duckeck, J Elmsheuser, F Fiedler, R Hertenberger, and O Kortner. A cosmic ray measurement facility for ATLAS muon chambers. *arXiv preprint physics/0307147*, 2003. URL <http://arxiv.org/abs/physics/0307147v1>. (Cited on page 1)
- Andreas Bollu. Characterisation of silicon-photomultiplier noise and optimisation of light detection through coupling with optical fibres, April 2014. (Cited on page 48)
- P. Buzhan, B. Dolgoshein, L. Filatov, A. Ilyin, V. Kantzerov, V. Kaplin, A. Karakash, F. Kayumov, S. Klemin, E. Popova, and S. Smirnov. Silicon photomultiplier and its possible applications. *Nuclear Instruments and Methods in Physics Research Section A: Accelerators, Spectrometers, Detectors and Associated Equipment*, 504(1-3):48–52, May 2003. ISSN 01689002. doi: 10.1016/S0168-9002(03)00749-6. URL <http://linkinghub.elsevier.com/retrieve/pii/S0168900203007496>. (Cited on pages 13 and 14)
- Caen. Datasheet n455 logic, October 2004. URL <http://www.caen.it/>. (Cited on page 55)
- Caen. Datasheet v792 QDC, 2010. URL <http://www.caen.it/>. (Cited on page 35)

- Caen. Datasheet DS2477 LED driver, 2011a. URL <http://www.caen.it/>.  
(Cited on page 35)
- Caen. Datasheet n845 LTD, May 2011b. URL <http://www.caen.it/>.  
(Cited on page 55)
- Caen. Datasheet v775n TDC, December 2012. URL <http://www.caen.it/>.  
(Cited on page 55)
- David L. Chichester, Scott M. Watson, and James T. Johnson. Comparison of BCF-10, BCF-12, and BCF-20 scintillating fibers for use in a 1-dimensional linear sensor. In *Comparison of BCF-10, BCF-12, and BCF-20 scintillating fibers for use in a 1-dimensional linear sensor*, pages 365–370. IEEE, October 2012. ISBN 978-1-4673-2030-6, 978-1-4673-2028-3, 978-1-4673-2029-0. doi: 10.1109/NSSMIC.2012.6551127. URL <http://ieeexplore.ieee.org/lpdocs/epic03/wrapper.htm?arnumber=6551127>. (Cited on page 56)
- F Corsi, C Marzocca, A Perrotta, A Dragone, M Foresta, A Del Guerra, S Marcatili, G Llosa, G Collazuol, G-F Dalla Betta, and others. Electrical characterization of silicon photo-multiplier detectors for optimal front-end design. In *Nuclear Science Symposium Conference Record, 2006. IEEE*, volume 2, pages 1276–1280. IEEE, 2006.  
(Cited on page 18)
- C. R. Crowell. TEMPERATURE DEPENDENCE OF AVALANCHE MULTIPLICATION IN SEMICONDUCTORS. *Applied Physics Letters*, 9(6):242, 1966. ISSN 00036951. doi: 10.1063/1.1754731. URL <http://scitation.aip.org/content/aip/journal/apl/9/6/10.1063/1.1754731>.  
(Cited on page 40)
- Hermann Diels and Walther Kranz. *Die Fragmente der Vorsokratiker griechisch und deutsch*, volume 2. Weidmannsche Buchhandlung, Berlin-Charlottenburg, 4 edition, 1922. (Cited on page )
- N. Dinu, Z. Amara, C. Bazin, V. Chaumat, C. Cheikali, G. Guilhem, V. Puill, C. Sylvia, and J.F. Vagnucci. Electro-optical characterization of SiPM: A comparative study. *Nuclear Instruments and Methods in Physics Research Section A: Accelerators, Spectrometers, Detectors and Associated Equipment*, 610(1):423–426, October 2009.

- ISSN 01689002. doi: 10.1016/j.nima.2009.05.101. URL <http://linkinghub.elsevier.com/retrieve/pii/S0168900209011383>. (Cited on page 17)
- Nicoleta Dinu. *Instrumentation on Silicon Detectors: from properties characterization to applications*. PhD thesis, Université Paris Sud-Paris XI, 2013. URL [http://hal.in2p3.fr/docs/00/87/23/18/PDF/HDR\\_Dinu.pdf](http://hal.in2p3.fr/docs/00/87/23/18/PDF/HDR_Dinu.pdf). (Cited on pages 16, 31, 33, and 49)
- Patrick Eckert, Hans-Christian Schultz-Coulon, Wei Shen, Rainer Stamen, and Alexander Tadday. Characterisation studies of silicon photomultipliers. *Nuclear Instruments and Methods in Physics Research Section A: Accelerators, Spectrometers, Detectors and Associated Equipment*, 620(2-3):217–226, August 2010. ISSN 01689002. doi: 10.1016/j.nima.2010.03.169. URL <http://linkinghub.elsevier.com/retrieve/pii/S0168900210008156>. (Cited on page 47)
- Tim Enzweiler. *Development of a Multipurpose Light Source for SiPM Characterization*. PhD thesis, RWTH Aachen, Aachen, November 2013. (Cited on page 49)
- Paolo Finocchiaro, Alfio Pappalardo, Luigi Cosentino, Massimiliano Belluso, Sergio Billotta, Giovanni Bonanno, and Salvatore Di Mauro. Features of silicon photo multipliers: Precision measurements of noise, crosstalk, afterpulsing, detection efficiency. *IEEE Transactions on Nuclear Science*, 56(3):1033–1041, June 2009. ISSN 0018-9499. doi: 10.1109/TNS.2009.2014308. URL <http://ieeexplore.ieee.org/lpdocs/epic03/wrapper.htm?arnumber=5076065>. (Cited on pages 18 and 47)
- N.D. Gagunashvili. Chi-square tests for comparing weighted histograms. *Nuclear Instruments and Methods in Physics Research Section A: Accelerators, Spectrometers, Detectors and Associated Equipment*, 614(2):287–296, March 2010. ISSN 01689002. doi: 10.1016/j.nima.2009.12.037. URL <http://linkinghub.elsevier.com/retrieve/pii/S0168900209023547>. (Cited on pages 73, 75, and 76)
- Benjamin Glauß. *Optical Test Stand and SiPM characterisation studies*. PhD thesis, RWTH Aachen, Aachen, May 2012. (Cited on page 49)
- V. Golovin and V. Saveliev. Novel type of avalanche photodetector with geiger mode operation. *Nuclear Instruments and Methods in Physics Re-*

- search Section A: Accelerators, Spectrometers, Detectors and Associated Equipment*, 518(1-2):560–564, February 2004. ISSN 01689002. doi: 10.1016/j.nima.2003.11.085. URL <http://linkinghub.elsevier.com/retrieve/pii/S0168900203029528>. (Cited on page 13)
- Martin A. Green. Self-consistent optical parameters of intrinsic silicon at 300k including temperature coefficients. *Solar Energy Materials and Solar Cells*, 92(11):1305–1310, November 2008. ISSN 09270248. doi: 10.1016/j.solmat.2008.06.009. URL <http://linkinghub.elsevier.com/retrieve/pii/S0927024808002158>. (Cited on page 7)
- Johannes Grossmann. Charakterisierung von silizium-photomultipliern, July 2012. (Cited on page 20)
- Roland H. Haitz. Model for the electrical behavior of a microplasma. *Journal of Applied Physics*, 35(5):1370, 1964. ISSN 00218979. doi: 10.1063/1.1713636. URL <http://scitation.aip.org/content/aip/journal/jap/35/5/10.1063/1.1713636>. (Cited on page 13)
- ISEG. Datasheet ISEG SHQ 224m, February 2014. URL <http://www.iseg-hv.com>. (Cited on page 54)
- Keithley. Datasheet 2440 SourceMeter, 2002. URL <http://www.keithley.com>. (Cited on pages 30 and 37)
- Keithley. Datasheet 6514 electrometer, 2003. URL <http://www.keithley.com>. (Cited on page 31)
- Charles Kittel and Paul McEuen. *Introduction to solid state physics*, volume 8. Wiley New York, 1976. ISBN 0-471-41526-X. (Cited on pages 6, 7, and 8)
- A.L. Lacaita, F. Zappa, S. Bigliardi, and M. Manfredi. On the bremsstrahlung origin of hot-carrier-induced photons in silicon devices. *IEEE Transactions on Electron Devices*, 40(3):577–582, March 1993. ISSN 00189383. doi: 10.1109/16.199363. URL <http://ieeexplore.ieee.org/lpdocs/epic03/wrapper.htm?arnumber=199363>. (Cited on page 19)

- William R. Leo. *Techniques for nuclear and particle physics experiments: a how-to approach*. Springer, Berlin ; New York, 2nd rev. ed edition, 1994. ISBN 3540572805. (Cited on pages 10, 12, 21, 22, and 76)
- R. J. McIntyre. Theory of microplasma instability in silicon. *Journal of Applied Physics*, 32(6):983, 1961. ISSN 00218979. doi: 10.1063/1.1736199. URL <http://scitation.aip.org/content/aip/journal/jap/32/6/10.1063/1.1736199>. (Cited on page 13)
- Y. Musienko, S. Reucroft, and J. Swain. A simple model of EG&g reverse reach-through APDs. *Nuclear Instruments and Methods in Physics Research Section A: Accelerators, Spectrometers, Detectors and Associated Equipment*, 442(1-3):179–186, March 2000. ISSN 01689002. doi: 10.1016/S0168-9002(99)01218-8. URL <http://linkinghub.elsevier.com/retrieve/pii/S0168900299012188>. (Cited on page 16)
- Ralph Müller. Development of a position sensitive scintillating muon detector with silicon photo-multiplier readout, September 2013. (Cited on page 26)
- NIST. NIST PSTAR database, 2014. URL <http://physics.nist.gov/PhysRefData/Star/Text/PSTAR.html>. (Cited on page 53)
- Nepomuk Otte. *Observation of VHE gamma-Rays from the Vicinity of magnetized Neutron Stars and Development of new Photon-Detectors for Future Ground based gamma-Ray Detectors*. PhD thesis, TU München, München, August 2007. (Cited on page 49)
- Kolja Prothmann. *Comparative Measurements of Silicon Photomultipliers for the Read-out of a Highly Granular Hadronic Calorimeter*. PhD thesis, Ludwig-Maximilians Universität, München, September 2008. (Cited on pages 35, 38, and 40)
- Jozef Pulko. *A Monte-Carlo Model of a Silicon Photomultiplier*. PhD thesis, Technische Universität München, München, December 2012. URL <http://mediatum.ub.tum.de/doc/1119328/1119328.pdf>. (Cited on page 17)
- Marco Ramilli. Characterization of SiPM: temperature dependencies. In *Nuclear Science Symposium Conference Record, 2008. NSS'08. IEEE*, pages 2467–2470. IEEE, 2008. (Cited on page 47)

- Marco Ramilli, Alessia Allevi, Valery Chmill, Maria Bondani, Massimo Caccia, and Alessandra Andreoni. Photon-number statistics with silicon photomultipliers. *JOSA B*, 27(5):852–862, 2010. (Cited on pages 19 and 47)
- D Renker and E Lorenz. Advances in solid state photon detectors. *Journal of Instrumentation*, 4(04):Po4004–Po4004, April 2009. ISSN 1748-0221. doi: 10.1088/1748-0221/4/04/Po4004. URL <http://stacks.iop.org/1748-0221/4/i=04/a=Po4004?key=crossref.0b2aaff32d46c072c53ee73cbf621d59>. (Cited on pages 15, 19, and 20)
- Alexander Ruschke. *Possumus*. PhD thesis, Ludwig-Maximilians Universität, München, October 2014. (Cited on pages 1, 25, 26, 46, and 61)
- Saint-Gobain\_Crystals. Datasheet BCF-12, 2014a. (Cited on page 53)
- Saint-Gobain\_Crystals. Datasheet BCF-92,BC400, 2014b. URL [http://www.crystals.saint-gobain.com/Plastic\\_Scintillation.aspx](http://www.crystals.saint-gobain.com/Plastic_Scintillation.aspx). (Cited on page 61)
- MALVIN CARL Teich and BEA Saleh. Fundamentals of photonics. *Canada, Wiley Interscience*, page 3, 1991. (Cited on page 47)
- Voltcraft. Datasheet PSP 12010, 2008. URL [http://www.produktinfo.conrad.com/datenblaetter/500000-524999/512410-an-01-ml-PROGRAM\\_SCHALTNETZTEIL\\_PSP\\_de\\_en\\_fr\\_nl.pdf](http://www.produktinfo.conrad.com/datenblaetter/500000-524999/512410-an-01-ml-PROGRAM_SCHALTNETZTEIL_PSP_de_en_fr_nl.pdf). (Cited on page 28)
- Wacker. Datasheet wacker AK 500 000, June 2013. URL <http://www.wacker.com>. (Cited on page 57)
- T.O. White. Scintillating fibres. *Nuclear Instruments and Methods in Physics Research Section A: Accelerators, Spectrometers, Detectors and Associated Equipment*, 273(2-3):820–825, December 1988. ISSN 01689002. doi: 10.1016/0168-9002(88)90102-7. URL <http://linkinghub.elsevier.com/retrieve/pii/0168900288901027>. (Cited on pages 22 and 24)
- F. Zappa, S. Tisa, A. Tosi, and S. Cova. Principles and features of single-photon avalanche diode arrays. *Sensors and Actuators A: Physical*, 140(1):103–112, October

2007. ISSN 09244247. doi: 10.1016/j.sna.2007.06.021. URL <http://linkinghub.elsevier.com/retrieve/pii/S0924424707004967>. (Cited on page 19)



---

## Acronyms

---

$V_{over}$	overvoltage
AP	afterpulse
APD	Avalanche Photo Diode
CFD	constant fraction discriminator
CRF	Cosmic Ray Facility
CWG	Clear Wave Guide
DCR	Dark Count Rate
DS18B20	DS18B20 temperature sensor
ENF	Excess Noise Factor
GM-APD	Geiger mode APD
Ham. 1x1 025C	Hamamatsu S10362-11-025C
Ham. 1x1 050C	Hamamatsu S10362-11-050C
Ham. 1x1 100C	Hamamatsu S10362-11-100C
Ham. 3x3 025C	Hamamatsu S10362-3x3-025C
Ham. 3x3 050C	Hamamatsu S10362-3x3-050C
Ham. 3x3 100C	Hamamatsu S10362-3x3-100C
OC	Optical Crosstalk

## Acronyms

---

PDE	Photon Detection Efficiency
PDF	Probability Density Function
PE	photo electron
psp1210	PSP1210 Voltcraft programable power supply
PWM	Pulse-width modulation
QDC	charge-to-digital converter
SiPM	Silicon Photomultiplier
SNR	signal-to-noise-ratio
TDC	time-to-digital converter
WLSF	wavelength shifting fiber

---

## Symbols

---

$C_{Cell}$	The capacitance of the a SiPM microcell
$E_F$	The Fermi energy.
$G$	The amount of charge contained in an avalanche discharge of a single microcell divided by $e$
$I_{bulk}$	The current, that flows through the bulk of a p-n junction and eventually is subject to avalanche multiplication
$QE$	The quantum efficiency to create an electron-hole pair.
$R_D$	The diode equivalent resistance of a SiPM microcell
$R_{quench}$	The quenching resistance of a SiPM microcell
$U$	The net number of charge carriers generated per volume as difference between e-h pair generation and recombination rates. $U = R_{th} - G_{th}$
$V_{bd}$	the breakdown voltage of a SiPM
$V_{bias}$	the bias voltage of a SiPM
$V_{over}$	$V_{over} = V_{bias} - V_{bd}$
$V_t$	The terminal voltage of a voltage divider
$\alpha$	Charge carrier ionization probability per unit distance travelled
$dG/dV$	The temperature coefficient of the SiPM gain
$dV_{bd}/dT$	The temperature coefficient of the breakdown voltage.

$\varepsilon_{geom}$	The fill factor of a SiPM as ratio of optical active surface to total detector area.
$\varepsilon_i$	Ionization energy
$\varepsilon_r$	Raman optical phonon energy
$\varepsilon_{trigger}$	The avalanche trigger probability for a single e-h pair.
$\lambda_{Poisson}$	The mean value of a Poisson distribution.
$\lambda$	Carrier mean free path for optical phonon generation
$n_c$	the number of microcell APDs on the SiPM
$n_{trigger}$	the number of triggered microcells during a short light pulse SiPM
$n_i$	The intrinsic density of charge carriers in thermal equilibrium.
$p_{cross}$	The crosstalk probability for one microcell to trigger another microcell
$PDE$	The photon detection efficiency.
$\tau_e$	The lifetime of an e-h-pair.

---

## Glossary

---

### *amplitude and risetime compensation triggering*

The difference to Constant Fraction Triggering triggering is the delay between the inverted and attenuated signal. This technique has delays so short, that it does not allow the undelayed signal to reach its peak and so only the early portion of signal is taken into account for a trigger decision, which is especially suited for a SiPM with afterpulses during microcell recovery.

### *BC-400*

A fast plastic scintillator by St. Gobain.

### *BCF-12*

A scintillating fibre with 3.2 ns decay time.

### *BCF-92*

A 1.0 mm wave length shifting fiber with 2.7 ns decay time and peak emission at 492  $\mu\text{m}$ .

### *Chisquare Distribution*

A special case of a PDF:

$$f(x;k) = \begin{cases} \frac{x^{(k/2-1)}e^{-x/2}}{2^{k/2}\Gamma(\frac{k}{2})}, & \forall x \geq 0 \\ 0, & \textit{otherwise} \end{cases} \quad (\text{A.18})$$

### *Constant Fraction Triggering*

A modern high precision method for triggering minimizing time walk effects.

*contact potential*

In thermodynamic equilibrium the contact potential is the electrostatic potential difference between two metals or semiconductors in contact close to the surface of the boundary region.

*depletion zone*

The depletion zone is the boundary region between the n-type and p-type semiconductor and is essentially free of mobile charge carriers.

*Excess Noise Factor*

The variation in charge given a constant signal for an APD in proportional mode arises due to randomness in photon arrivals and randomness in carrier multiplication process. For a SiPM the ENF is given by the 1-photon signal

$$ENF = 1 + \sigma_1^2 / S_1^2, \quad (\text{A.19})$$

where  $\sigma_1$  is the variance of the peak and  $S_1$  is the mean value of the peak. This indicates the pixel-to-pixel gain variation.

*I<sup>2</sup>C Bus*

A digital 2-wire Bus system for setting the RDAC values.

*Monte Carlo Simulation*

The Monte Carlo method is a way of obtaining the distribution of an unknown PDF relying on repeated random sampling.

*p-n junction*

The boundary region between p- and n-type semiconductors.

*PID controller*

The PID controller is a simple controlling algorithm, which uses a feedback signal. The PID controller is considered to be the best controller, if no

information about the underlying process is given. The error  $e$  between the process variable and the set point  $e = SP - PV$  defines the controller output.

$$u(t) = K_P(e(t) + \frac{1}{T_i} \int_0^t e(\tau) d\tau + T_d \frac{d}{dt} e(t)) \quad (\text{A.20})$$

### *Poisson distribution*

The Poisson distribution defined as:

$$f(k, \lambda) = \frac{\lambda^k e^{-\lambda}}{k!} \quad (\text{A.21})$$

### *POSSUMUS*

A Position Sensitive Scintillating Muon Detector with SiPM readout.

### *RDAC*

A digitally controlled potentiometer.

### *walk*

When coincident signals of different amplitudes cross a discriminator threshold at different times, the time difference is called time walk.



---

## List of Figures

---

1.1	The CRF in Garching . . . . .	2
3.1	Band structures . . . . .	6
3.2	Absorption coefficient of silicon . . . . .	7
3.3	Doping for p-type and n-type silicon . . . . .	10
3.4	p-n junction . . . . .	11
3.5	Hamamatsu S10362-33-100C . . . . .	14
3.6	Equivalent circuit diagram of a SiPM . . . . .	14
3.7	SiPM doping concentrations and configuration of electric field . . . . .	15
3.8	Avalanche multiplication in Geiger mode . . . . .	15
3.9	Operating mode for a GM-APD . . . . .	16
3.10	Ionization coefficients for electrons and holes . . . . .	16
3.11	The equivalent circuit for a SiPM at low photon flux . . . . .	18
3.12	Dark count rate versus voltage . . . . .	20
4.1	Scintillation principle . . . . .	22
5.1	Wavelength shifter principle . . . . .	24
6.1	Sketch possumus . . . . .	25
6.2	Basic principle of position sensitivity along y-axis . . . . .	26
7.1	Current voltage characteristic for 50 mm × 50 mm Peltier element . . . . .	29
7.2	T vs time at controller setpoints . . . . .	29
7.3	Setup for the measurement of U-I characteristic . . . . .	31
7.4	Current voltage forward characteristic for different SiPM types . . . . .	31
7.5	Current voltage reverse characteristic for a Ham. 3x3 050C . . . . .	33

7.6	The U-I characteristic for the tested SiPM types . . . . .	33
7.7	Current voltage reverse characteristic for a Ham. 3x3 100C SiPM at different temperatures . . . . .	34
7.8	The temperature coefficient of a Ham. 3x3 100C via U-I characteristic	35
7.9	Setup for SiPM characterization at low photon flux. . . . .	37
7.10	QDC-readout scheme . . . . .	37
7.11	QDC spectrum of a Ham. 1x1 100C . . . . .	38
7.12	Peak positions for determination of $V_{bd}$ . . . . .	39
7.13	Temperature coefficient $dV_{bd}/dT$ via charge spectra . . . . .	40
8.1	The multichannel gain stabilization system . . . . .	44
8.2	The peaks of the charge distribution spectra at different temperatures at constant bias . . . . .	45
8.3	The peaks of the charge distribution spectrae with temperature compensation . . . . .	45
8.4	Gain monitoring without $V_{bias}$ correction . . . . .	46
8.5	The peaks of the charge distribution spectra with temperature compensation . . . . .	46
9.1	Model for the detector response . . . . .	48
9.2	Data vs MC-simulation detector response . . . . .	50
9.3	Normalized residuals . . . . .	50
9.4	Chisquare distribution for $p_{cross}$ vs $\lambda_{Poisson}$ . . . . .	50
9.6	Chisquare distribution for $PDE$ vs $p_{cross}$ . . . . .	51
10.1	Beamspot diameter . . . . .	54
10.2	Setup TDC readout test . . . . .	54
10.3	Scintillating fiber mounted to stepper motor . . . . .	54
10.4	Setup TDC readout scheme . . . . .	55
10.5	Time distribution . . . . .	56
10.7	SiPM-Fiber prototype . . . . .	58
10.8	Time distribution of the SiPM signals . . . . .	59
10.11	POSSUMUS prototype . . . . .	62
10.12	POSSUMUS prototype . . . . .	63
10.13	Sketch point source with fiber . . . . .	64

10.16	Time distribution for the direct coupling of SiPMs to the scintillator rod	67
10.17	Positions versus mean of the time spectra . . . . .	67
A.1	Conventional Triggering . . . . .	77
A.2	Constant Fraction Triggering . . . . .	77
A.3	Conventional Triggering . . . . .	78
A.4	Voltage divider . . . . .	78
A.7	The compensated gain values for 4 channels. . . . .	81
A.8	Wiring diagram H bridge . . . . .	82



---

## List of Tables

---

2.1	Bethe Bloch formula symbols . . . . .	4
3.1	Properties of silicon at 300 K . . . . .	5
7.1	Properties of different tested 1 mm × 1 mm SiPM types . . . . .	27
7.2	Properties of different tested 3 mm × 3 mm SiPM types . . . . .	28
7.3	Quenching resistance and sum resistance . . . . .	30
8.1	The goodness of $G$ controlling algorithm. The values calculated with the measurement from figures A.6, A.7 . . . . .	45
10.1	Mean standard deviation of the Gaussian fits . . . . .	61
10.2	Mean standard deviation of the Gaussian fits . . . . .	63
A.1	The values for $V_{bd}$ and $dG/dV$ for the SiPMs used in the POSSUMUS prototypes. . . . .	79



---

## Acknowledgements

---

I want to give thanks to all, who supported me during my work on this thesis - especially to Prof. Dr. Otmar Biebel, Dr. Ralf Hertenberger, Alexander Ruschke, Dr. Jona Bortfeld, Ralph Müller, Philipp Lösel, Bernhard Flierl, Elias Pree. Thanks for one exceptional year.



---

## Selbstständigkeitserklärung

---

Erklärung:

Hiermit erkläre ich, die vorliegende Arbeit selbständig verfasst zu haben und keine anderen als die in der Arbeit angegebenen Quellen und Hilfsmittel benutzt zu haben.

München, den 30.10.2014 \_\_\_\_\_

Johannes Großmann